ISSI Scientific Report 12

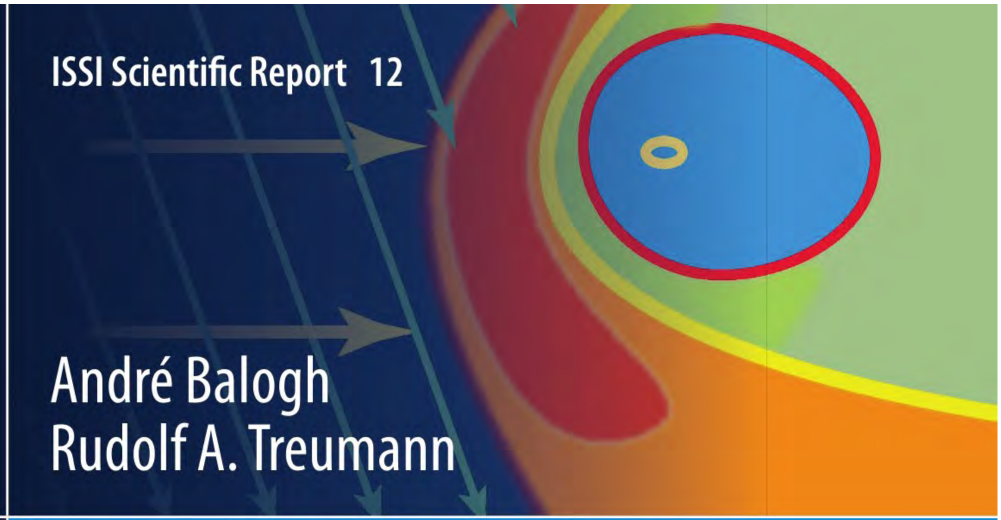

André Balogh
Rudolf A. Treumann

Physics of Collisionless Shocks

Space Plasma Shock Waves

International Space Science Institute

Springer

— 5 —

Quasi-perpendicular Supercritical Shocks

Abstract. Quasi-perpendicular shocks are the first and important family of collisionless magnetised shocks which reflect particles back upstream in order to satisfy the shock conditions. Discussion of the particle dynamics gives clear definition for distinguishing them from quasi-parallel shocks by defining a shock normal angle with respect to the upstream magnetic field. They exist for shock normal angles $<45°$. Reflected particles at quasi-perpendicular shocks cannot escape far upstream along the magnetic field. They form a foot in front of the shock ramp. We discuss the reflecting shock potential and the explicit shock structure. Most theoretical insight is provided by numerical simulations which confirm reflection, foot formation and reformation of the shock. The latter being caused by steeping of the foot disturbance until the foot itself becomes the shock transition, reflecting particles upstream. Reformation modulates the shock temporarily but on the long terms guarantees its stationarity. Ion and electron dynamics are explicitly discussed in view of the various instabilities involved as well as particle acceleration and shock heating. Finally, a sketchy model of a typical quasi-perpendicular shock transition is provided.

5.1 Setting the Frame

As long as the shocks are subcritical with Mach numbers $\mathscr{M} < \mathscr{M}_c$ the distinction between quasi-perpendicular and quasi-parallel shocks is not overwhelmingly important, at least as long as the shock normal angle is far from zero. The mechanisms of dissipation in such sub-critical (or laminar) shocks have been discussed in the previous chapter. However, when the Mach number increases and finally exceeds the critical Mach number, $\mathscr{M} > \mathscr{M}_c$, the distinction becomes very important.

We speak of quasi-perpendicular super-critical shocks when the shock-normal angles $\Theta_{Bn} < 45°$, and this because of good reasons. First, super-critical shocks cannot be maintained by dissipation alone. This has been clarified in Chapters 2 and 3. The inflow of matter into a supercritical shock is so fast that the time scales on which dissipation would take place are too long for dissipating the excess energy and lowering the inflow velocity below the downstream magnetosonic velocity. Hence, the condition for criticality, as we have shown in Chapter 2, is that the downstream flow velocity becomes equal to the downstream magnetosonic speed, which yielded the critical Mach number, $\mathscr{M}_c \lesssim 2.76$. We have also shown that $\mathscr{M}_c(\Theta_{Bn})$ is a function of the shock normal angle and can become quite small, even though $\mathscr{M}_c(\Theta_{Bn}) \gtrsim 1$ for existence of a shock, of course.

In order to help maintain a shock in the supercritical case the shock must forbid an increasing number of ions to pass across its ramp, which is done by reflecting some particles back upstream. This is not a direct dissipation process, rather it is an emergency act of the shock. It throws a fraction of the incoming ions back upstream and by this reduces

A. Balogh, R.A. Treumann, *Physics of Collisionless Shocks*, ISSI Scientific Report Series 12, DOI 10.1007/978-1-4614-6099-2_5,

both the inflow momentum and energy densities. Clearly, this reflection process slows the shock down by attributing a negative momentum to the shock itself. The shock slips back and thus in the shock frame also reduces the difference velocity to the inflow, i.e. it reduces the Mach number. In addition, however, the reflected ions form an unexpected obstacle for the inflow and in this way reduce the Mach number a second time.

These processes are very difficult to understand, and we will go into more detail of them in this chapter. However, we must ask first, what the reason is for this rigid limit in Θ_{Bn} for calling a shock a quasi-perpendicular supercritical shock. The answer is that a shock as long belongs to the class of quasi-perpendicular shocks as reflected particles cannot escape from it upstream along the upstream magnetic field. After having performed half a gyro-circle back upstream they return to the shock ramp and ultimately traverse it to become members of the downstream plasma population.

5.1.1 Particle Dynamics

To see this we must return to the orbit a particle performs in interaction with a supercritical shock when it becomes reflected from the shock. In the simplest possible model one assumes the shock to be a plane surface, and the reflection being specular turning the component v_n of the instantaneous particle velocity $\mathbf{v}$ normal to the shock by 180°, i.e. simply inflecting it. In a very simplified version we have already considered this problem in Chapter 3. Here we follow the explicit calculation for these idealised conditions as given by *Schwartz et al* [1983] who treated this problem in the most general way. One should, however, keep in mind that the assumption of ideal specular reflection is the extreme limit of what happens in reality. In fact, reflection must by no means be specular because of many reasons. One of the reasons is that the shock ramp is not a rigid wall; the particles penetrate into it at least over a distance of a fraction of their gyroradius. In addition, they interact with waves and even excite waves during this interaction and during their approach of the shock. Altogether, it must be stressed again that the very mechanisms by which they become reflected are poorly known, indeed. Specular reflection is no more than a convenient assumption. Nevertheless, observations suggest that assuming specular reflection seems to be quite a useful approximation to reality as long as nothing more precise is known about the inelastic reflection processes.

Figure 5.1 shows the coordinate frame used at the planar (stationary) shock, with shock normal $\mathbf{n}$, magnetic $\hat{b}$ and velocity $\hat{v}$ unit vectors, respectively. Shown are the angles Θ_{Bn}, θ_{Vn}, θ_{BV}. The velocity vector $\mathbf{V}_{\rm HT}$ is the de Hoffmann-Teller velocity which lies in the shock plane and is defined in such a way that in the coordinate system moving along the shock plane with velocity $\mathbf{V}_{\rm HT}$ the plasma flow is along the magnetic field. $\mathbf{V}-\mathbf{V}_{\rm HT} = -v_\| \hat{b}$. Because of the latter reason it is convenient to consider the motion of particles in the de Hoffmann-Teller frame. The guiding centres of the particles in this frame move all along the magnetic field. Hence, using $\mathbf{V} = -V\hat{v}$, $\mathbf{n}\cdot\hat{v} = \cos\theta_{Vn}$, $\mathbf{n}\cdot(\hat{b},\hat{x},\hat{y}) = (\cos\Theta_{Bn}, \sin\Theta_{Bn}, 0)$,

$$v_\| = V\frac{\cos\theta_{Vn}}{\cos\Theta_{Bn}}, \quad \mathbf{V}_{\rm HT} = V\left(-\hat{v} + \frac{\cos\theta_{Vn}}{\cos\Theta_{Bn}}\hat{b}\right) \equiv \frac{\mathbf{n}\times\mathbf{V}\times\mathbf{B}}{\mathbf{n}\cdot\mathbf{B}}, \quad V_{{\rm HT},n} \equiv 0 \qquad (5.1)$$

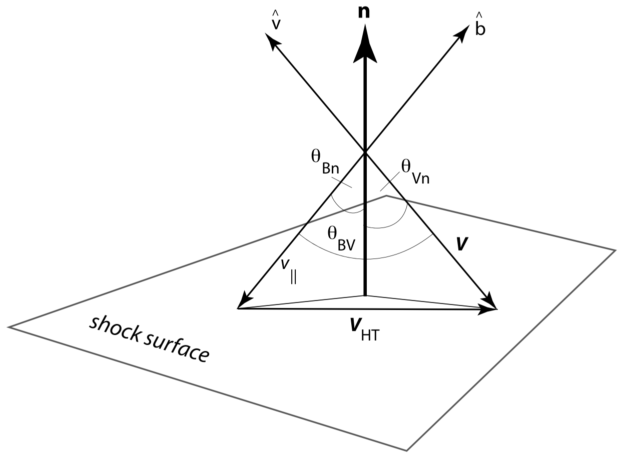

Figure 5.1: The shock coordinate system showing the shock normal **n**, velocity and magnetic field directions $\hat{v}$, $\hat{b}$, the three angles Θ_{Bn}, θ_{Vn}, θ_{BV} between $\hat{b}$ and **n**, velocity **V** and **n**, and velocity **V** and $\hat{b}$, respectively. The velocity $\mathbf{V}_{\rm HT}$ in the shock plane is the de Hoffmann-Teller velocity [after *Schwartz et al*, 1983, courtesy American Geophysical Union].

The de Hoffmann-Teller velocity is the same to both sides of the shock ramp, because of the continuity of normal component B_n and tangential electric field $\mathbf{E}_t$. Thus, in the de Hoffmann-Teller frame there is no induction electric field $\mathbf{E} = -\mathbf{n}\times\mathbf{V}\times\mathbf{B}$. The remaining problem is two-dimensional (because trivially **n**, $\hat{b}$ and $-v_\|\hat{b}$ are coplanar, which is nothing else but the coplanarity theorem holding under these undisturbed idealised conditions).

In the de Hoffmann-Teller (primed) frame the particle velocity is described by the motion along the magnetic field $\hat{b}$ plus the gyromotion of the particle in the plane perpendicular to $\hat{b}$:

$$\mathbf{v}'(t) = v'_\|\hat{b} + v_\perp\left[\hat{x}\cos\left(\omega_{ci}t+\phi_0\right) \mp \hat{y}\sin\left(\omega_{ci}t+\phi_0\right)\right] \tag{5.2}$$

The unit vectors $\hat{x}$, $\hat{y}$ are along the orthogonal coordinates in the gyration plane of the ion, the phase ϕ_0 accounts for the initial gyro-phase of the ion, and $\pm$ accounts for the direction of the upstream magnetic field being parallel $(+)$ or antiparallel to $\hat{b}$.

In specular reflection (from a stationary shock) the upstream velocity component along **n** is reversed, and hence (for cold ions) the velocity becomes

$$\mathbf{v}' = -v_\|\hat{b} + 2v_\|\cos\Theta_{Bn}\hat{n}$$

which (with $\phi_0 = 0$) yields for the components of the velocity

$$\frac{v'_\|}{V} = \frac{\cos\theta_{Vn}}{\cos\Theta_{Bn}}\left(2\cos^2\Theta_{Bn} - 1\right), \qquad \frac{v_\perp}{V} = 2\sin\Theta_{Bn}\cos\theta_{Vn} \tag{5.3}$$

These expressions can be transformed back into the observer's frame by using $\mathbf{V}_{\rm HT}$. It is, however, of greater interest to see under which conditions a reflected particle turns around in its upstream motion towards the shock. This happens when the upstream component of the velocity $v_x = 0$ of the reflected ion vanishes. For this we need to integrate Eq. (5.2) which for $\phi_0 = 0$ yields

$$\mathbf{x}'(t) = v'_{\|} t\, \hat{b} + \frac{v_\perp}{\omega_{ci}} \left\{ \hat{x} \sin \omega_{ci} t \pm \hat{y} (\cos \omega_{ci} t - 1) \right\} \tag{5.4}$$

Scalar multiplication with $\mathbf{n}$ yields the ion displacement normal to the shock in upstream direction. The resulting expression

$$\mathbf{x}'_n\left(t^*\right) = v'_{\|} t^* \cos \Theta_{Bn} + \frac{v_\perp}{\omega_{ci}} \sin \Theta_{Bn} \sin \omega_{ci} t^* = 0 \tag{5.5}$$

vanishes at time t^* when the ion re-encounters the shock with normal velocity $v_n(t^*) = v'_{\|} \cos \Theta_{Bn} + v_\perp \sin \Theta_{Bn} \cos \omega_{ci} t^*$. The maximum displacement away from the shock in normal direction is obtained when setting this velocity to zero, obtaining for the time t_m at maximum displacement (again including the initial phase here)

$$\omega_{ci} t_m + \phi_0 = \cos^{-1} \left(\frac{1 - 2\cos^2 \Theta_{Bn}}{2 \sin^2 \Theta_{Bn}} \right) \tag{5.6}$$

This expression must be inserted in $\mathbf{x}_n$ yielding for the distance a reflected ion with gyroradius $r_{ci} = V/\omega_{ci}$ can achieve in upstream direction

$$\Delta x_n = r_{ci} \cos \theta_{Vn} \left\{ (\omega_{ci} t_m + \phi_0) \left(2\cos^2 \Theta_{Bn} - 1 \right) + 2 \sin^2 \Theta_{Bn} \sin(\omega_{ci} t_m + \phi_0) \right\} \tag{5.7}$$

For a perpendicular shock $\Theta_{Bn} = 90^\circ$ and $\phi_0 = 0$ this distance is $\Delta x_n \simeq 0.7 r_{ci} \cos \theta_{Vn}$, less than an ion gyro radius. The distance depends on the shock normal angle, decreasing for non-planar shocks. Note that the argument of $\cos^{-1}$ in Eq. (5.6) changes sign for $\Theta_{Bn} \leq 45^\circ$. Equation (5.5) has solutions for positive upstream turning distances only for shock normal angles $\Theta_{Bn} > 45^\circ$, for an initial particle phase $\phi_0 = 0$. (A finite initial phase $\phi_0 \neq 0$ may, however, modify this conclusion shifting the boundary between quasi-parallel and quasi-perpendicular shock to angles larger or smaller than 45°, depending on the sign of the initial phase.) Reflected ions can return to the shock in one gyration time only when the magnetic field makes an angle with the shock normal that is larger than this value. For less inclined shock normal angles the reflected ions escape along the magnetic field upstream of the shock and do not return within one gyration. This sharp distinction between shock normal angles $\Theta_{Bn} < 45^\circ$ and $\Theta_{Bn} > 45^\circ$ thus provides the natural (kinematic specular) discrimination between quasi-perpendicular and quasi-parallel (planar) shocks we were looking for.

The theory of shock particle reflection holds, in this form, only for cold ions, which implies complete neglect of any velocity dispersion and proper gyration of the ions. The ions are considered of just moving all with one and the same oblique flow velocity $\mathbf{V}$. In a warm plasma each particle has a different speed, and it is only the group of zero velocity ions which are described by the above theory. Fortunately, these are the particles which experience the reflecting shock potential strongest and are most vulnerable to specular reflection. When temperature effects will be included, the theory is more involved in a number of ways. Firstly, the de-Hoffmann-Teller velocity must be redefined to include the microscopic particle motion. Secondly, the assumption of ideal specular reflection becomes questionable, as the particles themselves become involved into the generation of the shock potential. This problem is still open to investigation. Observations in space suggest that, for high flow velocities and supercritical Mach numbers, the simple kinematic reflection is a sufficiently well justified mechanism, however.

We may, formally, extend the above approach for warm ions to include the proper particle motion. In order to distinguish the different velocity components in this case, we indicate the bulk flow components by a tilde, $\tilde{V}'$, and write the proper microscopic velocity $\mathbf{v}_i$. Warm particles obey a phase space velocity distribution with different velocity components parallel, $v_{\|i}$, and perpendicular, $v_{\perp i}$, to the magnetic field, as well as gyration phases $\omega_{ci}t+\phi_0$. These add to the gyro-centre velocity. (One should note that in principle for high Mach numbers $V \gg v_i$ the velocity addition theorem should be applied in its relativistic version even if the proper particle motions particles are considered non-relativistic.) In the completely non-relativistic case where the velocities simply add linearly, the specularly reflected normal component of the particle velocity after reflection becomes sufficiently complicate:

$$v_n = \left(v_{\|i}+\tilde{V}'_{\|}\right)\cos\Theta_{Bn} + \left[v_{\perp i}\cos(\omega_{ci}t+\phi_0)+\tilde{V}'_{\perp}\cos\omega_{ci}t\right]\sin\Theta_{Bn} \tag{5.8}$$

The gyration phase ϕ_0 of the particle must be retained in this case as it is different from that of the bulk flow phase. The inclusion of many gyrating particles inhibits to identify it with that flow phase. Setting this normal component of velocity after reflection to zero does not lead to a simple expression for the turning point of an upstream reflected particle orbit, and the distinction between parallel and perpendicular shocks becomes blurred as it can at most be defined only approximately and in the average over the particle distributions and phases. On defining a new phase ψ through

$$\tan\psi = \frac{v_{\perp i}\sin\phi_0}{\tilde{V}'_{\perp}+v_{\perp i}\cos\phi_0} \tag{5.9}$$

the above expression set to zero can be rewritten into the form

$$\cos(\omega_{ci}t+\psi) = -\frac{v_{\|i}+\tilde{V}'_{\|}}{\tilde{V}'_{\perp}}\frac{\cos\Theta_{Bn}}{\sin\Theta_{Bn}} \tag{5.10}$$

again with the modulus of the expression on the right-hand side required to be <1 as the new condition to discriminate between parallel and perpendicular shocks. Clearly this condition makes sense only when averaged over the thermal particle distribution and over the phases of all particles. This average should, however, be taken already in Eq. (5.8).

In order to do so, we assume a simple thermal distribution of the upstream particles with anisotropic temperature T_i. In carrying out the averaging one must observe that the phase of the reflected particles can vary only in the forward half-space interval $0 \le \phi_0 \le \pi$, while the limits on the reflected parallel and perpendicular velocities are $-\tilde{V}_{\|} \le v_{\|} \le \infty$, and $0 \le v_{\perp} \le \infty$, respectively.

Now carrying out the integration and defining the new mock phase through $\tan\psi = v_{\perp i}/\sqrt{\pi}V'_{\perp}$, we find that for a hot plasma (for generality including a temperature anisotropy $T_{i\perp}/T_{i\|}$) the condition for a turning upstream gyration orbit after specular reflection can formally be written as

$$\frac{\cos(\omega_{ci}t+\psi)}{\sqrt{\pi}} = \frac{1-2\cos^2\Theta_{Bn}}{2\sin^2\Theta_{Bn}} + \frac{v_{\|i}}{V}\frac{\cos\Theta_{Bn}}{2\sin^2\Theta_{Bn}\cos\theta_{Vn}}\frac{\exp(-\tilde{V}'^2_{\|}/v^2_{\|i})}{\sqrt{\pi}[1+\mathrm{erf}(\tilde{V}'_{\|}/v_{\|i})]} \tag{5.11}$$

which in this case replaces the earlier simple condition (5.6) of the cold plasma. This is contained here in the first term on the right to which the second term adds a rather complicated thermal correction which becomes important at large parallel temperatures only, however, as indicated by the appearance of the ratio $v_{\|i}/V$. The presence of this term modifies the angle at which the sign of the right-hand side changes and thus also modifies the angle of transition from a quasi-parallel to a quasi-perpendicular shock. This modification will, of course, be more substantial the larger the upstream parallel temperature is and will further be modified if the plasma becomes relativistic, in which case it should depend on Γ. One, on the other hand, expects that highly relativistic plasmas with $\Gamma \gg 1$ will behave about like cold plasmas and therefore yield the ordinary distinction between quasi-parallel and quasi-perpendicular shocks. However, the thermal modification, though possibly not of vital importance for this distinction, will substantially affect the distance up to that a specularly reflected particle at the quasi-perpendicular shock can penetrate the upstream flow, i.e. it affects the width of the quasi-perpendicular shock-foot, even in the case when the reflection process is genuinely specular.

5.1.2 Foot Formation and Acceleration

Shock reflected ions in a quasi-perpendicular shock cannot escape far upstream (see Figure 5.2). Their penetration into the upstream plasma is severely restricted by formula (5.7). Within this distance the ions perform a gyration orbit before returning to the shock.

Since the reflected ions are about at rest with respect to the inflowing plasma they are sensitive to the inductive convection electric field $\mathbf{E} = -\mathbf{V}_1 \times \mathbf{B}_1$ behaving very similar to pick-up ions and becoming accelerated in the direction of this field to achieve a higher energy [*Schwartz et al*, 1983]. When returning to the shock their maximum (minimum) achievable energy is

$$\mathscr{E}_{\max} = \frac{m_i}{2}\left[\left(v'_{\|}+V_{\mathrm{HT}\|}\right)^2 + (V_{\mathrm{HT}\perp} \pm v_{\perp})^2\right] \tag{5.12}$$

This energy is larger than their initial energy with that they have initially met the shock ramp and, under favourable conditions, they now might overcome the shock ramp potential and escape downstream. Otherwise, when becoming reflected again, they gain energy in a second round until having picked up sufficient energy for passing the shock ramp.

In addition to this energisation of reflected ions which in the first place have not made it across the shock, the reflected ions when gyrating and being accelerated in the convection electric field constitute a current layer just in front of the shock ramp of current density

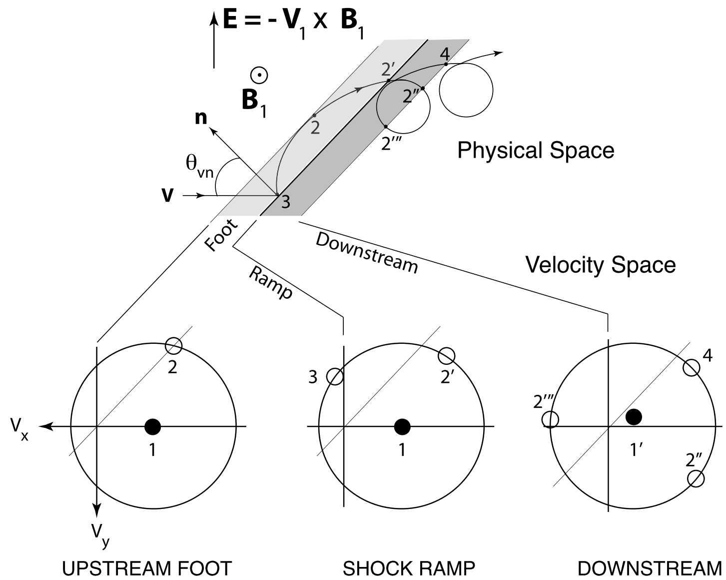

Figure 5.2: *Top*: Reflected ion orbits in the foot of a quasi-perpendicular shock in real space. The ion impacts under an instantaneous angle θ_{vn}, is reflected from the infinitely thin shock, performs a further partial gyration in the upstream field $\mathbf{B}_1$ where it is exposed to the upstream convection electric field $\mathbf{E} = -\mathbf{V}_1 \times \mathbf{B}_1$ in which it is accelerated as is seen from the non-circular section of its orbit in the shock foot. It hits the shock ramp a second time now at energy high enough to overcome the shock potential, passing the ramp and arriving in the compressed downstream magnetic field behind the shock where it performs gyrations of reduced gyro-radius. *Bottom*: The ion distribution function mapped into velocity space v_x, v_y for the indicated regions in real space, upstream in the foot, at the ramp, and downstream of the shock ramp. Upstream the distribution consists of the incoming dense plasma flow (population 1, dark circle at $v_y = 0$) and the reflected distribution 2 at large negative v_y. At the ramp in addition to the incoming flow 1 and the accelerated distribution 2' there is the newly reflected distribution 3. Behind the ramp in the downstream region the inflow is decelerated 1' and slightly deflected toward non-zero v_y, and the energised passing ions exhibit gyration motions in different instantaneous phases, two of them (2", 4) directed downstream, one of them (2"') directed upstream. [redrawn after *Sckopke et al*, 1983, courtesy American Geophysical Union].

$j_y \sim eN_{i,\mathrm{refl}} v_{y,\mathrm{refl}}$ which gives rise to a foot magnetic field of magnitude $B_{z,\mathrm{foot}} \sim \mu_0 j_y \Delta x_n$. It is clear that this foot ion current, which is essentially a drift current in which only the reflected newly energised ion component participates, constitutes a source of free energy as it violates the energetic minimum state of the inflowing plasma in its frame. Being the source of free energy it can serve as a source for excitation of waves via which it will contribute to filling the lack of dissipation. However, in a quasi-perpendicular shock there are other sources of free energy as well which are not restricted to the foot region.

Figure 5.3 shows a sketch of some of the different free-energy sources and processes across the quasi-perpendicular shock. In addition to the shock-foot current and the presence of the fast cross-magnetic field ion beam there, the shock ramp is of finite thickness. It contains a charge separation electric field E_x which in the supercritical shock is strong

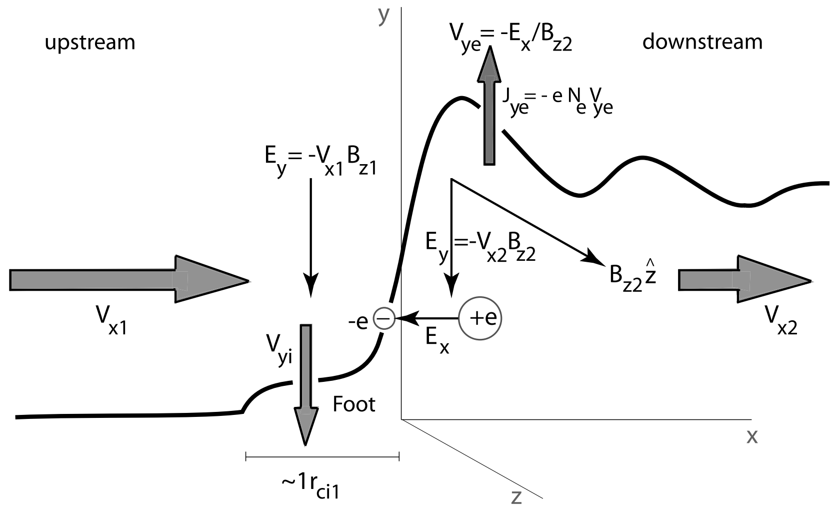

Figure 5.3: Geometry of an ideally perpendicular supercritical shock showing the field structure and sources of free energy. The shock is a compressive structure. The profile of the shock thus stands for the compressed profile of the magnetic field strength $|\mathbf{B}|$, the density N, temperature T, and pressure NT of the various components of the plasma. The inflow of velocity V_1 and outflow of velocity V_2 is in x direction, and the magnetic field is in z direction. Charge separation over an ion gyroradius r_{ci} in the shock ramp magnetic field generates a charge separation electric field E_x along the shock normal which reflects the low-energy ions back upstream. These ions see the convection electric field E_y of the inflow, which is along the shock front, and become accelerated. The magnetic field of the current carried by the accelerated back-streaming ions causes the magnetic foot in front of the shock ramp. The shock electrons are accelerated antiparallel to E_x perpendicular to the magnetic field. The shock electrons also perform an electric field drift in y-direction in the crossed E_x and compressed B_{z2} fields which leads to an electron current j_y along the shock. These different currents are sources of free energy which drives various instabilities in different regions of the perpendicular shock.

enough to reflect the lower energy ions. In addition it accelerates electrons downstream thereby deforming the electron distribution function.

The presence of this field, which has a substantial component perpendicular to the magnetic field, implies that the magnetised electrons with their gyro radii being smaller than the shock-ramp width experience an electric drift $V_{ye} = -E_x/B_{z2}$ along the shock in the ramp which can be quite substantial giving rise to an electron drift current $j_{ye} = -eN_{e,\mathrm{ramp}}V_{ye} = eN_{e,\mathrm{ramp}}E_x/B_{z2}$ in y-direction. This current has again its own contribution to the magnetic field, which at maximum is roughly given by $B_z \sim \mu_0 j_{ye}\Delta x_n$. Here we use the width of the shock ramp. The electron current region might be narrower, of the order of the electron skin depth c/ω_{pe}. However, as long as we do not know the number of magnetised electrons which are involved into this current nor the width of the electric field region (which must be less than an ion gyro-radius because of ambipolar effects) the above estimate is good enough.

The magnetic field of the electron drift current causes an overshoot in the magnetic field in the shock ramp on the downstream side and a depletion of the field on the upstream side contributing to the steepness of the ramp. When this current becomes strong it contributes to current-driven cross-field instabilities like the modified two-stream instability.

Finally, the mutual interaction of the different particle populations present in the shock at its ramp and behind provide other sources of free energy. A wealth of instabilities and waves is thus expected to be generated inside the shock. To these micro-instabilities add the longer wavelength instabilities which are caused by the plasma and field gradients in this region. These are usually believed to be less important as the crossing time of the shock is shorter than their growth time. However, some of them propagate along the shock and have therefore substantial time to grow and modify the shock profile. In the following we will turn to the discussion of numerical investigations of some of these processes reviewing their current state and provide comparison with observations.

5.1.3 Shock Potential Drop

One of the important shock parameters is the electric potential drop across the shock ramp – or if it exists also across the shock foot. This potential drop is not necessarily a constant but changes with location along the shock normal. We have already noted that it is due to the different dynamical responses of the inflowing ions and electrons over the scale of the foot and ramp regions. Its theoretical determination is difficult, however when going to the de Hoffmann-Teller frame the bulk motion of the particles is only along the magnetic field, and in the stationary electron equation of motion the $\mathbf{V}_e \times \mathbf{B}$-term drops out and, to first approximation, the cross shock potential is given by the pressure gradient (when neglecting any contributions from wave fields). The expression is then simply

$$\Delta\Phi(x) = \int_0^x \frac{1}{eN_e(n)} \left[\nabla \cdot \mathsf{P}_e(n)\right] \cdot \mathrm{d}\mathbf{n} \tag{5.13}$$

Integration is over n along the shock normal $\mathbf{n}$. For a gyrotropic electron pressure, valid for length scales longer than an electron gyroradius, $\mathsf{P}_e = P_{e\perp}\mathsf{I} + (P_{e\|} - P_{e\perp})\mathbf{BB}/BB$ one obtains [*Goodrich & Scudder*, 1984], taking into account that $\mathbf{E}\cdot\mathbf{B}$ is invariant,

$$\frac{\mathrm{d}}{\mathrm{d}n}\Phi(n) = -\frac{E_\|}{\cos\Theta_{Bn}} = \frac{1}{eN_e}\left[\frac{\mathrm{d}}{\mathrm{d}n}P_{e\|} - (P_{e\|} - P_{e\perp})\frac{\mathrm{d}}{\mathrm{d}n}(\ln B)\right] \tag{5.14}$$

which, when used in the above expression, yields

$$e\Delta\Phi(x) = \int_0^x \mathrm{d}n \left\{ \frac{\mathrm{d}T_{e\|}}{\mathrm{d}n} + T_{e\|}\frac{\mathrm{d}}{\mathrm{d}n}\ln\left[\frac{N(n)}{N_1}\frac{B_1}{B(n)}\right] + T_{e\perp}\frac{\mathrm{d}}{\mathrm{d}n}\ln\left[\frac{B(n)}{B_1}\right]\right\} \tag{5.15}$$

This expression can approximately be written in terms of the gradient in the electron magnetic moment $\mu_e = T_{e\perp}/B$ as follows:

$$e\Delta\Phi(x) \simeq \Delta(T_{e\|} + T_{e\perp}) - \int_0^x \mathrm{d}n \frac{\mathrm{d}\mu_e(n)}{\mathrm{d}n} B(n) \tag{5.16}$$

with T_e in energy units. When the electron magnetic moment is conserved, the last term disappears, yielding a simple relation for the potential drop $e\Delta\Phi(x) \simeq \Delta(T_{e\|} + T_{e\perp})$ as the sum of the changes in electron temperature. The perpendicular temperature change can be expressed as $\Delta T_{e\perp} = T_{e\perp,1}\Delta B/B_1$ which is in terms of the compression of the magnetic field. Non-adiabatic effects contribute via the dropped integral term.

The parallel change in temperature is more difficult to express. One could express it in terms of the temperature anisotropy $A_e = T_{e\|}/T_{e\perp}$ as has been done by *Kuncic et al* [2002], and then vary A_e. But this depends on the particular model. It is more important to note that this adiabatic estimate of the potential drop does not account for any dynamical process which generates waves and substructures in the shock. It thus gives only a hint on the order of magnitude of the potential drop across the foot-ramp region in quasi-perpendicular shocks.

5.2 Shock Structure

Figure 5.4 shows observations from one of the first unambiguous satellite crossings of a quasi-perpendicular supercritical (magnetosonic Mach number $\mathscr{M}_{ms} \sim 4.2$) shock in near Earth space. The crossing occurred at the Earth's bow shock, the best investigated shock in the entire cosmos! A complete discussion of its properties will be given in Chapter 10. Here it should mainly serve for visualisation of the properties of a real collisionless shock how it appears in the data. The shock crossing shown in the figure is indeed a textbook example.

5.2.1 Observational Evidence

The crossing occurred on an inbound path of the two spacecraft ISEE 1 (upper block of the figure) and ISEE 2 (lower block of the figure) from upstream to downstream in short sequence only minutes apart. In spite of some differences occurring on the short time scale the two shock crossings are about identical, identifying the main shock transition as a spatial and not as a temporal structure. Temporal variations are nevertheless visible on the scale of a fraction of a minute.

From top to bottom the figure shows the electron density (N_E), energetic ion density (N_I), proton and electron temperatures (T_P, T_E), bulk flow velocity (V_P), electron pressure (P_E), magnetic field (B), and Θ_{Bn}. The latter is close to 90° prior to shock crossing (in the average $\Theta_{Bn} \sim 85°$), and fluctuates afterwards around 90° identifying the shock as quasi-perpendicular. Accordingly, the shock develops a foot in front of the shock ramp as can be seen from the slightly enhanced magnetic field after 22:51 UT in ISEE 1 and similar in ISEE 2, and most interestingly also in the electron pressure. At the same time the bulk flow velocity starts decreasing already, as the result of interaction and retardation in the shock foot region. The foot is also visible in the electron density which increases throughout the foot region, indicating the presence of electrons which, as is suggested by the increase in pressure, must have been heated or accelerated.

The best indication of the presence of the foot is, however, the measurement of energetic ions (second panel from top). These ions are observed first some distance away from the shock but increase drastically in intensity when entering the foot. These are the shock-reflected ions which have been accelerated in the convection electric field in front of the shock ramp. Their occurrence before entrance into the foot is understood when realising that the shock is not perfectly perpendicular. Rather it is quasi-perpendicular such that part of the reflected ions having sufficiently large parallel upstream velocities can escape along the magnetic field a distance larger than the average upstream extension of the foot. For nearly perpendicular shocks, this percentage is small.

The shock ramp in Figure 5.4 is a steep wall in B and P_E, respectively. The electron temperature T_E increases only moderately across the shock while the ion temperature T_P jumps up by more than one magnitude, exceeding T_E downstream behind the shock. This behaviour is due to the accelerated returning foot-ions which pass the shock. P_E, B, and N_E exhibit overshoots behind the shock ramp proper. Farther away from the shock they merge into the highly fluctuating state of lesser density, pressure, and magnetic field that can be described as some kind of turbulence. Clearly, this region is strongly affected by the presence of the shock which forms one of its boundaries, the other boundary being the obstacle which is the main responsible for the formation of the shock.

The evidence provided by the described measurements suggests that the quasi-perpendicular shock is a quasi-stationary entity. This should, however, not been taken as apodictive. Stationarity depends on the spatial scales as well as the time scales. A shock is a very inhomogeneous subject containing all kinds of spatial scales. Being stationary on one scale does not imply that it is stationary on another scale. For a shock like the Earth's bow shock considered over times of days, weeks or years the shock is of course a stationary subject. However on shorter time scales of the order of flow transition times this may not be the case. A subcritical shock of the kind discussed in Chapter 4 may well be stationary on long and short time scales. However, for a supercritical shock the conditions for forming a stationary state are quite subtle. From a single spacecraft passage like that described above it cannot be concluded to what extent, i.e. on which time scale and on which spatial scale and under which external conditions (Mach number, angle, shock potential, plasma-$\beta, \ldots$) the observed shock can be considered to be stationary [a discussion of the various scales has been given, e.g, by *Galeev et al*, 1988]. Comparison between the two ISEE spacecraft already shows that the small-scale details as have been detected by both spacecraft are very different. This suggests that – in this case – on time scales less than a minute variations in the shock structure must be expected.

Generally spoken, one must be prepared to consider the shock locally (on the ion gyroscale) and temporarily (on the ion-cyclotron frequency scale) as a non-stationary phenomenon [this has been realised first by *Morse et al*, 1972] which depends on many competing processes and, most important though only secondarily related to non-stationarity, a shock as a whole is not in thermal equilibrium. It needs to be driven by some energy source external to the shock in order to be maintained. It will thus be very sensitive to small changes in the external parameters and will permanently try to escape the non-equilibrium state and to approach equilibrium. Since its non-equilibrium is maintained by the conditions in the flow, it is these conditions which determine the time scales over which a shock evolves, re-evolves and changes its state. In the following we will refrain from analytical theory and, forced by the complexity of the problem, mainly discuss numerical experiments on shocks. However, at a later stage we will return to the problem of non-

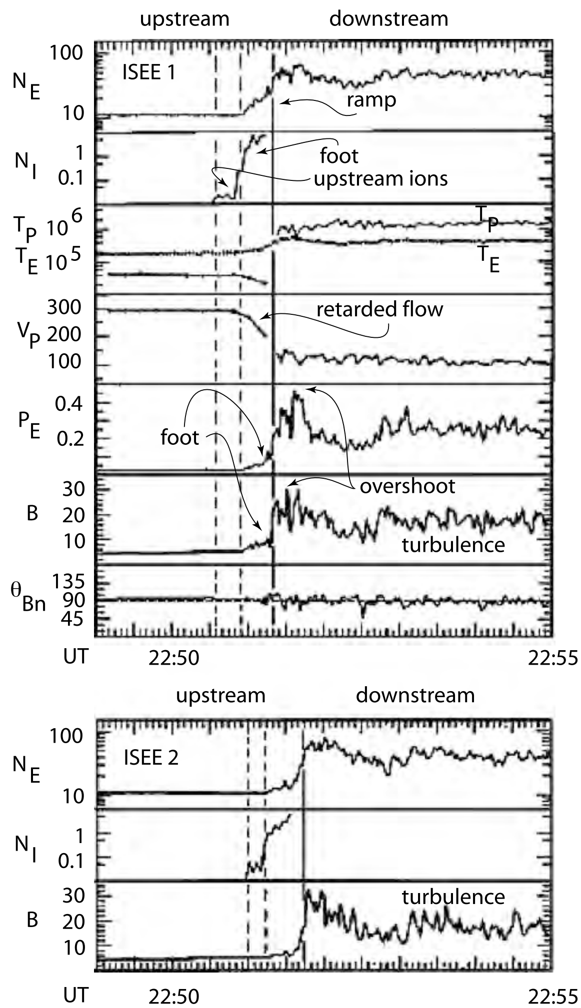

Figure 5.4: Time profiles of plasma and magnetic field parameters across a real quasi-perpendicular shock that had been crossed by the ISEE 1 and 2 spacecraft on November 7, 1977 in near-Earth space [after *Sckopke et al*, 1983, courtesy American Geophysical Union]. The shock in question is the Earth's bow shock wave which will be described in detail Chapter 10. Here the measurement serve as typical for a quasi-perpendicular shock. N_E is the electron density, N_I the reflected ion density, both in cm^{-3}, T_p, T_E are proton and electron in K. V_P is the proton (plasma) bulk velocity in km s-1, P_E electron pressure in 10^{-9} N m^{-2}, B the magnitude of the magnetic field in nT, and Θ_{Bn}. The *vertical lines* mark the first appearance of reflected ion, the outer edge of the foot in the magnetic profile, and the ramp in the field magnitude, respectively. The *abscissa* is the Universal Time UT referring to the measurements. The *upper block* are observations from ISEE 1, the *lower block* observations from ISEE 2.

stationarity again. Real supercritical shocks, whether quasi-perpendicular or quasi-parallel are in a permanently evolving state and thus are *intrinsically* nonstationary.

5.2.2 Simulation Studies of Quasi-perpendicular Shock Structure

Perpendicular or quasi-perpendicular collisionless shocks are relatively easy to treat in numerical simulations. Simulations of this kind have been mostly one-dimensional. Only more recently they have begun to become treated in two dimensions.

Already from the first one-dimensional numerical experiments on collisionless shocks [for an early review cf., e.g., *Biskamp*, 1973] if became clear that such shocks have a very particular structure. This structure, which we have describe in simplified version in Figure 5.3 and which could to some extent also be inferred from the observations of Figure 5.4, becomes ever more pronounced the more refined the resolution becomes and the better the shorter scales can be resolved.

As already mentioned, collisionless shocks are in thermodynamic non-equilibrium and therefore can only evolve if a free energy source exists and if the processes are violent enough to build up and maintain a shock. Usually in a freely evolving system the free energy causes fluctuations which serve dissipating and redistributing the free energy towards thermodynamic and thermal equilibria. (Thermal equilibria are characterised by equal temperatures among the different components, e.g. $T_e = T_i$ which is clearly not given in the vicinity of a shock as seen from Figure 5.4. Thermodynamic equilibria are characterised by Gaussian distributions for all components of the plasma. To check this requires information about the phase space distribution of particles. Shocks contain many differing particle distributions, heated, top-flat, beam distributions, long energetic tails, and truncated as well as gyrating distributions which we will encounter later. Consequently, they are far from thermodynamic equilibrium.)

For a shock to evolve the amount of free energy needed to dissipate is so large that fluctuations are unable to exercise their duty. This happens at large Mach numbers. The shock itself takes over the duty of providing dissipation. It does it in providing all kinds of scales such short that a multitude of dissipative processes can set on.

Scales

For a quasi-perpendicular shock propagating and evolving in a high-β plasma there is a hierarchy of such scales available (we recall that $\beta = 2\mu_0 nT/B^2$ refers to the thermal energy of the flow. The kinetic $\beta_{kin\perp} = 2\mu_0 N m_i V_n^2/2B^2 \equiv \mathscr{M}^2 > 1$ implies that the kinetic energy in the flow exceeds the magnetic energy. Hence the flow dominates the magnetic field, which is transported by the flow. In plasmas with $\beta_{kin\perp} = \mathscr{M}^2 < 1$ the magnetic field dominates the dynamics, and shock waves perpendicular to the magnetic field cannot evolve. Parallel shocks are basically electrostatic in the $\beta_{kin\perp} \ll 1$-case and can evolve when the flow is sufficiently fast along the field, as is observed in the auroral magnetospheres of the magnetised planets in the heliosphere. On the other hand, for large Mach numbers and $\beta \gtrsim 1$ conditions shocks do exist, as the example of the solar wind shows).

The different scales can be organised with respect to the different regions of the shock.

1. The macroscopic scale of the foot region, which determines the width of the foot, is the ion gyroradius based on the inflow velocity $r_{ci,1} = V_1/\omega_{ci,1}$. With the slight modification of replacing the upstream magnetic field with the (inhomogeneous) ramp magnetic field $B_r(x)$ this also becomes approximately the scale of the macroscopic electric potential drop in the ramp, $\Delta_{\phi,r} \sim r_{ci,r} \sim V_1/\omega_{ci,r}$.

Other scales are

2. the ion inertial length c/ω_{pi}, which is also a function of space inside the ramp because of the steep density increase $N(x)$. It determines the dispersive properties of the fast magnetosonic wave which is locally responsible for steeping and shock ramp formation;

3. the thermal ion gyroradius $r_{ci} = v_i/\omega_{ci}$. It determines the transition from unmagnetised to magnetised ions and from non-adiabatic to adiabatic heating of the ions;

4. the density gradient scale $L_P = (\nabla_x \ln P)^{-1}$. It determines the importance of drift waves along the shock which, when excited, structure the shock in the third dimension perpendicular to the shock normal and the magnetic field;

5. the electron inertial length c/ω_{pe}. It is the scale length of whistlers which are excited in front of the shock and are generally believed to play an essential role in shock dynamics;

6. the thermal electron gyroradius $r_{ce} = v_e/\omega_{ce}$. It determines whether electrons behave magnetised or non-magnetised. In the shock they are usually magnetised under all conditions of interest. However, when non-adiabatic heating becomes important for electrons it takes place on scales comparable to r_{ce};

7. the Debye length λ_D. It determines the dispersive properties of ion acoustic waves which are responsible for anomalous resistivity and for smaller scale density substructures in the shock like the phase space holes mentioned earlier which evolve on scales of several Debye lengths. It also determines the scales of the Buneman two-stream (BTS) and modified two-stream (MTS) instabilities which are the two most important instabilities in the shock foot.

The importance of some of these scales has been discussed by [*Kennel et al*, 1985] assuming that some mostly anomalous resistance has been generated in the plasma. In this case the speed of the fast magnetosonic wave, which is responsible for fast shock formation, is written as

$$c_{ms}^2 = c_{ia}^2 + \frac{V_A^2}{1+k^2R^2}, \qquad R = \begin{cases} R_\eta = (\eta/\mu_0)(k/\omega), & \eta \neq 0 \\ \lambda_e = c/\omega_{pe}, & \eta \to 0 \end{cases} \tag{5.17}$$

taking explicitly care of the dispersion of the wave which leads to wave steeping. The macroscopic scale of shock formation enters here through the definition of R which in the collisionless case becomes the electron skin depth. Starting from infinity far away from the shock one seeks for growing solutions of the linear magnetic disturbance $b_z \sim \exp \lambda x$ in the stationary point equation

$$R_e^2 b_z'' + R_\eta b_z' = D b_z, \qquad D \equiv \frac{1 - \mathscr{M}^{-2}}{1 - c_{ia}^2/V^2}$$

where the prime $' \equiv \partial/\partial x$ indicates derivation with respect to x. With $b_z \to 0$ for $x \to -\infty$ this yields for the spatial growth rate

$$\lambda_> = -\frac{R_\eta}{2\lambda_e^2} + \left[\frac{D}{\lambda_e^2} + \left(\frac{R_\eta}{2\lambda_e^2}\right)^2\right]^{\frac{1}{2}} \to \frac{D^{\frac{1}{2}}}{\lambda_e} \qquad \text{for} \qquad R_\eta \ll \lambda_e \tag{5.18}$$

which identifies the approximate shock transition scale as proportional to the electron skin depth, $\Delta \simeq c/\omega_{pe} D^{\frac{1}{2}}$, just what one intuitively would believe to happen for freely moving electrons and ions. Since the upstream sound speed $c_{ia} \ll V$ is small compared with the fast flow V, we have $D \approx 1 - \mathscr{M}^{-2}$, and the shock ramp width becomes slightly larger than the electron skin depth $\lambda_e = c/\omega_{pe}$, viz.

$$\Delta \simeq \mathscr{M}\left(\mathscr{M}^2 - 1\right)^{-\frac{1}{2}} \lambda_e \tag{5.19}$$

For large Mach numbers this width approaches λ_e. However, we have already seen that at large Mach numbers the competition between dispersion and dissipation does not hold anymore in this simple way.

With increasing wave number k the fast magnetosonic mode merges into the whistler branch with its convex dispersion curve. This implies that dispersive whistler waves will outrun the shock becoming precursors of the shock, a problem we have discussed in Chapter 3. Whistlers propagate only outside their resonance cone. The limiting angle between $\mathbf{k}$ and the magnetic field $\mathbf{B}$ for which the whistler outruns the shock is given by $\theta_{\mathrm{wh,lim}} \lesssim \cos^{-1}[\mathscr{M}_A(m_e/m_i)^{\frac{1}{2}}]$, artificially limiting the Alfvénic Mach number $\mathscr{M}_A = V/V_A < 43$.

In one-dimensional simulations with all quantities changing only along the shock normal $\mathbf{n}$ and the $\mathbf{k}$-vectors of waves along $\mathbf{n}$ as well, one choses angles between $(\mathbf{k}, \mathbf{n})$ and $\mathbf{B}$ larger than this in order to have clean effects which are not polluted by those whistlers. However, the maximum phase speed of whistlers does not exceed the Alfvén speed by much (see Figure 3.10). Hence, as long as the upstream velocity is less than this maximum whistler speed, a standing whistler precursor will be attached to the shock in front. When the upstream velocity exceeds this velocity, phase standing whistlers become impossible. This happens at the critical whistler Mach number given in Chapter 3. The shock structure becomes more complicated then by forming shock substructures [*Galeev et al*, 1988] on scales of c/ω_{ce}, and the shock might become non-stationary [*Krasnoselskikh et al*, 2002].

One-Dimensional Structure

One-dimensional observations as those presented in Figure 5.4 confirm the theoretical prediction of the gross structure of a quasi-perpendicular shock. They can, however, when taken by themselves, not resolve the spatial structure of the shock on smaller scales, nor do they allow to infer about the evolution of the shock. To achieve a clearer picture of both, the structure and the evolution, the observations must be supported by numerical simulations.

Such simulations have been performed in the past in various forms either as hybrid simulations or as full particle simulations. In hybrid simulations the electrons form a neutralising, massless background with no dynamics, i.e. the electrons react instantaneously while maintaining and merely adjusting their equilibrium Boltzmannian distribution to the locally changing conditions. Such simulations overestimate the role of the ions and neglect the dynamical contribution of the electrons. They nevertheless give a hint on the evolution and gross structure of a shock on the ion scales. Hybrid simulations have the natural advantage that they can be extended over relatively long times $\omega_{ci}t \gg 1$.

On the other hand full particle simulations are usually done for unrealistically small mass ratios $m_i/m_e \ll 1836$ much less than the real mass ratio. The electrons in these simulations are therefore heavy even under non-relativistic conditions. Their reaction is therefore unnaturally slow, the electron plasma and cyclotron frequencies are low, and the electron gyroradius, inertial length, and Debye length are unnaturally large. Under these conditions electrons readily become unmagnetised, non-adiabatic electron heating is prominent, and dispersive effects on ion-acoustic waves are overestimated.

Moreover, because of the large electron mass the electron thermal speed is reduced, and the Buneman two-stream instability sets on earlier and grows faster than under realistic conditions. This again should affect electron heating and structuring of the shock. On the other hand, the reduced electron gyroradius also reduces the shock potential, because the differences in ion and electron penetration-depths into the shock are smaller than in reality. This reduces the reflection capability of the shock, reduces the direct electric field heating of the impacting electrons, reduces the electron drift current in the shock ramp and shock transition and thus underestimates the dynamic processes in the shock, its structure, time dependence, formation and reformation and the strength of the foot effect and density of the foot population.

It is very difficult to separate all these effects, and comparison of different simulations is needed.

Low-Mass Ratio Simulations

Figure 5.5 shows an early one-dimensional low-mass-ratio perpendicular shock simulation with $m_i/m_e = 128$. Simulation times are short, not more than four ion-gyration times when energy conservation starts breaking down. Moreover, only a very small number of macro-particles (see Chapter 2) per simulation grid cell could be carried along in these simulation. Thus the noise in the simulations is large, not allowing for long simulation times, readily introducing diverging fake modes and fake dissipation/heating.

Nevertheless, the left-hand side of the figure shows the evolution of the magnetic field from the homogeneous state into a shock ramp and further the destruction and, what is known by now from much longer and better resolved simulation studies, the reformation of the shock profile. It should be noted that the shock in this case forms by reflection of the

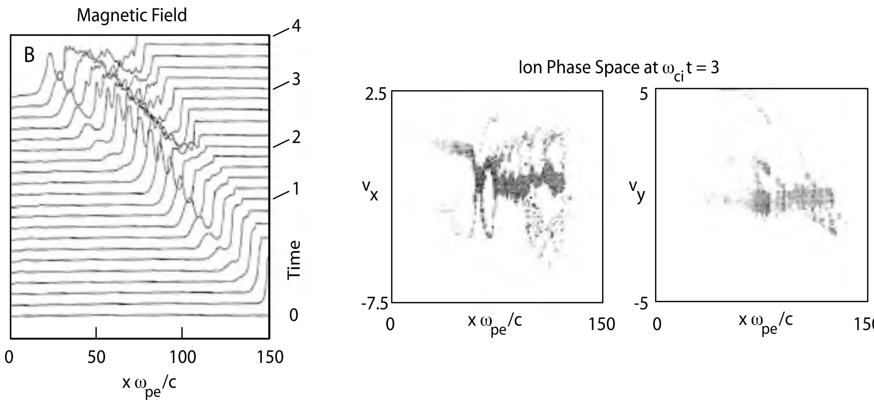

Figure 5.5: One-dimensional full particle-in-cell (PIC) simulations [after *Biskamp & Welter*, 1972] of shock formation assuming a mass ratio of $m_i/m_e = 128$. *Left*: Time-evolution of the magnetic field in stack-plot representation. Time is measured in units of ω_{ci}^{-1}, space in units of (heavy) electron inertial lengths c/ω_{pe}. The simulations are for a supercritical shock with $\mathscr{M} = 2.3$. Note the evolution of the magnetic field and the formation of a ramp, a foot and an overshoot. *Right*: Ion phase space plots (v_x, x) and (v_y, x) at time $\omega_{ci}t = 3$. Velocities are measured in units of the Alfvén velocity $V_A = B/\sqrt{\mu_0 N m_i}$.

fast initial supercritical flow with Mach number $\mathscr{M} = 2.3$ (which is above critical for the conditions of the simulation), entering the one-dimensional simulation 'box' from the left, from a 'magnetic piston' located at the right end of the box. This reflection causes a backstreaming ion-beam that interacts with the inflowing ions and drives an electromagnetic ion-ion instability which grows to large amplitude. The system is not current-free. In the interaction region of the two ion components the magnetic field forms a shock ramp. But after a short time of a fraction of an ion gyro-period a new ramp starts growing in the foot of the ramp, which itself evolves into a new ramp while the old ramp becomes eroded. This new ramp has not sufficient time to evolve to a full ramp as another new ramp starts growing in its foot. This causes the shock ramp to jump forward in space in steps from one ramp to the next, leaving behind a downstream compressed but fluctuating magnetic field region. The jump length is about the width of the foot region. It will become clear later why this is so.

Hybrid simulations [*Leroy et al*, 1981, 1982; *Leroy*, 1984] with fluid electrons and an artificially introduced anomalous resistivity show similar behaviour even though a number of differences have been found which are related to shock reformation. In particular shock reformation is slow or absent in hybrid simulations if not care is taken on the reaction of the electrons. The responsible instability in the foot region cannot evolve fast enough even though the hybrid simulation which take care of the ion dynamics also find reflection of ions and the evolution of a foot in front of the ramp. These differences must be attributed to the above mentioned lesser reliability of hybrid simulations than full particle codes.

Extended low-mass ratio full particle simulations in one space dimensions over a wide range of shock-normal angles $\Theta_{Bn} < 45°$ have been performed by *Lembège & Dawson*

[1987a, b] with the purpose to study plasma heating. These simulations used mass ratios of $m_i/m_e = 100$ and a magnetic-piston generated shock. The simulations were completely collisionless, relatively small Mach number but nevertheless supercritical when taking into account the decrease in critical Mach number with Θ_{Bn} [*Edmiston & Kennel*, 1984]. They showed the formation of a foot and overshoot, the generation of an electric charge separation field in the shock transition from the foot across the shock with a highly structured electric field which was present already in the shock foot. Moreover, indications for a periodicity of the electric field structure in the foot region were given which we now understand as standing whistler wave precursors in the shock foot for oblique shock angles and supercritical but moderate Mach numbers [*Kennel et al*, 1985; *Balikhin et al*, 1995]. In addition to the field variations these simulations already demonstrated much of the supercritical particle dynamics related to shock reflection and foot formation which we will discuss separately below.

Before discussing the ion phase space plots in Figure 5.5 on the right we are going to describe recent investigations on the effects of the mass ratio dependence of the one-dimensional full particle simulations on the shock structure. Of course, in the end only such simulations can be believed which not only take into account the full mass ratio but which are long enough for following the evolution of the shock from a small disturbance up to a stage where the shock on some time scale has approached kind of a state that in a certain sense does non further evolve. This state is either stationary or it repeats and restores itself such that it is possible to speak at all of a quasi-perpendicular supercritical shock.

The Shock Transition Scale

Determination of the shock foot scale is relatively easy both in simulations as also from observation. From observations, as already mentioned, it has been first determined by *Sckopke et al* [1983] who found that the foot scale is slightly less but close ($\sim 0.7\, r_{ci,\mathrm{refl}}$) to the reflected ion gyroradius in quasi-perpendicular shocks. The reasons for this number have been given by *Schwartz et al* [1983] and are related to the reflected ions coupling to the upstream convection electric field in which they are accelerated. This can also be checked in simulations. Of more interest is the determination of the shock transition, i.e. the width of the shock ramp which from theory is not well determined since it depends on several factors which can hardly be taken into account at once.

The width of the shock transition is particularly important in its relation to the width of the electrostatic potential drop across the shock. There are essentially three transition scales: the magnetic scale Δ_B, the density scale Δ_N, and the electric potential scale Δ_E. Since the shock is not in pressure equilibrium, the first two scales must not necessarily be proportional to each other. However, the electric field and density gradient might be related, so one expects that $\Delta_N \sim \Delta_E$ even though this is not necessarily so, in particular not when instabilities arise which cause very small scale electric field gradients. In principle one can distinguish three different cases [*Lembège et al*, 1999] which describe different physics:

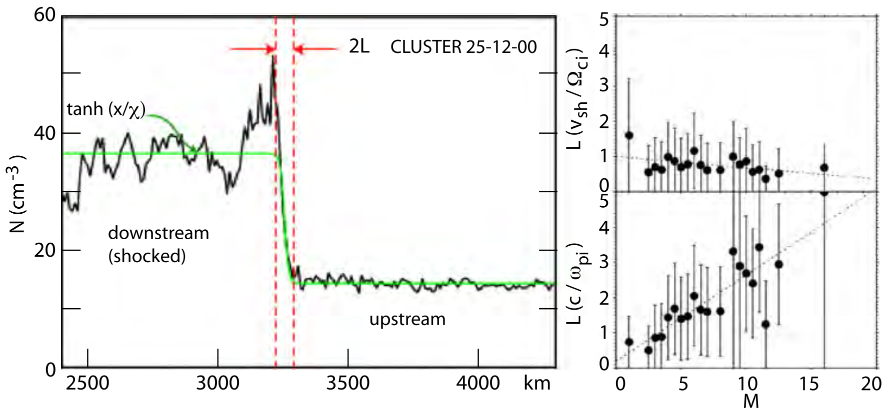

Figure 5.6: *Left*: Shock density transition-fit by a tanh-function in order to determine the shock-ramp transition scale [after *Bale et al*, 2003]. 98 of those shock transitions have been used in order to find a dependence of the shock ramp width from some physical parameter. *Right*: The dependence inferred by *Bale et al* [2003]. The *upper part* of the figure scales the dependence of the gyroradius with Mach number, the *lower part* the dependence of the ion inertial scale. Apparently there is no dependence of gyroradius on Mach number, while there is a clear linear dependence of the inertial scale on Mach number.

1. $\Delta_E \gg \Delta_B$. This is a case that has been reported to have been observed in Bow shock crossings [*Scudder et al*, 1986; *Scudder*, 1995]. The magnetic ramp is much steeper in this case than the structure of the electric field. The latter smears out over the foot and ramp regions. In this case the electrons will behave adiabatically, while the ions may be only partially or even non-magnetised.

2. $\Delta_E \sim \Delta_B$. In this case there will be a significant deviation from adiabatic behaviour of the electrons in the shock transition. Electron heating and motion will not be adiabatic anymore, and the electron distribution will significantly be disturbed [see, cf., *Balikhin et al*, 1995]. Observations of such cases have been reported [*Formisano & Torbert*, 1982].

3. $\Delta_E \ll \Delta_B$. This case which is also called the 'isomagnetic' transition [*Eselevich*, 1982; *Kennel et al*, 1985] corresponds to shock transitions with electrostatic substructuring which are sometimes also called subshocks.

The most recent *experimental* determination of the density transition scale has been provided by *Bale et al* [2003] using data from 98 Bow Shock crossings by the Cluster spacecraft quartet. The result is shown in Figure 5.6 for an example of this fit-determination by fitting a tanh-profile to the shock density transition. The point is that these authors found a dependence of the shock ramp transition on Mach number when the transition is scaled in ion inertial units, while there is no dependence when scaled in ion gyroradii. This scaling suggests that the shock scales with the gyroradius, since $(V/c)(\omega_{pi}/\omega_{ci}) \sim \mathscr{M}_A$.

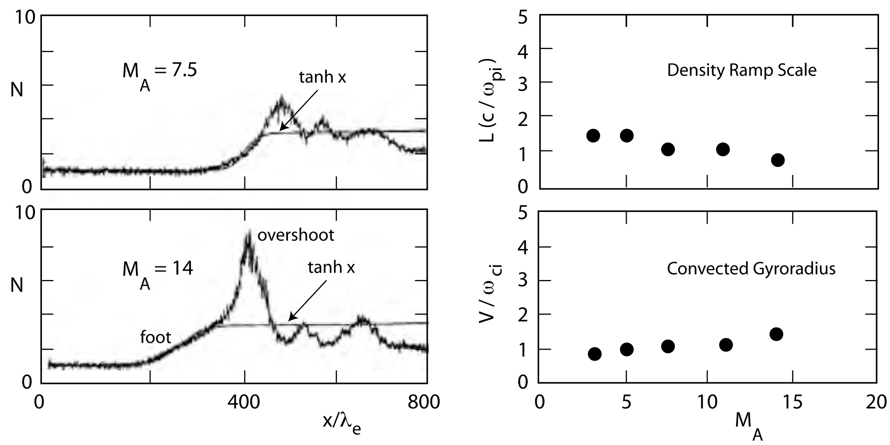

Figure 5.7: *Left*: Density profile in two full PIC simulations of large Mach numbers. Indicated is the pronounced overshoot and the long extended foot. The *straight lines* are tanh$x$-fits to the simulations showing the neglect of the overshoot and ramp during such fits which only account for the foot region. From fitting the ramp width the curves on the right are obtained. *Right*: Density ramp scales and convected ion gyroradii (in units of upstream inertial length) obtained in one-dimensional full particle PIC simulations of quasi-perpendicular shocks [after *Scholer & Burgess*, 2006] as function of Alfvénic Mach number. Use has been made of the full particle mass ratio 1838, $\Theta_{Bn} = 87^\circ$, and $\omega_{pe}/\omega_{ce} = 4$. The magnetic field used is that of the overshoot. One observes that the ratio of ion gyroradius to ion inertial length is constant. Also the scale of the ramp is about $\sim 1c/\omega_{pi}$, supporting a narrow ramp. The simulations also show that the scale of the ramp sharpens with increasing Mach number.

In order to check this behaviour numerically, *Scholer & Burgess* [2006] performed a series of one-dimensional full-particle PIC simulations with the correct mass ratio $m_i/m_e = 1838$ and for the Alfvénic Mach number range $3.2 \leq \mathscr{M}_A \leq 14$ and a shock normal angle $\Theta_{Bn} = 87^\circ$ in order to have a component of $k_\|$ parallel to **B**, but with small ratio $\omega_{pe}/\omega_{ce} = 4$ to compromise computing requirements. Figure 5.7 shows the results of these simulations. A tanh$x$-fit neglects in fact the entire ramp and takes account only of the foot region. Correcting the above described measurements it is thus found that the ramp thickness is just of the order of $\sim 1\,\lambda_i = c/\omega_{pi}$ and decreases slightly with increasing Mach number. However, from the form of the density profile it seems clear that the shock ramp is basically determined by the overshoot, and one must take the overshoot magnetic field value in calculating the gyroradius. The convected gyroradius based on the overshoot magnetic field $B_{\rm ov}$ and measured in λ_i is about constant very close to unity. Thus the shock ramp scale is given by the convective ion gyroradius based on the overshoot magnetic field. One should, however, note that the computing power in the simulations does not yet allow for larger ratios ω_{pe}/ω_{ce} which may affect the result. Moreover, higher dimensional simulations would be required to confirm the general validity of those calculation and conclusions.

Hence, combining the observations of *Bale et al* [2003] and the results of the simulation studies of *Scholer & Burgess* [2006] we may conclude that the scale of the shock foot is given by the upstream-convected ion gyroradius $r_{ci} = V/\omega_{ci,1}$ based on the upstream field B_1, while the scale of the shock ramp is given by the ramp-convected ion gyroradius $r_{ci,\mathrm{ov}} = V/\omega_{ci,\mathrm{ov}}$ based on the value of the magnetic field B_{ov} overshoot. This is an important difference which can be taken as a *golden rule* for estimates of the structure of quasi-perpendicular shocks even though, of course, these values are dynamical values which change from position to position across the foot and ramp. The scale differences are the reasons for the large upstream extension of the foot and the relative steepness of the shock ramp.

The observed constancy of the overshoot magnetic field-based convective ion gyroradius $r_{ci} \propto V/B_{\mathrm{ov}}$ with Mach number $\mathscr{M}_A \propto V$ can be understood when considering the about linear increase of the overshoot magnetic field $B_{\mathrm{ov}} \propto \mathscr{M}$ with Mach number (or with upstream velocity V) which holds for supercritical Mach numbers $\mathscr{M} > \mathscr{M}_{\mathrm{crit}}$ as long as $\mathscr{M}$ is not too large. At very large – but still non-relativistic – Mach numbers $\mathscr{M} < \mathscr{M}_{\mathrm{max}}$ the increasing steepness of the shock ramp and the increasing extension of the foot ultimately lead to the excitation of smaller scale structures in the ramp and the foot, which smear out any further increase in the overshoot.

The generation of these structures by a variety of instabilities might even turn the shock foot and ramp regions into regions where large anomalous collisions and thus resistances are generated as the result of wave-particle interactions. In this case the shock returns to become resistive again due to preventing large numbers of reflected ions from passing across the steep shock ramp and large shock potential, using the kinetic energy of the reflected particle population for the generation of a broad wave spectrum which acts to scatter the particles around in the foot and ramp regions and, possibly, also up to some distance in the transition region behind the ramp. This kind of confinement of reflected particles over long times will then be sufficiently long for providing the heating and dissipation which is required for sustaining a resistive shock which, then, is the result of the combined action of ion viscosity and anomalous resistivity, i.e. anomalous collisions. In addition, the scattering of the trapped reflected particle population necessarily results in plasma heating, and some particles will become accelerated to high velocities in these interactions as well. It is then possible that these particles provide the seed population for energetic particles which have been accelerated to high energies in the well-known shock-Fermi-one and shock-Fermi-two acceleration mechanisms.

So far the range of Mach numbers $\mathscr{M}_{\mathrm{max}} < \mathscr{M} < \mathscr{M}_{\mathrm{rel}}$ where this will happen is unknown, as it is hardly accessible to numerical simulations. However, the available simulations seem to point in this direction as long as the Mach numbers remain non-relativistic. In relativistic shocks with $\mathscr{M} = \mathscr{M}_{\mathrm{rel}}$ different effects arise which are not subject to our discussion at this place.

5.2.3 Shock Reformation

It has already been mentioned several times that supercritical shocks do under certain conditions reform themselves periodically – or quasi-periodically –, which is kind of a non-stationarity of the shock that does not destroy the shock but, at the contrary, keeps it intact in a temporarily changing way. We will come later to the problem of real non-stationarity.

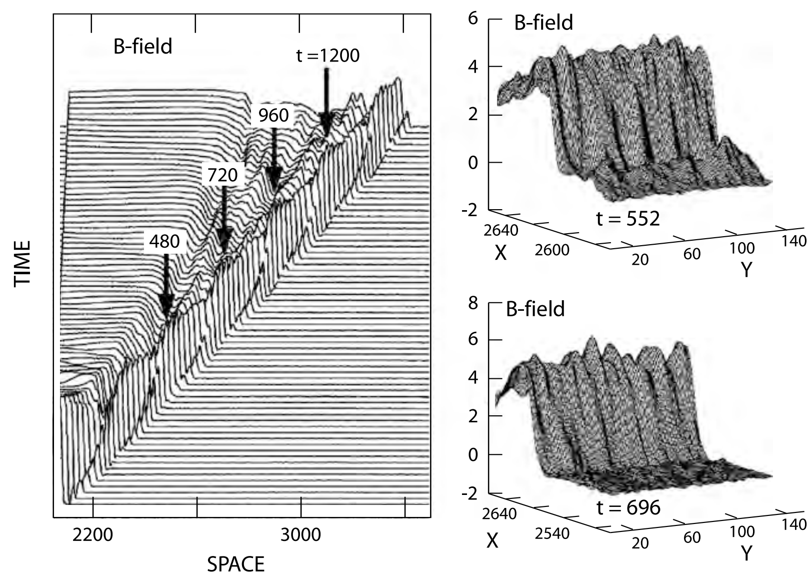

Figure 5.8: Magnetic field from full particle PIC simulations of shock reformation [after *Lembège & Savoini*, 2002, courtesy American Geophysical Union]. *Left*: Reformation cycles of the magnetic field in the shock. Time is measured in inverse electron plasma frequencies ω_{pe}^{-1}. The reformation times are indicated by the *arrows* in the plot with time given when the cycle is complete. *Right*: Two snapshots in time of the view of the shock front in the magnetic field at reformation. The interesting finding is that the front in this two-dimensional view is not a smooth plane but is quite distinctly structured in space and at the same time evolving.

Reformation in One Dimension: Mass Ratio Dependence

Reformation of quasi-perpendicular shocks is thus an important shock property which is closely related to highly super-critical shocks and the formation of a foot region, i.e. to the reflection of ions from the shock ramp.

In fact, reformation was already observed by *Biskamp & Welter* [1972] in the early short-simulation time PIC simulations shown in Figure 5.5, where we have noted it explicitly. Reformation of quasi-perpendicular shocks has also been reported, for instance, by *Lembège & Dawson* [1987a], *Lembège & Savoini* [1992, 2002], *Hellinger et al* [2002] and others who all used small ion-to-electron mass ratios. For illustration, Figure 5.8, on its left, shows a low mass-ratio example of the temporary evolution of a shock during shock reformation in a magnetic field stack plot. On its right the structure of the shock ramp at two different two reformation times is plotted along the shock ramp. There is a distinct reformation cycle in this simulation and also a distinct structure of the ramp/shock front in the tangential direction which is far from being smooth, a fact to which we will return during discussion of non-stationarity of shocks. The shock not only reforms cyclically in time, it also develops ripples along its surface which travel like waves along the shock.

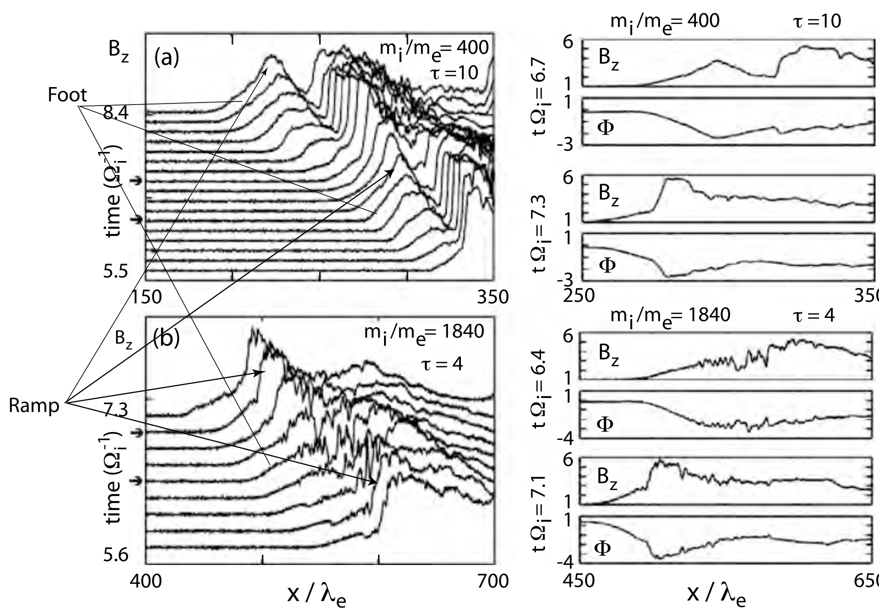

Figure 5.9: *Left*: One-dimensional PIC simulations [after *Scholer et al*, 2003, courtesy American Geophysical Union] of quasi-perpendicular $\Theta_{Bn} = 87°$ shock reformation for mass ratios $m_i/m_e = 400$ and 1840. Time is in ω_{ci}^{-1} (here denoted as Ω_i^{-1}), space in $\lambda_e = c/\omega_{pe}$. The parameter $\tau = \omega_{pe^2}/\omega_{ce}^2$ is taken small in both cases. The higher mass ratio shows a violent time evolution because of the high electron mobility. Reformation of the shock is due to evolution of the shock feet. The original foot region builds up until becoming itself the shock assuming the role of the ramp. Afterwards a secondary foot evolves in front of this new ramp. *Right*: Spatial shock profiles at two time sections (*see arrows on the left*). The higher mass ratio run shows a more subtle structure in B_z and shock potential Φ, but the gross features are similar. The potential drop exists already in the foot but the main drop occurs in the ramp. The lower mass ratio has a more concentrated foot region.

Full particle electromagnetic PIC simulations with realistically large mass ratios have been performed only very recently [*Matsukiyo & Scholer*, 2003; *Scholer et al*, 2003; *Scholer & Matsukiyo*, 2004] and only in one spatial dimension, showing that reformation at least occurs at small ion-$\beta_i \sim 0.2$. In these simulations the shock is produced by injecting a uniform plasma from $-x$ and letting it reflect from a stationary wall at the right end of the simulation box. The plasma carries a uniform magnetic field in the (x,z)-plane, and the plasma is continuously injected in the $+x$-direction. Since the right-hand reflecting boundary is stationary the shock, which is generated via the ion-ion beam instability in the interaction of the incoming and reflected ion beams, moves to the left at velocity given by the supercritical shock Mach number $\mathscr{M}_A \sim 4.5$. The upstream plasma has $\beta_i = \beta_e = 0.05$, and the shock normal angle is $\Theta_{Bn} = 87°$.

Two runs of these simulations are shown in Figure 5.9, one is for a mass ratio of 400, the other for a mass ratio of 1840. The left-hand side of the figure shows stack plots of time profiles of the nearly perpendicular magnetic field B_z with time running in equidistant units upward on the ordinate. Since the plasma is injected from the left and reflected at the right boundary the shock is seen to move from the right to the left in this pseudo-three-dimensional representation. Time is measured in ion cyclotron periods ω_{ci}^{-1}, while space on the abscissa is in units of the electron inertial length c/ω_{pe}. The magnetic profiles are strikingly similar for both mass ratios. In both cases a relatively flat foot develops in front of the steeper shock ramp caused by the shock reflected ions. The magnetic field of this foot starts itself increasing with time with growth being strongest close to the upstream edge of the foot until the foot field becomes so strong that it replaces the former shock ramp and itself becomes the new and displaced shock ramp.

This is seen most clearly in the upper low mass-ratio part of the figure. The foot takes over, steepens and becomes itself the shock. One can recognise in addition that, even earlier, the intense foot already had started reflecting ions by himself and developing its own flat pre-foot region. This pre-foot evolves readily to become the next foot, while the old ramps become part of the downstream turbulence.

During this reformation process the shock progresses upstream from right to left. This progression is not a continuous motion at constant speed. Both the foot and the ramp jump forward in steps. One such step ahead is seen, for instance, at time $t\omega_{ci} = 7.6$. Sitting in the shock frame one would experience some forward acceleration at this time, seeing the ramp moving downstream as a magnetic wave front the apparent source of which is the instantaneous shock ramp, while it is just the old shock foot. Hence the shock ramp and shock overshoot act as a source of a pulsating magnetic waves that are injected downstream from the shock with periodicity of roughly $\Delta t \sim 1.8\omega_{ci}^{-1}$ (for $m_i/m_e = 400$) and add to the downstream turbulence.

The realistic mass-ratio run in the lower part on the left also shows reformation of the shock. However there are some differences. First, the magnetic profiles are much stronger disturbed exhibiting much more structuring. Second, the foot region is considerably more extended in upstream direction. Third, the ramp is much steeper, and reformation is faster, happening on a time scale of $\Delta t \sim 1.3\omega_{ci}^{-1}$, roughly 30% faster than in the above case. Reformation is, however, more irregular at the realistic mass ratio with the property of reforming the shock ramp out of a long extended relatively smooth shock foot which exhibits pronounced oscillations.

The right-hand side of the figure shows two shock profiles at constant times for the two different mass-ratio simulations. The first profile at $t\omega_{ci} = 6.7$ has been taken when a well developed foot and ramp had been formed on the shock, the second profile at $t\omega_{ci} = 7.3$ is at the start of the new foot towards the end of the simulations. At the low mass ratio the foot profile is quite smooth showing that the foot is produced by the accumulation of reflected ions at the upstream edge of the foot where the ions have the largest velocity in direction y along the shock. This is where, during their upstream gyration in the upstream magnetic field, they orbit about parallel to the upstream convection electric field and gain most energy.

Hence, here, the current density is largest due to the accumulation of the reflected ions, due to the retardation of some ions from the inflow already at this place, and due to the speeding up of the reflected and retarded ions in y-direction by the convection electric field

E_y. All this leads to a maximum in the current density j_y and thus causes a maximum in the magnetic field B_z close to the upstream edge of the foot.

Most interestingly, the electric potential exhibits its strongest drop right here in the foot region with a second but smaller drop in the ramp itself. It is the electric field that belongs to this potential drop that retards the inflow already before it reaches the shock ramp. At the contrary, when the shock ramp is well developed, the main potential drop is for short time right at the ramp and extends even relatively far into the downstream region.

For the realistic mass ratio the foot- and ramp-transitions are both highly structured at $t\omega_{ci} = 6.4$ exhibiting fluctuations in both the magnetic field and electric potential, but the electric potential drop extends all over the foot region with nearly no drop in the ramp. When the ramp has been reformed at $t\omega_{ci} = 7.1$, the foot region still maintains a substantial potential drop, but 50% of the total drop is now found in the ramp with the downstream potential recovering. This is interesting as it implies that lower energy electrons will become trapped in the overshoot region, an effect which is much stronger for the large mass-ratio than for small mass-ratios and thus closer to reality.

Some recent one-dimensional full particle PIC simulations by *Umeda & Yamazaki* [2006] at Mach number $\mathscr{M}_A = 10$ and medium mass ratio $m_i/m_e = 100$ throw additional light on the reformation process when keeping in mind that reformation is not as strongly dependent on the mass ratio as originally believed. Figure 5.10 shows a collection of their results which this time are represented in the shock frame of reference.

The simulations have been performed by assuming an initial Rankine-Hugoniot equilibrium in the PIC code. The non-physicality of this initialisation is manifested in the initial evolution over the first few ion cyclotron periods. During this time the simulation adjusts itself to the correct physics, and the non-physical disturbance decays. The shock frame has shifted by this to a new position, which in the shock frame is located farther downstream (which takes into account of the moment transferred to the shock by the reflection of the upstream ions who lower the shock speed).

The further evolution of the shock shows the quasi-periodic reformation and the play between the foot and the ramp formation. The periodicity is roughly $\sim 10\omega_{ci,2}^{-1}$. When the foot takes over to become the ramp, the ramp jumps ahead in a fraction of this time. Afterwards the formation of the foot retards the ramp motion, and the ramp softens and displaces itself downstream to become a downstream moving spectrum of magnetic oscillations which is injected into the downstream region in the form of wave packets. The various plasma parameters in the left part of the figure show in addition the compression of plasma and field, and the dominance of perpendicular ion heating which is, of course, due to the accelerated foot ions which pass into downstream.

Two-Dimensional Reformation: Whistlers and Mach Number Dependence

First two-dimensional simulations of a strictly perpendicular $\Theta_{Bn} = 90^\circ$ shock formation have recently been performed by *Hellinger et al* [2007]. These simulations were intended to study the reformation process in two dimensions when the perpendicular shock is supercritical. Since PIC simulations are very computer-time consuming, most of the simulation runs by *Hellinger et al* [2007] used a two-dimensional hybrid code with the shock being

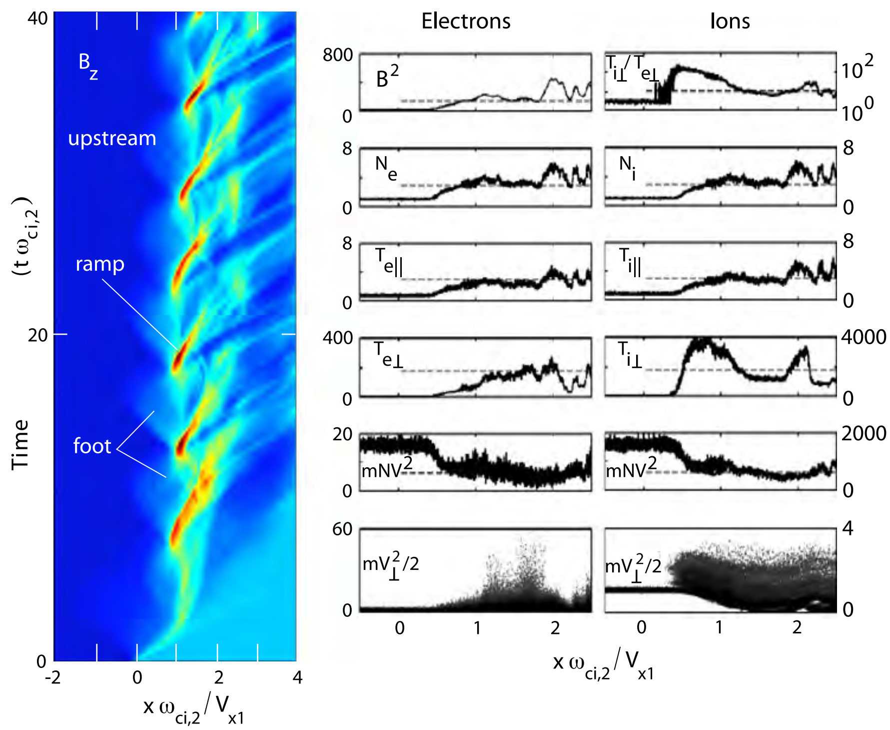

Figure 5.10: *Left*: Evolution of the magnetic field in a quasi-perpendicular high Mach number $\mathscr{M}_A = 10$ PIC simulation [after *Umeda & Yamazaki*, 2006]. Here the presentation is in the shock frame of reference, and the shock has been initialised by assuming Rankine-Hugoniot initial jump conditions. The non-physical nature of this assumption is visible in the initial evolution and fast displacement of the shock to the right. After the initial unphysical disturbance has disappeared a self-consistent physical state is reached in which the shock quasi-periodically reforms itself. The competition between the shock foot and ramp formation is nicely seen in the colour plot of the magnetic field B_z. *Right*: Electron and ion plasma parameters in computational units. Of interest is only their relative behaviour, not the absolute values. The profiles are taken at time $t\omega_{ci,2} = 38.1$. They show the compression of the plasma and heating of electrons and ions. Parallel electron and ion heating is comparable, but ions are heating much stronger than electrons in perpendicular direction causing a large perpendicular temperature anisotropy downstream of the shock.

generated by a magnetic piston as in the case of the simulations by *Lembège & Dawson* [1987a]. The interesting result of this simulation study was that no shock reformation was found while phase locked whistlers were detected which formed a characteristic interference pattern in the shock foot regions. This result is surprising as for strictly perpendicular shocks no whistlers should be generated according to the one-dimensional theory [see the above discussion on whistlers and, e.g., *Kennel et al*, 1985; *Balikhin et al*, 1995].

In order to cross check their hybrid simulation results *Hellinger et al* [2007] also performed a two-dimensional PIC [*Lembège & Savoini*, 1992] simulation choosing a mass

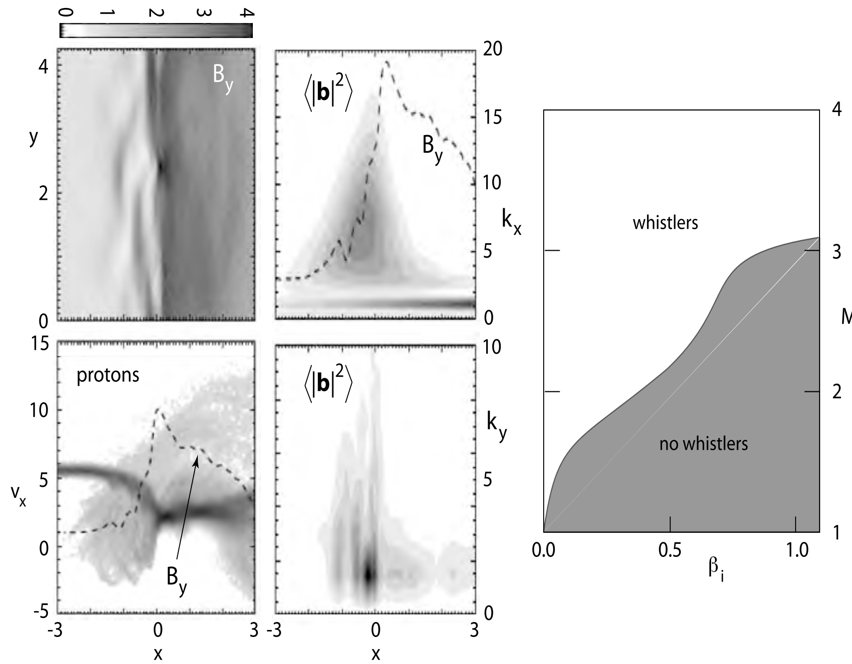

Figure 5.11: *Left*: Two-dimensional PIC simulations [after *Hellinger et al*, 2007, courtesy American Geophysical Union] of the end time $\omega_{ci}t = 28$ of the evolution of a *strictly perpendicular* shock using $m_i/m_e = 400$. Shown is the magnetic structure in the (x,y)-plane, the proton phase space (x,v_x) and the power of magnetic fluctuations in dependence on space x and wave numbers (k_y,k_x). Lengths are measured in ion inertial lengths c/ω_{pi}, velocities in Alfvén speeds V_A, wave numbers in inverse ion inertial lengths ω_{pi}/c. Magnetic fields and powers are in relative units (see *grey scale bar*). No shock reformation is seen in the *upper panel* of B_y on the left. A periodic foot evolves periodically causing a higher and steeper ramp overshoot when its cycle ends, but the shock ramp does not become exchanged with a new ramp. Note also that the next foot cycle begins before the end of the former cycle, i.e. the shock foot itself reflects ions. The power spectra show a periodic spatial spectrum of whistlers standing in and restricted to the shock foot. Periodicity in k_y is caused by interference between outward and inward moving whistlers. The proton phase space shows the retardation of the incoming flow in the shock foot, the occurrence of reflected ions in the foot and the heating of foot ions. Forward heating is also seen in the overshoot. *Right*: A parametric (2D-hybrid simulation) investigation of the evolution of phase locked whistlers in the shock foot in dependence on Mach number $\mathscr{M}_A$ and β_i. Large Mach numbers and small β_i support the excitation of standing whistlers.

ratio $m_i/m_e = 400$, Mach number $\mathscr{M}_A = 5.5$, electron plasma-to-cyclotron frequency ratio $\omega_{pe}/\omega_{ce} = 2$, upstream $\beta_e = 0.24$, $\beta_i = 0.15$ and 4 particles per cell. The results of this simulation have been compiled in Figure 5.11, showing only the PIC simulations and no hybrid simulations. Deviating from the former one-dimensional simulations by *Matsukiyo & Scholer* [2003] the magnetic field is in y. The block consisting of the four panels on the left in the figure are the simulation results at the end of the simulation run, showing the compression of the magnetic field B_y in the (x,y)-plane, proton velocity space (v_x,x) – only the normal velocity component is shown –, and the average magnetic fluctuation spectra $\langle b^2 \rangle$ as functions of wave number components k_x, k_y. As the authors describe, after a short initial time when the shock foot forms and the shock reforms, reformation stops and does not recover again in these two dimensional run. Instead, the shock foot starts exhibiting large magnetic fluctuations. These are seen in the low-frequency magnetic power spectra being confined solely to the shock foot (as recognised from the B_y-profile) as seen from the k_x dependence of the magnetic power spectrum and forming an interference pattern in k_y.

These fluctuations are identified as whistler waves propagating obliquely (in k_x and k_y) across the foot and the magnetic field. Since $k_x \sim 3k_y$ their perpendicular wave numbers are large, they are quite oblique, and their parallel wavelengths are long. They are excited in the foot and because of their obliqueness probably propagate close to the resonance cone. Their main effect is to resonantly suppress shock reformation by inhibiting the ions to accumulate in the foot. Hence, under the conditions of these simulations the shock turns out to be stable and does not reform. It maintains its structure thanks to the generation of oblique whistlers in the shock foot which dissipate so much energy that the shock becomes about resistive. In one-dimensional simulations this regime has not been seen and is probably inhibited for strictly perpendicular shocks. In two-dimensional simulations, on the other hand, the additional degree of freedom provided by the introduction of the second spatial dimension allows for the generation of the whistlers which are suppressed in the one-dimensional case (where $\mathbf{k}$ has only the component k_x).

Guided by these simulations *Hellinger et al* [2007] have undertaken a parametric study of the regime where whistler excitation and thus presumably stationary shock structures lacking reformation should exist. Their results are given on the right in Figure 5.11 in $(\beta_i, \mathscr{M}_A)$-space. According to this figure, whistlers will not be excited at low Mach numbers. Here the two-dimensional perpendicular shocks will reform. At higher Mach numbers whistlers should be excited, and the shock should become stabilised in two dimensions.

This surprising result suggests that sufficiently high Mach numbers are needed in order to excite whistlers; on the other hand, when the Mach number will become large (*Hellinger et al* [2007] investigated only the range of Mach numbers <5) then other effects should set on, and the shock should become non-stationary with whistlers becoming unimportant and reformation becoming possible again.

5.3 Ion Dynamics

Until now we have avoided discussing the behaviour of particles in the simulations. The mere idealised reflection process we have already discussed, as far as this could be done analytically. The complicated geometry and dynamics of particle motion in shocks necessitates to return to simulations.

We have mentioned that reflected particles are forming a foot on the shock and may contribute to the reformation of the shock. We have, however, not yet gone into detail and into the investigation of the relation of the particle distributions in phase and real space observed in the simulations and their relation to the shock dynamics. This will be done in the present section for the ions on the basis of simulation studies.

5.3.1 Ion Dynamics in Shock Reformation

The two plots on the right-hand side of Figure 5.5 show phase space representations of ions in the early simulations of shock formation by *Biskamp & Welter* [1972] at $t\omega_{ci} = 3$ close to the end of the simulation. The first box is the dependence of the ion velocity v_x on position x (direction of inflow), the second plot the transverse ion velocity component v_y. Each macroparticle present in the box is identified by a dot. Hence high particle phase space density is reflected by accumulation of many such dots. The plasma enters the central region of the box from left at high positive speed v_x and $v_y = 0$ and leaves the central region to the right at high density and very low speed v_x. The inflowing plasma was extended relatively narrow in v_x indicating low temperature. The shocked plasma distribution is broader thus having higher temperature. Moreover, some of the ions are seen to be smeared out from large positive up to large negative velocities in v_x indicating that strong particle scattering has occurred and that there are particles of high velocity in both directions being equivalent to heated plasma. In the foot region the closed circle in the particle distribution signifies the presence of the reflected trapped ions which are accelerated in both direction. their presence decelerates the inflow as can be seen by the drop in the velocity v_x just before entering the closed loop trapped ion region. The reflected particles are seen on the left of this closed loop having negative speeds in v_x therefore being directed upstream. The (v_y, x)-box shows that the reflected and trapped ions gyrate and are accelerated into y-direction. Also many of the ions downstream of the shock possess nonzero v_y velocity components, some of the large, indicating acceleration along the shock front.

Even though it seems clear from this figure that reflected ions are involved into shock reformation and the dynamics of the shock profile, the process remained to be unclear until simulations at higher resolution and much higher mass ratio had been performed. Figure 5.9 gave a clearer idea of the ion dynamics. The corresponding ion phase space plots are shown in Figure 5.12 for the two mass ratios $m_i/m_e = 400$ (top) and 1840 (bottom) respectively. Both plots show just the enlarged shock foot transition region over the same scale of $100c/\omega_{pe}$. The electron $\beta_e = 0.2$ has been kept constant in both simulations, while the ion β_i has been changed. Only the normal component of the ion velocity is shown for the nearly perpendicular supercritical shock. In both plots the magnetic field B_z has been drawn as a thin continuous line showing the magnetic shock profile over the spatial distance Δx.

The upper (low-mass-ratio) low-β_i panel shows the cold dense ion inflow at velocity $v_{ix} \sim 5$ (in units of the upstream Alfvén velocity) being retarded to nearly Mach number 1 already when entering the foot. This retardation is due to its interaction with the intense but cold (narrow in velocity space) reflected ion beam which is seen as the narrow negative v_{xi}-velocity beam originating from the shock ramp. This reflected ion beam needs a certain distance to interact with the upstream plasma inflow. This distance is the length the beam-beam excited waves need to grow. But once the interaction becomes strong enough, the

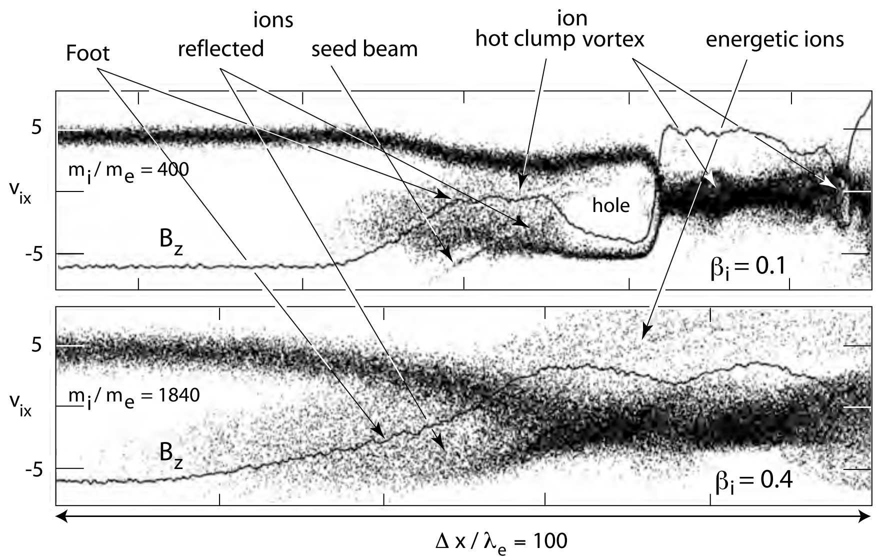

Figure 5.12: Ion phase space for two simulations of supercritical quasi-perpendicular shock formations for same Mach number and $\beta_e = 0.2$ but different mass ratios and β_i [after *Scholer et al*, 2003, courtesy American Geophysical Union]. *Top*: Foot formation and shock reformation in a low-β_i shock simulation. The reflected ion beam accumulates in the shock foot forming a hot clump-vortex ion distribution which causes scattering of the reflected and upstream ions and generates a high foot magnetic field. The hole of the vortex corresponds to low magnetic field, the ring to large magnetic fields. When the foot field further increases it takes over and becomes the new ramp. At this time the ramp position jumps from the current position to that of the foot edge thereby reforming the shock. Such former reformation cycles can be recognised in the downstream distribution as remains of ion vortices (holes) in the otherwise hot downstream distribution. *Bottom*: The same simulation with realistic mass ratio but large $\beta_i = 0.4$. No reformation and no ion vortex is observed. Instead, the foot ions because of their high temperature smear out the entire gap between the original inflow and the reflected ion beams. Note also the occurrence of a large number of downstream diffuse energetic ions in this case.

reflected ions are scattered by the waves into a hot ion clump in addition to being turned around by gyration. Both effects cause a reduction in velocity v_x of the reflected ions which, being accelerated by the convection electric field, turn to flow in y direction and cause the magnetic bump that develops in this region of the foot. It is interesting to remark that in the (v_x, x)-plane the reflected ions close with the upstream flow into an hot ion ring distribution (vortex) just in front of the ramp of which the hot ion clump that brakes the inflow is the upstream boundary. Behind the ramp, which is the point of bifurcation of the ion distribution, i.e. the location where the reflection is at work, a broad hot ion distribution arises which at some locations shows rudimentary remains of ion vortices from former reformation cycles. Their magnetic signatures are the dips seen in the magnetic field. The next reformation cycle can be expected to completely close the ion vortex in the foot and to transform the ramp from its current position to the position of the foot. The first sign of this process is already seen in the foot ion distribution, which shows the birth of a faint new reflected ion beam at high negative speeds. This beam is not participating in the formation of the ring but serves as the seed of the newly reflected population.

The same behaviour is found in large mass ratio simulations as long as β_i is small. This is obvious from the large mass-ratio magnetic field shown in Figure 5.9. As long as β_i remains to be small, the shock undergoes reformations also for realistic mass ratios. In other words, as long as the plasma is relatively cool the real shocks found in nature should develop feet which at a later time quasi-periodically become the shock ramp.

This changes completely, when β_i increases as is suggested from consideration of the lower panel in Figure 5.12. There a realistic mass ratio has been assumed, but $\beta_i = 0.4$, and no reformation is observed, at least not during the realisable simulation times. Instead, the shock develops a very long foot region that is extended twice as far into the upstream region as in the low-β_i case. Clearly, the high ion temperature smears out the reflected ion population over the entire gap region between the upstream and reflected beam regions, and no vortex can develop. This implies that the foot remains smooth and does not evolve into a ramp.

However, inspecting the panels of Figure 5.12 it becomes immediately clear that suppression of reformation is a relative process. Reformation will be suppressed only when the thermal speed v_i of the ions is large enough to bridge the gap between the reflected and incoming ion beams, i.e. large enough to fill the hole. Semi-empirically one can establish a condition for shock reformation as $v_i < \alpha V_{n1}$ when taking into account that the normal speed of incoming ions is simply specularly turned negative. Since this is never exactly the case, the coefficient will roughly be in the interval $1.5 < \alpha < 2$. This condition for reformation to occur can be written as

$$\mathcal{M}_\mathrm{A} > \frac{\beta_i^{\frac{1}{2}}}{\alpha} \tag{5.20}$$

where the Alfvénic Mach number is defined on V_{1n}. The larger the Mach number becomes the less suppression of reformation will play a role, and at high Mach numbers one expects that either reformation becomes a normal process or that other time-dependent processes set on which lead to a non-stationary state where the shock reformation becomes a chaotic and unpredictable process. As we have argued earlier this is quite normal as the shock is thermodynamically and thermally in a non-equilibrium state: it is a region where electrons and ions have violently different temperatures; it is not in pressure equilibrium; upstream and downstream temperatures are different; and it hosts a number of non-Boltzmannian phase space distributions all concentrated in a small volume of real space. Under such conditions stationary states suppressing reformation [advocated e.g. by *Hellinger et al*, 2007] will occur only very exceptionally.

Hada et al [2003] recently attempted to semi-empirically determine the fraction of reflected ions needed for reformation to occur. They performed a large parametric search based on hybrid simulations by changing the Mach number and determined the fraction of reflected ions in the foot when reformation occurred. Their result is shown in Figure 5.13 for cold electrons $\beta_e = 0$ (assuming that electrons do not contribute to reformation and reformation being exclusively due to ion-viscosity, and for fixed thermal velocity of upstream and reflected ions $v_i/\omega_{pe}\mathrm{d} = 0.2$, where d is the spatial simulation-grid spacing). The latter

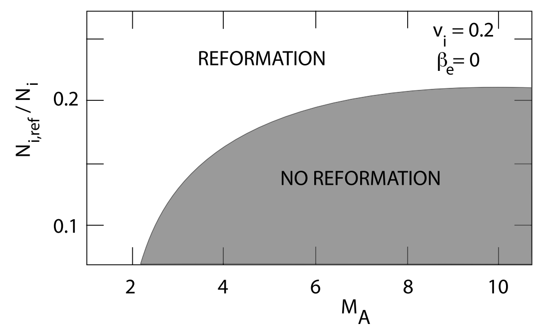

Figure 5.13: Parametric determination of the fraction of shock-reflected ions in the foot of a quasi-perpendicular shock as function of Alfvénic Mach number for the special case of $\beta_e = 0$ and ion thermal velocities $v_i = 0.2$ measured in ω_{pe}d, where d is the numerical grid spacing [after *Hada et al*, 2003, courtesy American Geophysical Union].

restriction is certainly not satisfied as the realistic mass ratio simulations show. Therefore these results must be taken with caution.

5.3.2 Ion Instabilities and Ion Waves

So far we have described the field and particle properties as have been observed in simulations of quasi-perpendicular supercritical shocks. It has become obvious that in the different regions of the shock transition the particle distributions carry free energy. This is true for the foot region, the shock transition and overshoot as well as the downstream region. And it is true for both species, electrons and ions. This free energy is the source of a number of instabilities which excite waves of different kinds in the various shock transition regions which can be measured. Figure 5.14, taken from *Gurnett et al* [1979], shows an example of such measurements when the ISEE-1 spacecraft crossed an interplanetary shock travelling outward in the solar wind. The passage of the shock over the spacecraft is seen in the wave instrument in the various channels as a steep increase of the power spectral density of the electric field which is highest in the crossing of the ramp and at medium frequencies of a few 100 Hz under the conditions of the crossing. After the crossing took place the wave power in the downstream region of the shock still remained high but was lower than during the shock crossing. In the right part of the figure the different electric wave power spectra are shown in their time sequence as a stack plot. From this plot the dramatic increase of the power in the medium frequencies during the crossing is nicely visible. Most of the waves excited in this frequency range are caused by electron-ion instabilities which we will discuss in the next section.

The free energy source of the instabilities is less the temperature anisotropy than the direct differences in bulk flow properties of the different species components. We therefore ignore the temperature anisotropy differences even though such instabilities may arise, in particular when ion-whistlers are excited of which we know that they can be driven

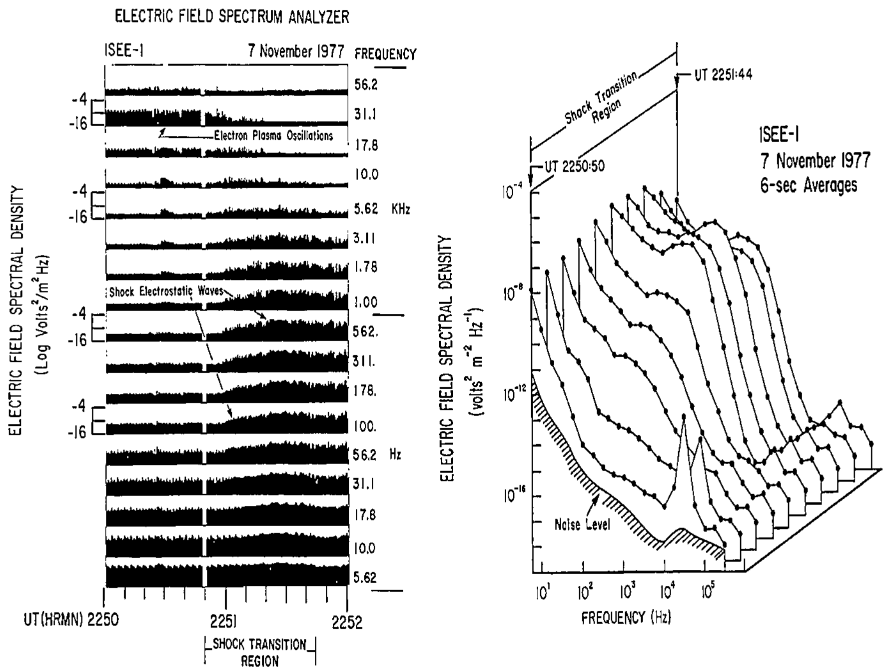

Figure 5.14: Electric wave spectra measured during the spacecraft crossing of an interplanetary shock [after *Gurnett et al*, 1979, courtesy American Geophysical Union]. *Left*: Power spectra (in V^2/m^2 Hz) with respect to time in a number of frequency channels. The spacecraft approaches the shock from left and crosses over it. The increase in power is well documented from low to high frequencies when coming into the shock transition region. *Right*: A sequence of shock electric spectra during this crossing given as power spectral density with respect to frequency. The dramatic increase of the low frequency wave power is seen when the spacecraft approaches and crosses over the shock. Behind the shock the power remains high but lower than in the transition region. The Bump around a few 100 Hz is the most interesting from the point of view of instability. These waves are excited by electron-ion instabilities discussed in the next section.

by a temperature anisotropy. To some extent the occurrence of two (counter-streaming in direction x of the shock normal) ion beams already fakes a bulk temperature on the ion component thus generating some relationship between a two-beam situation and a temperature anisotropy. Similarly transversely heated reflected ions superposed on a low perpendicular temperature inflowing ion background fakes a perpendicular temperature anisotropy. For our purposes, however, the bulk flow differences are more interesting and have, in fact, been more closely investigated right from the beginning [*Forslund & Shonk*, 1970; *Forslund et al*, 1970; *Papadopoulos et al*, 1971; *Wu et al*, 1984].

Foot Region Waves

Let us first consider the foot region. The free energy sources here are the relative drifts between the incoming electrons and reflected ions and the incoming electrons and incom-

Instability	Excitation by	Source of free energy	Direction of propagation
Ion-ion streaming instability	Reflected ions and transmitted ions	Relative streaming between the ion species	$(\mathbf{k} \cdot \mathbf{B}_0) = 90°$
Kinetic cross-field streaming instability	Reflected ions	Relative streaming between the reflected ions and the solar wind electrons	$0 < (\mathbf{k} \cdot \mathbf{B}_0) < 90°$ (In the coplanarity plane)
	Transmitted ions	Relative streaming between the transmitted ions and the electrons	$(\mathbf{k} \cdot \mathbf{B}_0) \leq 90°$ (In the coplanarity plane)
Lower-hybrid-drift instability	Reflected ions	(i) Relative cross-field drift between the reflected ions and the electrons (ii) Density gradient	$(\mathbf{k} \cdot \mathbf{B}_0) < 90°$ (Out of the coplanarity plane)
	Drifting electrons	(i) Relative cross-field drift between the electrons and the transmitted ions (ii) Density gradient	$(\mathbf{k} \cdot \mathbf{B}_0) < 90°$ (Out of the coplanarity plane)
Ion-acoustic instability	Transmitted ions	Relative streaming between the ion species and the electrons	$(\mathbf{k} \cdot \mathbf{B}_0) < 90°$ (Out of the coplanarity plane)
Electron-cyclotron drift instability	Drifting electrons	Electron drift relative to the solar wind ions	$(\mathbf{k} \cdot \mathbf{B}_0) \simeq 90°$ (Out of the coplanarity plane)
Whistler instability	Electrons	Electron thermal anisotropy $T_{e\perp} > T_{e\parallel}$	$(\mathbf{k} \cdot \mathbf{B}_0) \simeq 0°$

Figure 5.15: Instabilities in the Foot Region [copied from *Wu et al*, 1984].

ing ions. The presence of the reflected ions causes a decrease of the ion bulk velocity in the foot region. This implies that the incoming electrons are decelerated so that the current in shock normal direction is zero, i.e. the flow is current-free in normal direction. However, this has the consequence that a relative bulk velocity between electrons and reflected ions or electrons and incoming ions arises. These differences will contribute to the excitation of instabilities. Electrons are not resolved in hybrid simulations, however. In this section we will restrict to ion instabilities leaving the essentially more interesting ion-electron instabilities for the next section. A list of the most important instabilities in the foot region is given in Figure 5.15. This list has been complied by *Wu et al* [1984]. It is interesting to note that only a few of these instabilities have ever been identified in actual observations and in the simulations even though theoretically they should be present. This can have several reasons, too small growth rates, too strong Landau damping, for instance, in the presence of hot ions, convective losses or very quick saturation due to heating effects, competition with other waves or wave-wave interaction and so on.

The ion-ion instability [*Papadopoulos et al*, 1971; *Wu et al*, 1984] generates waves in the whistler/lower hybrid frequency range $\omega_{ci} \ll \omega\omega_{ce}$ as we have discussed in Chapter 3. Its energy source is the beam-beam free energy of two counter streaming ion beams, one the reflected ion beam, the other the inflow. As long as the wavelengths re shorter than the reflected ion beam gyroradius the instability is relatively high frequency and electrostatic close to perpendicular and at the lower hybrid frequency. However, at slightly longer wavelength the magnetisation of the ions comes into play and the instability generates electromagnetic whistlers. These are the whistlers which are observed at angles larger than the critical whistler angle mentioned earlier and probably also in the two-dimensional simulation case by *Hellinger et al* [2007] for the parameters used there. An important ion-driven instability in the foot region of quasi-perpendicular supercritical shocks is the whistler instability which we have already mentioned several times. It is related either to reflected ion beams, to assumed temperature anisotropies [as assumed to exist – though never been confirmed by observations – by *Wu et al*, 1984], or to result from diamagnetic density-gradient drifts in the lower-hybrid band as the electromagnetic branch of the lower-hybrid/modified two stream instability, the electrostatic part of which we will discuss in the next section on electronic instabilities and electron dynamics.

Hellinger et al [2007], in their two-dimensional hybrid simulations discussed above, have seen the evolution of whistlers without identifying their sources. Recently *Scholer & Burgess* [2007] performed an extensive parametric search for whistler waves in the foot region of oblique shocks between $60^\circ \leq \Theta_{Bn} \leq 80^\circ$, the region where in one-dimensional PIC simulations intense whistlers should become excited theoretically when reflected ions are present. This is the case for the more oblique but still quasi-perpendicular supercritical shocks. A wide range of Alfvénic Mach numbers was used, and strong excitation of whistlers in the parametric range was found indeed. We will discuss these observations here in more detail as they are the currently existing best available simulation results representing the current state of the art in the field of whistler excitation in connection with the formation, stability and time dependence of supercritical shocks at the time of writing this review.

Before discussing their results we briefly review the physics involved in the importance of whistlers in shock foot stability as had already been anticipated by *Biskamp & Welter* [1972] following a suggestion by *Sagdeev* [1966]. As we have mentioned earlier, a linear whistler wave precursor can stand in front of the quasi-perpendicular shock as long as the Mach number $\mathscr{M} < \mathscr{M}_{\rm wh}$ is smaller than the critical whistler Mach number

$$\mathscr{M}_{\rm wh} = \frac{1}{2}\left(\frac{m_i}{m_e}\right)^{\frac{1}{2}}|\cos\Theta_{Bn}| \quad \text{or nonlinearly} \quad \frac{\mathscr{M}_{\rm wh,nl}}{\mathscr{M}_{\rm wh}} = \sqrt{2}\left[1-\left(\frac{27\beta}{128\mathscr{M}_{\rm wh}}\right)^{\frac{1}{3}}\right] \tag{5.21}$$

The second expression results when including the nonlinear growth of the whistler amplitude during the steeping process [for the derivation of this expression see, e.g., *Kazantsev*, 1961; *Krasnoselskikh et al*, 2002]. The nonlinear critical whistler Mach number $\mathscr{M}_{\rm wh,nl}$ is larger by a factor of $\sqrt{2}$ than the whistler Mach number $\mathscr{M}_{\rm wh}$. It depends weakly on the plasma-β which has a decreasing effect on it, slightly reducing the whistler range.

For instance, with realistic mass ratio $m_i/m_e = 1840$ and $\Theta_{Bn} = 87°$ the whistler critical Mach number is quite small, $\mathscr{M}_{\rm wh} \simeq 1.14$. Otherwise no standing whistlers can thus be expected. It has also been speculated that above the above critical whistler Mach number the shock ramp is replaced by a nonlinear whistler wave train with wavelength of the order of λ_e. Approximating such a train as a train of whistler solitons one realises that the amplitude of the solitons increases with Mach number. Hence, the critical whistler Mach number in this case must become dependent on the whistler amplitude [*Krasnoselskikh et al*, 2002]. This leads to the slightly larger nonlinear whistler critical Mach number $\mathscr{M}_{\rm wh,nl}$ on the right in the above equation. At such realistic low Mach numbers the shocks are subcritical, however, and we are back to the problems discussed in Chapter 4.

Between the two Mach numbers $\mathscr{M}_{\rm wh} \leq \mathscr{M} \leq \mathscr{M}_{\rm wh,nl}$ the nonlinear whistler soliton train can exist attached to the ramp. However, when the nonlinear whistler Mach number is exceeded this is not possible anymore, and the whistler wave should turn over due to a so-called gradient catastrophe leading to non-stationarity of the shock front, which we will discuss later. In the simulations of *Biskamp & Welter* [1972] the simulation range was in favour of the excitation of whistlers which have also been seen and by these authors had been attributed to a nonlinear instability between the two ion beams and the electric field of a standing whistler wave an interpretation which is overturned by the new simulation results. *Scholer & Burgess* [2007] performed PIC simulations with physically realistic mass ratio. For all shocks with $\Theta_{Bn} \leq 83°$ the whistler critical Mach number is well above the critical Mach number such that the shock is supercritical. This is in order to check the excitation of whistlers in the different regimes of $\mathscr{M}$. In the left part of Figure 5.16 the Mach number is below the critical whistler Mach number, and in the shock foot region a group of phase locked whistler waves is excited with increasing amplitudes towards the shock ramp. This is nicely seen on the left in both the magnetic stack plot as also in the time profile in the second panel on the left from top. The whistlers slow the incoming flow V_{ix} down before it reaches the ramp. In the phase space plot the incoming and reflected beams are seen as is the scattering and trapping of the resonant ions in the whistler waves. The right part of the figure shows an identical simulation with Mach number above the critical whistler Mach number but below the nonlinear whistler Mach number. The stack plot shows two well developed reformation cycles with all signs of normal reformation. The magnetic field profile chosen in the second panel is at time $t\omega_{ci} = 7.6$ in the second reformation cycle when the foot loop is well developed. The magnetic field signature shows the distortion due to the foot which is caused by a large amplitude non-phase-standing whistler wave that evolves nonlinearly. However, the reformation is not due to this whistler but due to the accumulation of gyrating ions at the foot edge as known from previous simulations.

Near the ramp the ions become trapped in a large-amplitude whistler loop, as is seen in the phase space plot. The loop coincides with a minimum in the B_z-component of the magnetic field. The whistler, on the other hand, does practically not affect reformation, even though it structures the overshoot region. Reformation time is defined thus, as we know already, by the gyration time of ions in the foot, being of the order of a few ion-cyclotron periods. When the shock becomes more oblique, the whistler effect increases again at fixed Mach number as the Mach number enters the domain below critical whistler Mach num-

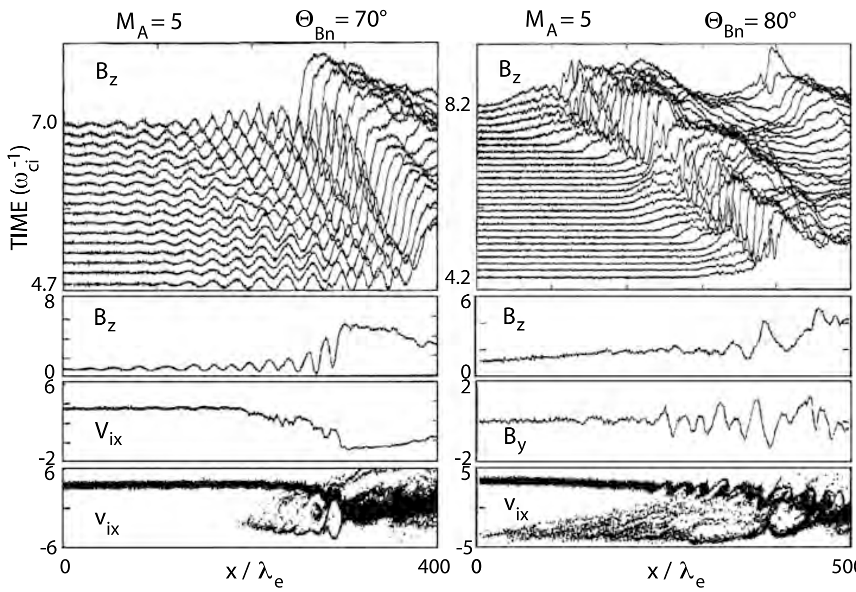

Figure 5.16: One-dimensional full particle PIC simulations with realistic mass ratio for the same Mach number but different angle $\Theta_{Bn} = 70°$ and $80°$ [after *Scholer & Burgess*, 2007]. *Left top*: Mach number $\mathscr{M} < \mathscr{M}_{\rm wh}$. The shock foot region is filled with waves of two polarisations, one of the expected standing whistler waves which interfere with the other kind of waves. No substantial shock reformation is observed in this case. *Right top*: Here the Mach number is in the range Mach number $\mathscr{M}_{\rm wh} < \mathscr{M} < \mathscr{M}_{\rm wh,nl}$. Two reformation cycles are visible during the simulation run in the magnetic field, and no whistler waves occur because the Mach number exceeds the first whistler Mach number. However there is also no nonlinearly steepened whistler in the shock front which is simply taken over by the foot after one reformation cycle. *Bottom three panels*: On the *left* shown the standing whistler oscillations in the magnetic field on the *left*, the decrease in the flow velocity when entering the foot due to the whistler scattering of the ions, and the particle phase space in $v_(ix)$ with the reflected beam and the scattered foot ions with little vortex formation such that the reformation is inhibited. On the *right* seen is the more irregular structure of the transition, the component B_y in the magnetic field and the accelerated foot ions in the absence of whistlers.

ber $\mathscr{M}_{\rm wh}$, and the shock transition becomes much more structured and reformation less important.

In order to see what kind of waves are excited during the whistler cycles, a separation of the magnetic wave spectrum B_y into positive B_y^+ and negative B_y^- helicity components has been performed for a $\mathscr{M}_A = 9$, $\Theta_{Bn} = 70°$ simulation run. Figure 5.17 shows the result. The negative helicity waves B_y^- propagate toward the shock, i.e. to the right. After correcting for the convection velocity which is also to the right, these waves turn out to be left-hand polarised. The lower panel shows positive helicity B_Y^+ waves propagating to the left, so they are upstream propagating waves and are also left-hand polarised. The positive helicity waves have longer wavelength than negative helicity waves. They propagate close to the shock speed upstream. They are thus almost standing in the shock frame. These are the

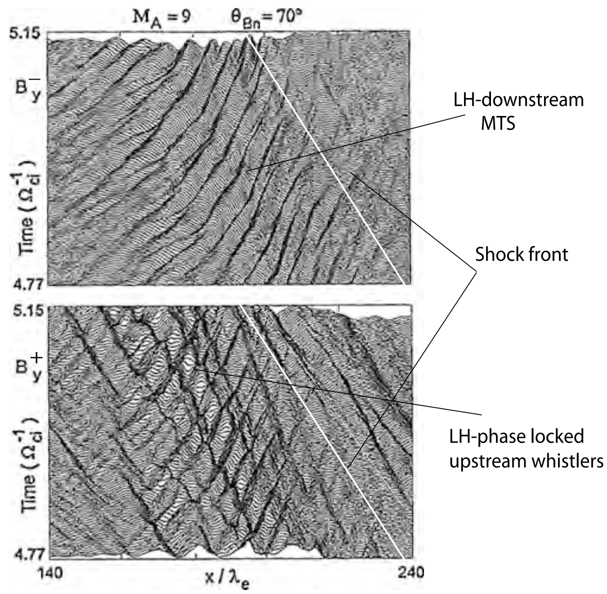

Figure 5.17: One-dimensional full particle PIC simulations with realistic mass ratio for Mach number $\mathscr{M}_A = 9$ and $\Theta_{Bn} = 70^\circ$ in the non-reformation whistler regime [after *Scholer & Burgess*, 2007]. *Top*: Negative helicity waves B_y^- propagating to the right are left-hand polarised short wavelength waves moving downstream toward the shock and being mostly absorbed in the shock transition. *Bottom*: Positive helicity waves B_y^+. These waves move upstream and thus are also left-hand circularly polarised waves. They move at shock velocity which identifies them as the phase-locked standing whistler precursors in the shock-upstream region with decaying upstream amplitude and long wavelength. Some interference is seen on these waves. Their left-hand polarisation identifies them as ion-beam excited whistlers and not as electron temperature anisotropy exited whistlers.

upstream left-hand polarised (ion beam and not electron temperature anisotropy driven) whistlers.

The downstream propagating negative helicity waves are no whistlers. They are caused in quite a different way which is related to the electromagnetic modified two-stream instability which we will discuss in the next section on electron waves.

Ramp Transition Waves

Stability of the ramp is a question that is not independent of the stability of the foot as both are closely connected by the reformation process of the quasi-perpendicular shock front. Since the suggestion of *Sagdeev* [1966] it is widely believed that the whistler waves excited in the foot are the main responsible for the stability of the foot and formation of the ramp by steeping. In fact, they might accumulate their, store energy in both magnetic and electric field, trap particles and excite different waves.

Instability	Nature of wave mode	Typical wavelength	Frequency and growth rate	Remarks
Ion-ion streaming instability	Magnetosonic waves	$k \sim \frac{\omega_e}{c}$	$\gamma \sim \Omega_i$	Stabilized when the streaming velocity exceeds the Alfvén speed.
Kinetic cross-field streaming instability	Whistler mode waves with oblique propagation	$k \gtrsim \frac{\omega_{\mathrm{LH}}}{V_0}$	$\omega \simeq \omega_{\mathrm{LH}}$ $\gamma > \Omega_i$ $\omega \simeq \omega_{\mathrm{LH}}$ $\gamma > \Omega_i$	The instability persists even if $V_0 \gg v_{\mathrm{A}}$
Lower-hybrid-drift instability	Lower hybrid waves and drift waves	$k \sim \frac{\omega_{\mathrm{LH}}}{V_0}$	$\omega \simeq \omega_{\mathrm{LH}}$ $\gamma \gg \Omega_i$	Instability enhanced by ∇T_e
	Doppler-shifted whistler mode	$k > \frac{\omega_{\mathrm{LH}}}{V_0}$	$\omega \simeq \omega_{\mathrm{LH}}$ $\gamma \gg \Omega_i$	
Ion-acoustic instability	Ion waves	$k\lambda_{\mathrm{D}} \lesssim 1$	$\omega \lesssim \omega_i$ $\gamma > \Omega_i$	Instability enhanced by ∇T_e
Electron-cyclotron drift instability	Doppler-shifted Bernstein waves and ion waves	$k\lambda_{\mathrm{D}} \lesssim 1$	$\omega \simeq n\Omega_e$ $\gamma > \Omega_i$	Instability suppressed by ∇B
Whistler instability	Whistler-mode waves with parallel propagation	$k \lesssim \frac{\omega_e}{c}$	$\omega \ll \Omega_e$ $\gamma \gg \Omega_i$	

Figure 5.18: Instabilities in the Ramp Transition [copied from *Wu et al*, 1984].

A very early and to large extent out of time list is given in Figure 5.18 of the theoretical expectations for possible instabilities in the shock ramp region [*Wu et al*, 1984]. As in the case of the foot region, the instabilities in the ramp which might be of real importance have turned out to not fit very well into the scheme of this listing. In both cases, the case of the foot and the case of the ramp, this disagreement reflects the weakness of theoretical speculation which is not supported by direct observations on the one hand and clear parametric searches in numerical experiments on the other.

Waves excited or existing in the ramp cannot be considered separate from the stability of the shock ramp. They are mostly related to electron instabilities and will to some extent been considered there in the next section. On the other hand they are also related to the non-stationarity of a shock ramp. We will therefore return to them also in the respective section on the time dependence of evolution of shock ramps and their stability. It is, however, worth mentioning that recently very large electric fields have been detected during

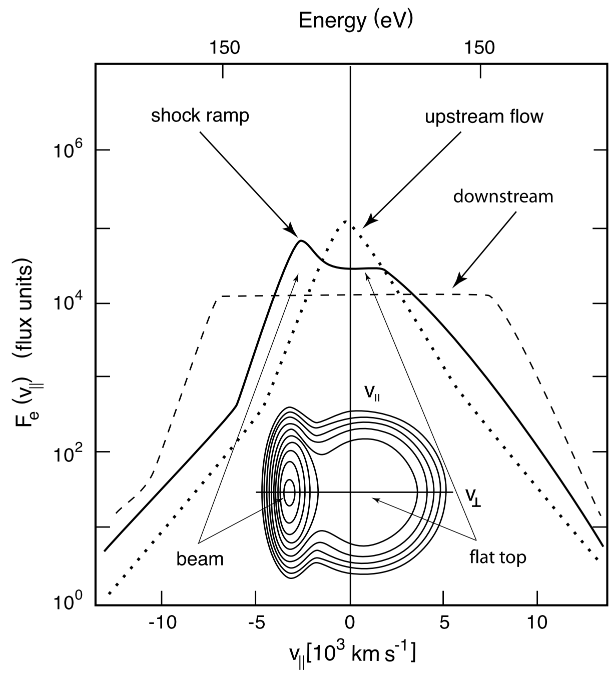

Figure 5.19: Several successive reduced parallel electron distribution functions $F_e(v_\parallel)$ during the crossing of the supercritical bow shock of the Earth by ISEE 2 on December 13, 1977. The cuts through the distribution show the transition from the Maxwellian-plus-halo upstream flow distribution through the shock ramp distribution to the close to the shock downstream distribution. The shock ramp distribution is intermediate in evolving into a flat-top distribution of the kind of the downstream distribution but contains in its upstream directed part a well expressed shock-reflected electron beam of velocity of a few 1000 km s^{-1} which is sufficiently fast to destabilise the shock front and excite electron plasma waves [after *Gurnett*, 1985, courtesy American Geophysical Union].

passages of the Polar satellite across the quasi-perpendicular bow shock when the spacecraft was traversing the shock ramp.

These observations showed that in the shock ramp electric fields on scales $\lesssim \lambda_e = c/\omega_{pe}$ exist with amplitudes of the order of several 100 mV m^{-1}. These are amongst the strongest localised electric fields measured in space [*Bale & Mozer*, 2007]. Clearly, these localised fields are related to the electron dynamics in the shock and in particular in the shock overshoot/ramp region. Excitation of intense electron waves in the shock ramp has been expected for long time already since the observation of the (reduced) electron distribution across the shock from a drifting to a flat-topped distribution [*Feldman et al*, 1983]. Figure 5.19, taken from *Gurnett* [1985], shows this transition. The interesting point is that right in the ramp/overshoot region the reduced electron distribution function shows the presence of an electron beam in addition to an already quite well developed flat top on the distribution. Such a beam will almost inevitably serve as the cause of instability.

5.3.3 The Quasi-perpendicular Shock Downstream Region

We have already mentioned earlier that a shock without a downstream region does not exist. Detached shocks that evolve in front of blunt obstacles like a magnetosphere, in particular, possess extended downstream regions which separate the obstacle from the undisturbed upstream region. These regions are the domains of compressional waves – of the family of magnetosonic waves – with upstream directed phase and group velocities larger than the downstream flow velocity that in a characteristic flow time across the downstream distance from the shock to the obstacle can make it upstream to reach the shock, which forms the spatial envelope of these waves thereby confining them to downstream of the shock transition.

This is the fluid picture of the evolution of the region downstream of the shock. In this subsection we are not going into an extended discussion of the downstream region of a quasi-perpendicular shock but restrict only to a few remarks. The reason is that for a curved collisionless supercritical shock it is very difficult to distinguish between the processes triggered by the quasi-perpendicular and quasi-parallel parts separately. In order to do this one needs to have plane shocks which are found possibly at the giant distant planets (cf. Chapter 10 on Planetary Bow Shocks) and at interplanetary travelling shocks. The latter, unfortunately, are mostly subcritical as they are convected by the stream and therefore their downstream regions differ from those of supercritical shocks. Because of this reason we delay a more substantial discussion of downstream regions to the next chapter after having presented the main properties of quasi-parallel shocks.

Collisionless shocks cannot be described solely in the fluid picture, however. Therefore the downstream region has quite a different behaviour from that inferred from the hydrodynamic description. This is particularly true for quasi-parallel shocks which (see the next chapter). Downstream of a quasi-perpendicular or perpendicular super-critical shock the conditions are as well very different from those which the fluid picture prescribes which of the plasma properties basically predicts an increase in the fluid pressure anisotropy due to compression of the magnetic field and plasma under conservation of the fluid magnetic moment (the ratio $T_\perp/B$), the deviation of the flow around the obstacle, draping of the magnetic field, and a pile-up region of the magnetic field close to the obstacle where pressure balance requires dilution of the plasma.

The main reasons for a deviation from this average and laminar behaviour of the downstream region are that in the supercritical case the fluid picture does not contain the ion (and electron) reflection processes and their consequences for shock foot formation, ramp physics and formation of the shock overshoot. Since collisional dissipation is out of question, the reflection mechanisms replace the necessary dissipation. It is easy to estimate, for instance for the quasi-perpendicular Earth's bow shock, how much energy must be dissipated in order to adjust for the differences in the flow properties between upstream and downstream. For an upstream solar wind of nominal density $N = 5\times 10^6\,\mathrm{m}^{-3}$ and velocity $V_1 = 500\,\mathrm{km/s}$ at 1 AU, Mach number $\mathscr{M} = 5$ and moderate shock strength (compression ratio) of $B_2/B_1 = 3$, the energy density in the flow behind the shock (Mach number $\mathscr{M} = 1$) is just half the energy density in the solar wind. Thus 50% of inflow energy must be dissipated by the shock. Since at most 10% of the ions are reflected(corresponding to 10% of incoming energy only), the remaining 40% are absorbed and dissipated in other ways.

A first simple effect that affects the region behind the shock ramp is that the reflected ions are accelerated by the motional electric field in the shock foot along the shock surface in the direction perpendicular to the upstream magnetic field to energies that are much higher than the kinetic energy of the incoming ions, thereby absorbing a substantial part of inflow energy. Acceleration of the 10% reflected ions by a factor 2 gives already 40% of energy dissipation. Hence this is the main dissipation mechanism.

We have already described how this acceleration affects the nearly periodic reformation of a quasi-perpendicular shock when these ions carry a drift current and gyrate at high speeds and large ion gyroradii in the upstream magnetic field. However, after a few such gyrations they have gained sufficient energy to break through the reflecting shock potential and overcome the shock barrier to enter the downstream flow region. Downstream of the quasi-perpendicular shock they appear as an energetic gyrating ion component with much larger perpendicular than parallel energy.

In fact these gyrating energetic ions have been observed [*Sckopke et al*, 1983]. They are a source of free energy and excite a number of instabilities like electromagnetic ion-cyclotron waves which can grow to large amplitudes downstream of the shock and contribute to the magnetic fluctuation that are observed downstream. Even mirror modes just behind the shock have been reported [*Czaykowska et al*, 1998]. The rms amplitudes $b_{\rm rms} = \sqrt{\langle|\mathbf{b}|^2\rangle} \sim B_2$ of these waves downstream of the shock are comparable to the average downstream field B_2. Therefore these waves contribute to the energy balance. Moreover, since they are convected downstream and damp away, they contribute to heating of the downstream plasma and shock energy dissipation.

The larger amplitude waves do not damp but decay into other shorter amplitude waves or by ponderomotive force interaction may stabilise and form large amplitude localised magnetic structures, density pulses or also narrow current sheets. The physics of these structures is still barely understood. Sometimes one speaks about downstream turbulence which, however, is not qualified and also unjustified as turbulence can hardly develop in the downstream region because it has not sufficient time for reaching a well mixed state. This would require a very large extended region and relatively quiet boundary conditions with continuous inflow at an approximately constant energy level. It would also require stationarity of the shock which is definitely not given, as we will see later when discussing the problem of stationarity. Shock reformation is already kind of a rather non-stationary process that makes the development of downstream turbulence rather doubtful.

The narrow current sheets which the presence of such wave structures implies have transverse scales comparable to the ion inertial length. They must close in themselves. They thus form current vortices on scales of several ion gyroradii. Even though they are very thin, their dynamics is different from the dynamics of narrow current sheets that undergo reconnection, drift kink modes and tearing instabilities like the current sheets in the tail of the Earth's magnetosphere. The reason is that these vortices are convected with the flow and there is very little velocity difference between them to trigger reconnection.

In addition, adjacent current sheet vortices have antiparallel currents and experience repulsing Lorentz forces such that they avoid close contact. However, if the currents become strong enough, i.e. if the amplitudes of the magnetic field fluctuations become large enough, they can decay due to generation of current instabilities which again are mostly in the drift modes and lower hybrid modes, accelerate electrons along the magnetic field and heat the plasma by dissipating their energy. Electron heating and the appearance of lower hybrid modes in connection to the observation of these current vortices thus rather indicates their decay than reconnection.

To these downstream excited waves a couple of other waves can be added. These are waves that are generated in the upstream shock foot having phase and group velocities less than the flow velocity and thus are swept down into the shock, where they accumulate and contribute to local dissipation in case their group velocities compensate for the reduced downstream flow across the shock. Otherwise they pass the shock and contribute to the downstream fluctuations.

Among those waves are the various low frequency electrostatic waves that are excited in the foot and will be described below. They propagate in the ion acoustic and lower hybrid mode frequency ranges and appear downstream as broadband low frequency noise where they have been observed for long time [*Rodriguez & Gurnett*, 1975]. The electrostatic modes in the lower-hybrid range have electric field components along the magnetic field and thus accelerate electrons into beams, a process that serves the transport of energy from the ion flow to the electron component and is responsible for electron heating, formation of electron beamlets and generation of the recently detected downstream solitary structures in the electron plasma wave component [*Pickett et al*, 2004].

In the next chapter on quasi-parallel shocks we compare the downstream wave spectra for both quasi-perpendicular and quasi-parallel shocks in Figure 6.50. However, even this short reconciliation of the fluctuating state of the downstream region behind a quasi-perpendicular shock shows that the downstream medium is in a rather complex plasma state investigation of which is interesting in itself though poorly understood yet.

5.4 Electron Dynamics

When talking about the dynamics of electrons hybrid simulations cannot be used anymore. Instead, one must return to the more involved full particle PIC simulation codes or to Vlasov codes, which directly solve the Vlasov equation in the same way as a fluid equation, this time, however, for the "phase space fluids" of ions and electrons. In both cases short time scales of the order of the electron gyro-period ω_{ce}^{-1} or even the electron plasma period ω_{pe}^{-1} must be resolved, and resolution of spatial scales of the order of the electron inertial scale λ_e and Debye scale λ_D is required. It is thus no surprise that reliable simulations of this kind became available only within the last decade with the improved computing capacities.

5.4.1 Shock Foot Electron Instabilities

Papadopoulos [1988] proposed that in the foot region of a perpendicular highly supercritical shock the velocity differences between reflected ions and electrons from the upstream plasma inflow should be responsible for the excitation of the Buneman two-stream instability thus heating the electrons, generating anomalous conductivity and causing dissipation of flow energy which contributes to shock formation.

Buneman Two-Stream Heating in Strictly Perpendicular Shocks

Shimada & Hoshino [2000] and *Schmitz et al* [2002] building on this idea performed full particle PIC simulations in strictly perpendicular shocks discovering that the Buneman two-stream instability can indeed work in the foot region of the shock and can heat and accelerate the electrons. *Shimada & Hoshino* [2000] initiated their one-dimensional simulations for a small mass ratio of $m_i/m_e = 20$, $\beta_i = \beta_e = 0.15$, and Alfvénic Mach numbers $3.4 \leq \mathscr{M}_A \leq 10.5$.

Figure 5.20 shows some of their simulation results. It is interesting to inspect the right part of the figure which shows the (shaded) ramp and foot regions on the left in expanded view. The electron phase space shows the development of electron holes which are generated by the Buneman two stream instability in this strictly perpendicular shock simulation. The signature of the electrostatic field E_y in the lowest panel shows the bipolar electric field structure the holes cause. The average field is zero, but in the hole it switches to large negative values, returns to large positive values and damps back to zero when passing along the direction normal to the hole. This is exactly the theoretical behaviour expected for both, solitons and electron holes of the form of BGK modes. As known from simulations (see Chapter 3) such BGK-hole structures will trap electrons and heat them, they do, on the other hand, also accelerate passing electrons to large velocities. Both is seen here also in the simulations in the vicinity of the shock: Three such holes are completely resolved in the right high resolution part of the figure, with decreasing amplitude when located closer to the shock ramp. All of them contain a small number of trapped electrons over a wide range of speeds which on the gross scale on the left fakes the high temperature of the electrons they achieve in the hole. This is just the effect of heating by the two-stream instability. In addition the electron velocity shows two accelerated populations, one with positive velocity about 2–3 times the initial electron speed, the other reflected component with velocity almost as large as the positive component but in the opposite direction suggesting that the electron current in the holes is almost compensated by the electron distribution itself.

Obviously the further strong heating of electrons in the ramp is caused by many smaller amplitude overlapping holes as is suggested by the structures in the inflowing and reflected ion distributions which do also strongly interact with the electric field of the holes. This is seen in the incoming ion component in the first hole as a dip in the velocity. The hole retards the incoming flow. It is also seen in the reflected ion component as strong distortion of their backward directed velocity when encountering a hole. The smaller speed ions are obviously retarded in their backward flow and are partially trapped in the negative electric

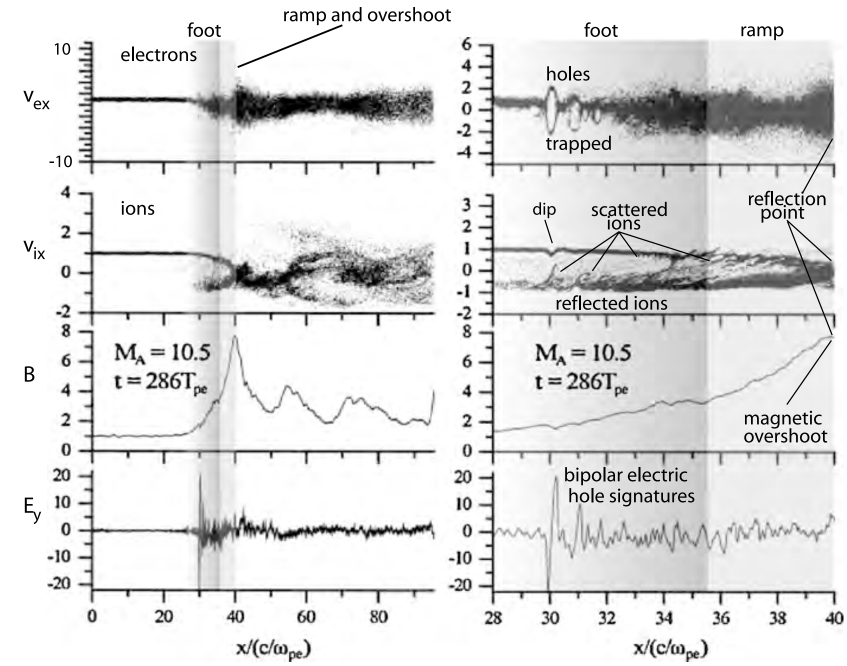

Figure 5.20: One-dimensional full particle PIC simulations with mass ratio 20 for Mach number $\mathscr{M}_A = 10.5$ and $\Theta_{Bn} = 90°$ resolving the electron scales [after *Shimada & Hoshino*, 2000]. *Left*: Simulation overview for electron and ion phase spaces, magnetic field and electric field. Ion reflection from the ramp and foot formation is seen in the *second panel from top*. The electrons are heated in the foot region. the heating coincides with large amplitudes in the electric field in the *lowest panel*. *Right*: Expanded view of the shaded foot and ramp regions on the *left*. The electron heating location turns out to be a site of electron hole formation. Three Buneman two-stream instability holes are nicely formed on this scale with trapped electrons. The broadening of the distribution and thus heating is due to the holes. Retardation of the ions in interaction with the holes is seen in the *second panel* which is due to the retarding electric potential in the large amplitude electric field oscillations (*lowest panel*). Interestingly enough, ion reflection takes place in the very overshoot! The ion distribution is highly structured in the entire region which is obviously due to interaction with many smaller scale electron holes.

field part of the hole. Very similar strong scattering of the incoming ion component is seen in the ramp region. This suggests that a large number of electric field structures are located in the ramp which scatter the incoming ions. These must be related to the highly fluctuating electric field component in the ramp seen on the right in the lowest panel.

Two further observations which are related to the ion component are of considerable interest: The first is that the retardation of the incoming ion flow and the scattering of the reflected ions in the foot region cause a signal on the magnetic field component. The second is that the reflection of the main incoming ion beam, i.e. the incoming plasma takes place at the location of the magnetic overshoot and not in the shock ramp. Therefore, physically spoken, the shock ramp is also part of the foot, while it is the narrow overshoot

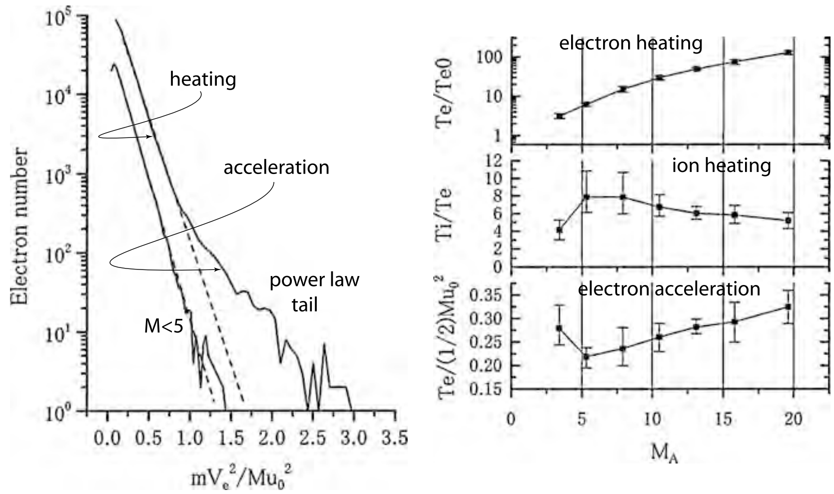

Figure 5.21: *Left*: The electron distribution in the shock arising from the action of the Buneman electron hole interaction at large Mach numbers $\mathscr{M}_A > 5$. The interaction not only causes heating but also an energetic tail on the electron distribution function. This tail has the shape of a power law $F\varepsilon \propto \varepsilon^{-\alpha}$, with power $\alpha \approx 1.7$. Note that this power gives a very flat distribution close to marginal flatness $\alpha = \frac{3}{2}$ below that an infinitely extended distribution function has no energy moment. *Right*: Evolution of the average electron temperature, ion temperature and ratio of electron temperature to initial kinetic energy in the simulations as function of Alfvénic Mach number [after *Shimada & Hoshino*, 2000]. All quantities are in relative units of computation.

region where the reflection occurs in a strictly perpendicular supercritical shock with cold ion inflow. The actual ramp region is much narrower than for instance shown in the figure. Its actual width is only of the order of $\Delta \sim (1\text{–}2)c/\omega_{pe}$.

Electron Heating and Acceleration

Shimada & Hoshino [2000] followed the evolution of the electron vortices (holes) and showed that a hole once evolved distorts the ion and electron velocities in such a way that nonlinearly the velocity difference can increase and cause the generation of secondary vortices, which leads to excessive electron heating [see also *Shimada & Hoshino*, 2005]. The result is the generation of an extended electron tail on the electron distribution. This is seen from the left part of Figure 5.21 in a log-lin representation of the electron number versus normalised electron energy. When plotting the data on a log-log scale (not shown) one realises that the newly produced tail of the electron distribution has a power law slope $F(\varepsilon) \propto \varepsilon^{-\alpha}$, notably with power $\alpha \approx 1.7$. (Note that this power is close to the marginally flattest power $\alpha = \frac{3}{2}$ below that an infinitely extended power law energy distribution has no energy moment more and thus ceases to be a distribution. In fact, any real nonrelativistic power law will not be infinitely extended but will be truncated due to the finite extent of the volume and loss of energetic particles.)

The dependence of electron heating and ion cooling on Mach number for the investigated range of Alfvénic Mach numbers is plotted on the right. The effect does not occur for small Mach numbers, too small for the Buneman two-stream instability to be excited. However, once excited, the heating increases strongly with $\mathscr{M}_A$. Over the range $5 < \mathscr{M}_A < 20$ the increase in electron temperature (electron energy stored mainly in the tail of the distribution) is a factor of 40–50, which demonstrates the strong non-collisional but anomalous transfer of kinetic flow energy into electron energy via the two-stream instability. However, one should keep in mind that this result holds merely for a one-dimensional simulation of strictly perpendicular shocks.

At this place we should look again at observations during crossings of real collisionless shocks in space. Recently, during passages of the Polar satellite of the quasi-perpendicular Bow Shock of the Earth, very strong localised electric fields have been detected. These fields exist on scales $\lesssim \lambda_e = c/\omega_{pe}$, less than the electron skin-depth, and reach enormous values of $\lesssim 100\,\mathrm{mV\,m^{-1}}$ parallel and $\lesssim 600\,\mathrm{mV\,m^{-1}}$ perpendicular to the magnetic field. They must naturally be related to the electron dynamics and should play a substantial role in the formation and dissipation processes of the quasi-perpendicular shock. They should also be of utmost importance in accelerating electrons (and possibly also ions) at shocks. Their nature still remains unclear, however, it is reasonable to assume that they are generated by some electron-current instability via either the Buneman-two-stream instability, the modified two-stream instability which we discuss below, or the ion-acoustic instability, depending on the current strength. In any case they will turn out to belong to the family of Bernstein-Green-Kruskal modes which are encountered frequently in collisionless plasmas.

5.4.2 Modified-Two Stream Instability

The Buneman two-stream instability works on scales $\leq \lambda_e = c/\omega_{pe}$. This condition is less easily satisfied in quasi-perpendicular shocks. However, here other instabilities can evolve which are relatives of the Buneman two-stream instability.

The condition that there is no current flowing in the shock normal direction during foot formation and reflection of ions at the shock requires that the electron inflow from upstream is decelerated when entering the foot region. This causes a difference in the ion and electron inflow velocities. In a quasi-perpendicular shock the wave vector $\mathbf{k} = (k_\|, \mathbf{k}_\perp)$ is allowed to have a component $k_\|$ along the magnetic field. The velocity difference between ions and electrons can then excite the modified two-stream (MTS) instability, a modification of the Buneman instability acting in the direction perpendicular to the magnetic field. This instability is electromagnetic coupling the Buneman two-stream instability to the whistler mode. The waves generated propagate on the whistler mode branch with frequency $\omega_{\mathrm{mtsi}} \sim \omega_{lh} \ll \omega_{ce}, \omega_{pe}$, close to the lower-hybrid frequency, but far below both the electron cyclotron and electron plasma frequencies, respectively. These waves are capable to modify the shock profile when being swept downstream towards the shock ramp. Their obliqueness generates a magnetic field aligned wave electric field component which accelerates, traps and eventually pre-heats the electrons in the shock foot along the magnetic field.

Relation to the Buneman Instability

Scholer & Matsukiyo [2004] investigated the transition from Buneman to modified two-stream (MTS) instabilities as function of mass ratio m_i/m_e and for various β_i, β_e in the regime where no upstream standing whistlers exist, i.e. above the critical whistler Mach number $\mathscr{M}_A > \mathscr{M}_{\rm wh}$. This investigation is restricted to shocks, however, with **k**-vectors being strictly perpendicular to the shock along the shock normal and for one-dimension only. This excludes any waves which could propagate along the inclined magnetic field. Nevertheless, this investigation is interesting in several respects. First it showed that for mass ratios $m_i/m_e \lesssim 400$ no modified two-stream instabilities occur since their growth rates are small. The electron dynamics and the shock behaviour in this range are determined by the Buneman two-stream instability unless the electron temperature is large enough to inhibit its growth in which case ion-acoustic instability should (or could) set on (but has not been observed or has not been searched for). For larger mass ratios (and particularly for the realistic mass ratio) the Buneman two stream instability ceases to be excited. Instead, the modified two-stream instability (MTSI) takes over which is strong enough to completely determine the behaviour of the electrons. A summary of their results is schematically given in Figure 5.22.

The evolution of the MTS-waves for realistic mass ratio simulations is shown in Figure 5.23 for three instants of time. The wave spectrum has been determined in the shaded area. Large amplitude waves of left-hand polarisation propagate toward the shock during this reformation cycle. These waves are related to the electron dynamics. They are excited by the modified two-stream instability in the foot (top panel) in interaction between the retarded electrons and the fast ions. The simulations also show the evolution of large amplitude electron holes and ion holes (right lower panel). Such structures have been observed in the electric field in the quasi-perpendicular shock region [*Bale et al*, 2002; *Pickett et al*, 2004; *Balikhin et al*, 2005; *Hull et al*, 2006; *Hobara et al*, 2008] with differing interpretations. From the simulations it is concluded that both kinds of holes/solitary structures are excited near a quasi-perpendicular shock on similar scales while being related to the combined electron and ion dynamics.

Modified Two-Stream Instability and Quasi-perpendicular Shock Reformation

They cause reformation of the shock, but in a different way than it is caused for low mass ratio by the Buneman-instability. There the reformation was the result of accumulation of ions at the upstream edge of the foot, while here it is caused by participation of the foot ions in the MTSI all over the foot and particularly close to the shock ramp and presumably also at the ramp itself. Phase mixing of the ions leads to bulk thermalisation and formation of a hot retarded ion component in the foot region which has similar properties like the downstream population and, when sufficiently compressed takes over the role of the shock ramp. This can be seen from the lower right part of Figure 5.23 which is a snapshot at time $t\omega_{ci} = 3.7$ showing the magnetic profile, the density profile with its strong distortions, and the evolution of the ion distribution which evolves into large thermalised vortices towards

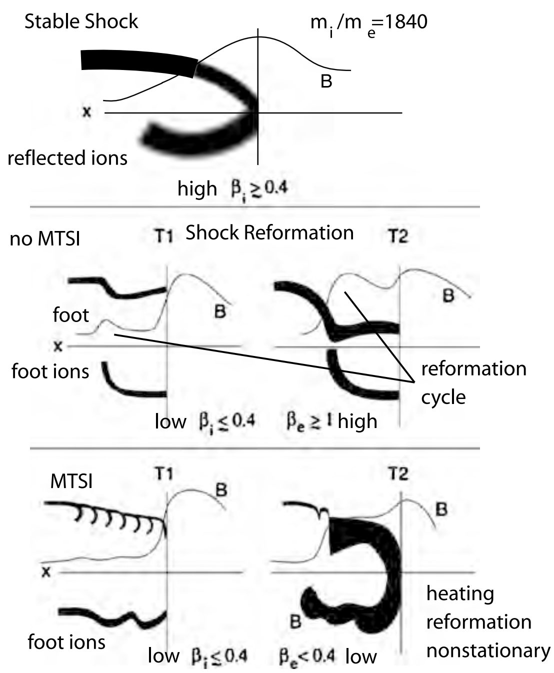

Figure 5.22: Schematic of the dependence of the shock structure on the combinations of β_i, β_e for quasi-perpendicular supercritical but non-whistler shocks. For large β_i the shock is stable even though ions are reflected. At small β_i, large β_e the shock reforms due to accumulation of ions at the edge of the foot forming n reformation cycle. For small β the MTSI evolves in the foot, strong heating and complicated dynamics evolves due to nonlinear interaction, heating and hole-vortex formation [after *Scholer & Matsukiyo*, 2004].

the front of the shock (note that here the shading indicates also the spatial domain where the wave spectra have been taken).

The generation of MTS-waves by the modified two-stream instability has been investigated in depth theoretically and with the help of specially tailored one-dimensional numerical simulation studies by *Matsukiyo & Scholer* [2003], and in two-dimensional simulations by *Matsukiyo & Scholer* [2006a, b] which we are going to discuss in detail.

Modified Two-Stream Generation Mechanism: Tailored Simulations. Figure 5.24 in its left-hand parts shows the set-up of the two-dimensional simulation and the resulting time histories of fields and particles. The incoming and reflected ion velocities are shown for time zero in the (x,y)-plane where the co-ordinate y is about parallel to the magnetic field. The phase space at time zero contains the three distributions of inflow and reflected ions and hot incoming electrons. The slight displacement between the latter and the incoming ions accounts for zero normal current flow in presence of reflected ions. Clearly this configuration is unstable causing instabilities between the ion beams and electrons (in

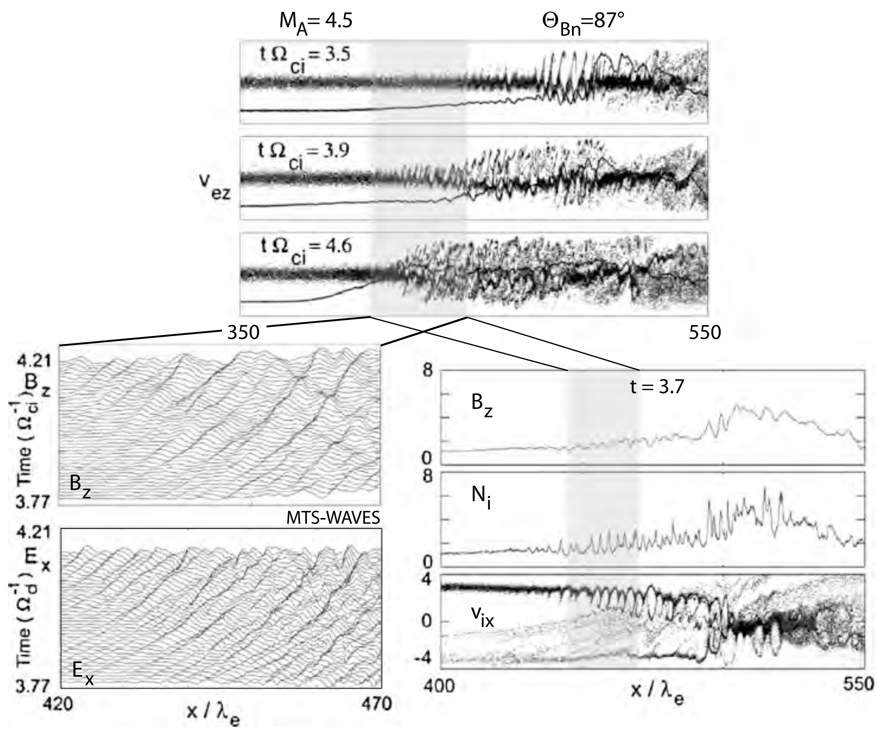

Figure 5.23: *Top*: Electron phase space evolution showing the distortion of the electrons until thermalisation during the modified two-stream instability. The evolution of narrow electron holes can be seen of increasing amplitude (phase space width) the closer one comes to the shock ramp. *Lower left*: Magnetic and electric wave components of MTSI waves present in the *grey shaded area* in space during part of the time shown and are moving toward the shock ramp in the left-hand mode as discussed earlier. These waves steepen when reaching the shock front. Distortion of the ion distribution is the result as shown in *Lower right*. Large amplitude ion holes are formed as well [after *Scholer & Matsukiyo*, 2004].

addition to the slowly growing ion-ion instabilities discussed earlier). The basic physics of the instability can be readily identified from the time histories of the fields and particles in the middle of Figure 5.25. The first exponential growth phase of the E_x-component for times $\omega_{pe}t < 500$ is due to the Electron-Cyclotron-Drift instability (ECDI) which we have omitted in our theoretical analysis in Chapter 3 [cf., also, *Muschietti & Lembège*, 2006]. This instability is driven by the ion beam when it interacts with obliquely propagating electron-Bernstein waves (electron-cyclotron waves). In fact, this instability, in the present case is nothing else but the Buneman instability (BI) which for the given set-up is initially unstable (as is seen from the bulk velocity difference between the ion and electron phase space distributions on the left of the figure) due to the interaction of the ion beam mode with the lowest order electron-cyclotron mode. Initially there is some growth also in the

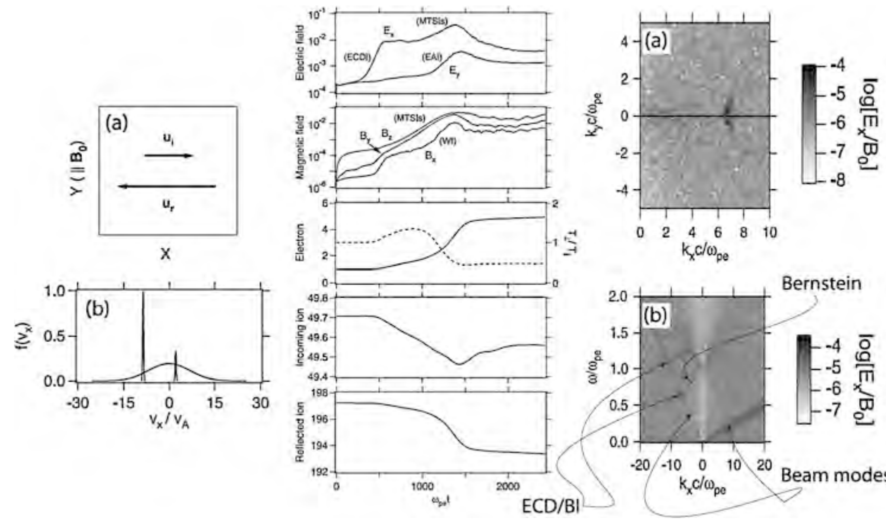

Figure 5.24: *Left*: The phase space distribution set-up for the simulation. The original magnetic field is in z-direction. The *upper panel* shows the incoming and reflected ion beams. The *lower panel* shows the two cold ion distributions, incoming and reflected, and the hot electron distribution, shifted slightly in order to satisfy the zero-current condition in shock-normal direction. *Centre*: Time histories of the energy densities of the simulation quantities: electric and magnetic wave fields, electrons and the two ion components. *Right*: Wave power spectra in **k**-space at early times $t\omega_{pe} < 404.8$ showing the excited power in the Buneman mode in the *upper panel*. The *lower panel* shows the dispersion relation. The *two straight lines* correspond to the damped beam modes of the reflected (negative slope) and direct (positive slope) ion beams. The enhanced power in the *two dark spots* is due to the ECD-instability, which is the Buneman mode which excited under these early conditions in the simulation as the interaction between the reflected ion beam mode and the first and second Bernstein harmonic waves [after *Matsukiyo & Scholer*, 2006a, courtesy American Geophysical Union].

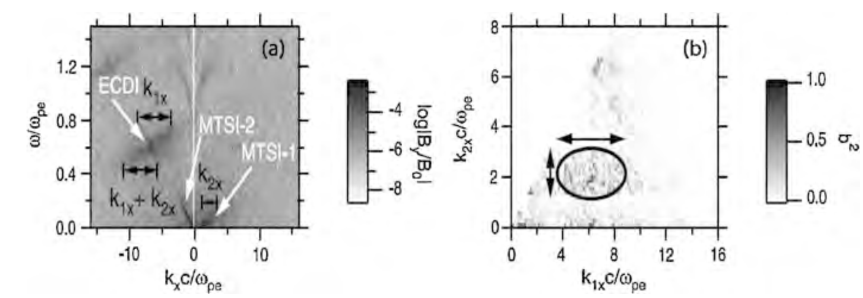

Figure 5.25: *Top*: The dispersion relation for the time interval $607.2 < t\omega_{pe} < 1011.9$ showing the ECDI (Buneman mode), the original MTI-1 and the secondary MTSI-2 which is generated by wave-wave interaction. The corresponding reaction in k_x numbers is indicated for the waves which participate in the three-wave process. *Bottom*: The power spectral density in the (k_x, k_y)-plane. The ellipse indicates the wave numbers that contribute to the wave-wave interaction of the MTSI-1 and ECDI [after *Matsukiyo & Scholer*, 2006a, courtesy American Geophysical Union].

magnetic field which is strongest in B_z and much weaker in B_y and B_x. However, until the MTSI sets on the magnetic field energy does not grow substantially. This changes with onset of the MTSI when all components increase with B_y, B_z dominating and being of equal intensity, showing that due to the magnetic wave field of the MTSI the instantaneous magnetic field develops a transverse component.

The MTSI does not grow in this initial state because its growth rate is small for these conditions. During the saturation phase the ECDI still dominates in the flat regime until the MTSI takes over causing further growth of the already large amplitude electric field fluctuations. This stage after $\omega_{pe}t > 10^3$ is characterised by a growth phase also in E_y (which is due to the electron acoustic instability EAI which can be excited in presence of both a cold and a hot electron component) and, surprisingly, the normal component B_x.

This latter component might be caused by the Weibel instability (WI) when a substantial anisotropy is generated. Such an anisotropy exists for the ions, in fact, in our case as they propagate solely in $\pm x$-direction at grossly different speeds. The growth rate of the instability, neglecting the magnetic field, i.e. setting $\omega_{ce} = 0$, is $\gamma_{\rm WI} = (V_i/\lambda_i)(1 + 1/k^2\lambda_e^2)^{-\frac{1}{2}}$ [*Weibel*, 1959], where $\lambda_{e,i} = c/\omega_{pe,i}$ are the ion and electron inertial lengths, respectively. When the magnetic field is not neglected but the ions are taken as non-magnetised, as is the case in the shock foot, then

$$\gamma_{\rm WI} = \frac{V_i}{\lambda_i}\left(1+\frac{1}{k^2\lambda_i^2}\right)^{-\frac{1}{2}} \quad \text{for} \quad \left(1+\frac{1}{k^2\lambda_i^2}\right)\frac{\omega_{ce}^2}{\omega_{pi}^2} \gg \frac{V_i^2}{c^2}\left(1+\frac{1}{k^2\lambda_e^2}\right) \tag{5.22}$$

At short wavelengths the growth rate of this instability can be quite large. Its maximum is assumed for $k^2 \to \infty$ when it becomes the order of $(\gamma_{\rm WI}/\omega_{ci})_{\rm max} \sim V_i/V_A \simeq \mathscr{M}_A$. At the expected wave-number $k\lambda_i \sim 1$ is just a factor $\sqrt{2}$ smaller than its maximum value and decreases rapidly towards longer wavelengths.

One may thus expect that large Mach number shocks generate magnetic fields by the Weibel instability, in which case the field becomes non-coplanar, and small-scale stationary magnetic structures appear in the shock foot and ramp. Still, this is a little speculative. However, if the Weibel instability exists it will generate many small-scale magnetic structures in the shock. This is, in itself, sufficiently interesting to be noted. The simulations show the presence of $B_x \neq 0$, suggesting that the magnetic field becomes three-dimensional since the Weibel instability has zero frequency and thus produces a steady normal field component. At very high Mach numbers the Weibel instability will help reflecting a much larger fraction of ions thereby contributing to sustaining the shock and increasing the (viscous) dissipation rate. This is of substantial interest in astrophysical applications.

The right outermost part of the figure shows two power spectra of the electric field in (k_x, k_y)-space at times $t\omega_{pe} = 253$ (top) and $t\omega_{pe} < 404.8$ (bottom). In the top panel the power of the waves concentrates at $(k_x\lambda_e, k_y\lambda_e) = (6.8, 0)$. These waves propagate nearly perpendicular to the ambient magnetic field.

The lower panel shows the dispersion relation $\omega(k_x)$ for these waves in a grey scale representation. The two straight dark lines with negative and positive slopes belong to the damped ion beam modes for the reflected (negative slope) and incoming (positive slope) ion beams.

There are two dark specks on the reflected beam mode where the intensity of the electric field (which is shown here only) is enhanced. These specks are separated by about the electron cyclotron frequency in frequency. They belong to the crossings of the reflected ion beam mode and the two lowest harmonics of the electron Bernstein modes which is the ECD-instability which in this case is also the Buneman instability (BI). This mode has been investigated by *Muschietti & Lembège* [2006] in one-dimensional PIC simulations and has been shown to be present in the foot region. Since we now know that it is the Buneman mode, it is no surprise to find it in the early stage here in two dimensions, when the conditions are favourable for the Buneman mode and the initial situation is still close to one-dimensional. It is, however, important to note that the Buneman two-stream instability is excited by the large difference in bulk speeds between electrons and reflected ions. In the later stages, as the existence of the electromagnetic left-hand polarised negative helicity waves in Figure 5.23 confirms, the ECDI/Buneman mode is replaced by the MTS-instability which generates oblique, nearly perpendicularly propagating large amplitude electromagnetic waves which also form hole structures and heat the plasma.

Figure 5.25 shows the next time slot in the presentation of the dispersion relation (left). At this time the waves have reached large amplitudes, large enough to cause various interactions among the waves which react on the wave and particle distributions and, in addition, cause nonlinearity of the plasma state at wave saturation. The ECDI forms as a broad spot in the (ω, k)-domain. The MTSI is the short nearly straight line at low frequencies and small positive k_x (indicated as MTSI-1 in the figure). In the wave spectrogram these waves move towards the shock ramp. This means their slope is positive in the dispersiogram!

Secondary Modified Two-Stream Instability: Wave-Wave Interaction. In addition to these modes another negatively moving low frequency wave appears. This is also an MTSI, but it is a secondary one, which *Matsukiyo & Scholer* [2006a] have shown to arises in a three wave process when the ECDI-BI and the MTSI-1 interact causing a wave with $k_x = k_{\mathrm{BI}} + k_{\mathrm{MTSI-1}} = k_{\mathrm{MTSI-2}}$. The right part of the figure shows the enhanced wave power for this process extracted from the data on the way of a bi-spectral analysis and represented in the k-plane. The ellipse encircles the wavenumbers which are involved into the three-wave interaction, the original ECD-wave, and the resulting MTS-2-wave. Clearly, a whole range of waves participates in the interaction because the ECD-spectrum has broadened when saturating, and many combinations of ECD and MTS-1 waves satisfy the nonlinear three-wave interaction condition.

The top-left panel of Figure 5.26 shows the evolution of the electron velocity v_y during this interval and averaged over a range of x-values along the normal. This velocity is about perpendicular to the magnetic field; its dynamic range of variation is impressive. The panel at the lower left shows the electron phase space distribution. Two electron beams are seen to propagate at counter streaming velocities. These beams can already be identified in the upper panel. Due to the interaction with the unstable waves the region between the beams is partially filled. These distributions have been taken in the interval $17.6 < y/\lambda_e < 19$ as indicated in the top panel.

Another distribution a little further in the interval $39.1 < y/\lambda_e < 40,5$, at the rear end of the top panel, is shown in the lower right panel. Here the distribution has evolved

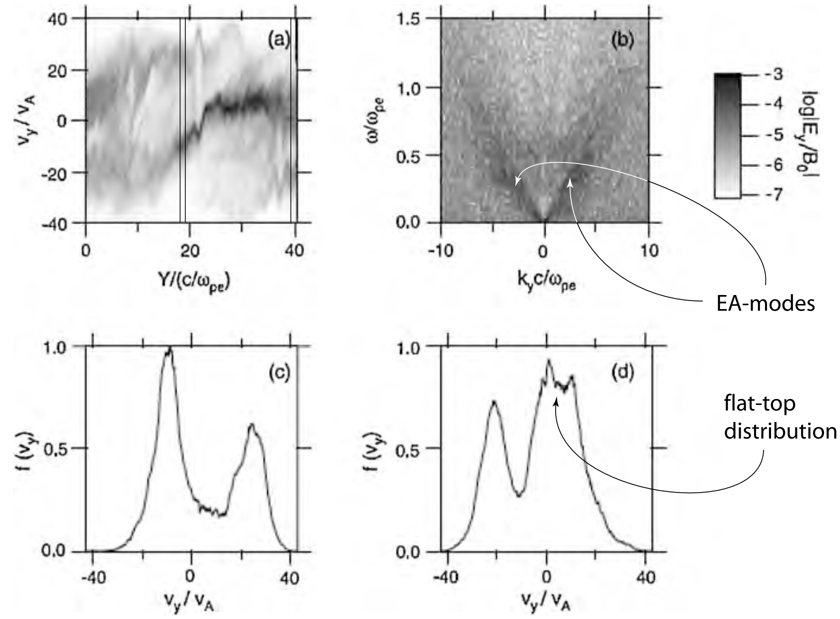

Figure 5.26: *Top*: Electron phase space plot (*left*) at $19.4 < x/\lambda_e < 21$, and (*right*) dispersion relation $\omega(k_y)$ for the period $910.7 < t\omega_{pe} < 1315.5$ as obtained from E_y. This dispersion relation shows the occurrence of EA-waves with strictly linear dispersion and frequency below $\omega_{ea} \lesssim \omega_{pe}$ while propagating in both directions. These are generated in the presence of the two-electron component structure seen in the distribution function below. They are responsible for the subtle fine-structuring of the electron distribution in the phase space as is seen in the *upper left panel* representation of v_y versus y which exhibits trapping and scattering of electrons on very small scales. *Bottom*: Two electron distribution functions at $17.6 < y/\lambda_e < 19$ and $39.1 < y/\lambda_e < 40.5$ at $t = 1000$, as indicated in the *upper left panel* by the *vertical lines*, showing the large electron hole distribution that is generated by the MTSI and some smaller substructures [after *Matsukiyo & Scholer*, 2006a, courtesy American Geophysical Union].

into a totally different combination of two electron populations, one top-flat and hot, the other one narrow, i.e. cold, but of same height indicating the retardation of one beam and heating of the other. Altogether the electron plasma has been heated to high temperature. Returning to the upper left panel the complicated structure of the distribution is nicely seen with several sub-beams evolving and also with electron trapping in some vortices being visible for instance in the upper part around $y \simeq 22\,\lambda_e$.

Coming now to the upper right panel, which shows the dispersion relation in the y-direction, one recognises two low-frequency linear wave modes propagating in positive and negative y-directions. These waves are electron-acoustic (EA) modes which are excited in the presence of the two electron distributions, the hot top-flat distribution and the cold beam distribution. They have strictly linear dispersion and frequencies below the electron plasma frequency $\omega_{ea} \lesssim \omega_{pe}$. Because they interact strongly with the electron distribution, they are responsible for the fine-structuring in the electron distribution function

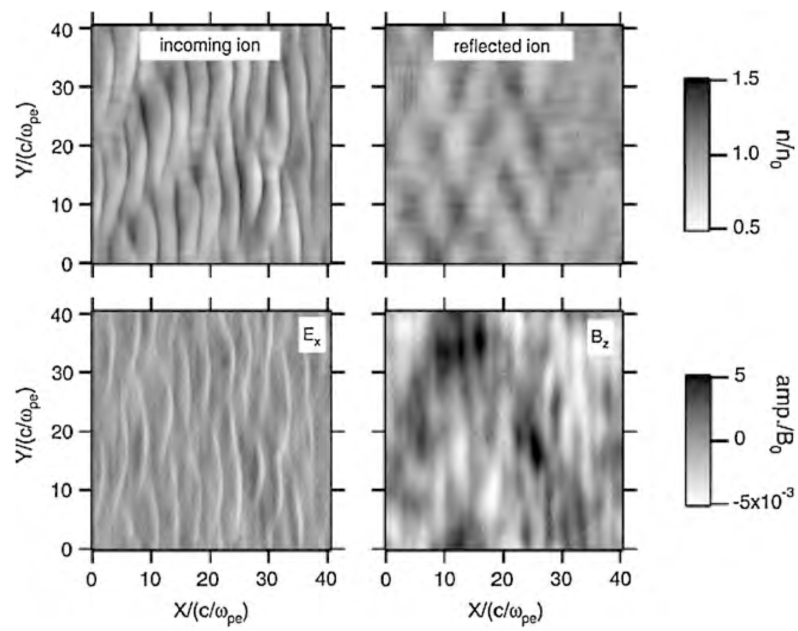

Figure 5.27: *Top*: Incoming (*left*) and reflected (*right*) ion densities at the late time $t\omega_{pe} = 2023.9$ shown in the (x,y)-plane. This time, in terms of the ion cyclotron period, corresponds to $t\omega_{ci} = 0.55$, i.e. about half an ion-cyclotron period. At later times the ion magnetisation would come into play as well. *Bottom*: The corresponding electric field E_x and magnetic fieldB_z profiles. One observes that the ECD-waves (Bernstein modes) have decayed by feeding their energy into electron heating. The two MTS-modes are still visible as the wavy variations in the incoming and reflected ion beams. The original MTS-1 wave modulates the incoming beam, which is seen in its downward propagation towards the shock. The secondary MTS-2 mode modulates, in addition, the reflected ion beam causing the interference pattern seen in the reflected beam density. The electric field is modulated by the MTS-2 wave, while the magnetic field contains signatures of both, MTS-1 and MTS-2 [after *Matsukiyo & Scholer*, 2006a, courtesy American Geophysical Union].

seen in the top-left panel of Figure 5.26 where they cause electron trapping and scattering which results in electron heating and electron acceleration.

We close this section by presenting ion densities of the reflected and incoming beams and the corresponding modulations of the electric E_x and magnetic variation fields B_z, respectively, in Figure 5.27 in two-dimensional grey-scale representation in the (x,y)-plane. One observes that the ECD-waves (Bernstein and Buneman-modes) have decayed. They have been feeding their energy into electron heating, creating electron holes, trapping electrons and shaking them, as we have discussed above. The two MTS-modes are still visible. They dominate the ion density structure being visible as the wavy variations in the incoming and reflected ion beams. The original MTS-1 wave only modulates the incoming beam. This is recognised from its long-wavelength downward propagation towards the shock. The secondary shorter scale MTS-2 mode modulates, in addition, the reflected ion beam causing the interference pattern seen in the reflected ion-beam density. The electric field is merely modulated by the short wavelength MTS-2 wave.

Weibel Instability Caused Effects. On the other hand, the magnetic field contains signatures of both, MTS-1 and MTS-2 thus exhibiting a more irregular structure than the electric field. Here, probably, also the small-scale structures of the Weibel instability do contribute. We have noted its effect already above, but it would be rather difficult to extract them from the figure as they should appear as stationary vortices, which are convected downstream towards the shock front with the speed of the average bulk flow. Their dynamics remains to be unresolved, i.e. it is not clear what will happen to them when encountering the shock front. One possibility would be that they accumulate there and generate a non-coplanar magnetic component. Nevertheless, the possibility for the Weibel instability to evolve in supercritical quasi-perpendicular shocks is of interest as Weibel vortices could, if confirmed by observations, cause an irregular fine structuring of the magnetic field in the shock ramp transition, which would have consequences for the particle dynamics, trapping, scattering, reflecting and acceleration of particles from the shock front. It could, moreover, also lead to small scale reconnection in the shock front, which so far has not been believed to exist in the shock, including the various side-effects of reconnection. Weibel vortices could also pass into the downstream region where they might contribute to the downstream magnetic turbulence. There they would occur as magnetic nulls or holes for which the shock would be the source.

5.5 The Problem of Stationarity

In this last section of the present chapter we will be dealing with the time-dependence of quasi-perpendicular shocks. Since in the previous sections we have frequently dealt with time variations, there is little new about time-dependencies of shocks. Nevertheless, in the past few years there has been much ado about the so-called "problem" of shock non-stationarity which has grown into an own field of shock research. We have already spoken on this before.

What does it mean that shocks can be or even are non-stationary? In principle, stationarity means time independence and, hence, is a question of the time scale under consideration. For instance, any cascade looked at from far is stationary. Such are shocks. As for an example take Earth's bow shock which stands in front of Earth for eons, or astrophysical shocks which for the human eye are practically invariable. On the time scale of their existence they are stationary, while on much shorter time scales they undergo global and local variations. Non-stationarity, at its best, thus just means nothing else but dealing with such variations. However, at a physically much deeper level would be the question for the *equilibrium state* of shocks. Clearly, as already explicated, *shocks are not in thermodynamic equilibrium*. They need to be driven. Thus the time scale of the global "stationarity" of shocks is the life time of the driver.

One kind of non-stationarity is shock reformation. This is a periodic or better quasi-periodic process in which the shock ramp for the time of foot formation remains about stationary, i.e. the shock ramp is well defined and moves ahead only very slowly. In fact, during the following reformation the shock is everything else but stationary: from one reformation cycle to the next the ramp flaps, it flattens and broadens while the new shock foot grows and steepens. And towards the end of the reformation cycle the shock ramp suddenly jumps ahead from its old position to the edge position of the shock foot. Could one follow this evolution over very many reformation cycles, one would find that there is no real periodicity but that the process of reformation, i.e. the time sequence of final forward jumps of the shock ramp would form a quasi-periodic or even chaotic time series. Unfortunately, computer capacities do not yet allow to simulate more than a few reformation cycles such that this conjecture cannot be proved yet. But it is simple logic that reformation cannot be strictly cyclic; there are too many processes involved into it, too many instabilities cooperate, and the particle dynamics is too complicated for a strictly periodic process to be maintained over longer times than one or two ion-gyroperiods. In addition, once the shock is considered two-dimensional – or even three-dimensional – the additional degrees of freedom introduced by the higher dimensions multiply and the probability for the shock of becoming a stationary or even cyclic entity decreases rapidly. This is particularly true for high-Mach number shocks even under non-relativistic conditions. Hence, we may expect that a realistic high-Mach number, i.e. supercritical shock will necessarily be locally non-stationary.

Principally, stationarity is a question of scales. On the macroscopic scale, the scale of the macroscopic obstacle and the macroscopic flow, a shock will be stationary as long as the flow and the obstacle are stationary. For instance, such stationary shocks are the planetary bow shocks that stand in front of the planetary magnetospheres or ionospheres. On the scales of the magnetospheric diameters their variation is of the same order as the variation of the solar wind or – if the magnetospheres themselves behave dynamically – the time and spatial scales of their variations are of the same order as the time and spatial scales of the magnetospheric variations, for instance the diurnal precession of the Earth's magnetic axis which causes a strictly periodic flapping of the magnetosphere and thus a strictly periodic variation of the position and shape of the Earth's bow shock.

On spatial scales of the order of the ion gyroradius and temporal scales of the order of the ion gyroperiod there is little reason to believe in stationarity of a collisionless supercritical shock wave. The whole problem of stationarity reduces to the investigation of instabilities and their different spatial and temporal scales and ranges, their evolution, saturation, being the sources of wave-wave interactions and nonlinear wave-particle interactions and so on. These we have already discussed in the former sections as far as the current state of the investigations do allow. What, thus, remains is to ask how a shock surface can become modulated in higher dimensions and what reasons can be given for such modulations.

5.5.1 Theoretical Reasons for Shocks Being "Non-stationary"

That collisionless shock waves might exhibit non-stationary behaviour was suggested early on from the first laboratory experiments on collisionless shocks [*Auer et al*, 1962; *Paul et al*, 1967]. *Morse et al* [1972] were the first to definitively conclude from their one-dimensional shock full particle PIC simulations that collisionless shocks seem to be non-stationary on the scale of the ion gyroperiod. Afterwards, time variations in the behaviour and evolution of collisionless shocks have been recovered permanently in shock simulations [e.g., *Lembège & Dawson*, 1987a, b].

This is no surprise as we have mentioned several times already. The *principal reason* is that shocks, and in particular supercritical shocks which are not balanced by collisional dissipation, are in thermal non-equilibrium and are thermodynamically not in balance. Hence, locally they are longing for any opportunity to escape this physically unpleasant situation in order to achieve balance and thermal equilibration. However, as simple as this reason might look, as difficult is it to find out what under certain given conditions will actually happen and which way a shock will locally direct itself for a try to escape non-equilibrium and to achieve equilibrium. Even though when it is permanently driven by an unchangeable flow and a stationary obstacle it will chose any kind of irregularity, fluctuation or detuning to drive some kind of instability, cause dissipation and, when driving will become too hard in any sense, it will overturn and break; and in this way it will maximise dissipation if it is not possible to achieve it in any smoother way.

Non-stationary behaviour of quasi-perpendicular shocks has been anticipated theoretically, following *Sagdeev* [1966], by *Kennel et al* [1985] who noted the existence of the critical whistler Mach number $\mathscr{M}_{\rm wh}$, which we have discussed above in comparison to numerical simulations. *Galeev et al* [1988] tried to give a theoretical account for reasons of the anticipated non-stationary character of supercritical shocks. They investigated the role of whistlers in the nonlinear domain at the ramp, finding that whistlers for flow speeds sufficiently above the Alfvén speed do not possess soliton solutions and thus do not sustain the steady state of a shock. This means very simply that neither dissipation nor dispersion can sustain the nonlinear steeping of the waves, and therefore the waves should cause breaking of the flow and lead to non-stationary behaviour of the ramp and crest, a process called by them ‘gradient catastrophe’. These authors also dealt with quasi-electrostatic waves of frequencies close to the lower-hybrid frequency ω_{lh} to which they attributed responsibility for wave breaking.

Simulations by *Quest* [1986], *Lembège & Savoini* [1992], *Savoini & Lembège* [1994] and *Hada et al* [2003] for low mass-ratios have attempted to illuminate some aspects of this non-stationary behaviour. *Lowe & Burgess* [2003] and *Burgess* [2006a, b] have investigated two-dimensional rippling of the shock surface in hybrid simulations and its consequences. Full particle simulations up to realistic mass ratios have been performed by *Scholer & Matsukiyo* [2004], *Matsukiyo & Scholer* [2006a, b] and *Scholer & Burgess* [2007]. We will return to these attempts. Here we first follow the analytical and simulational attempts of *Krasnoselskikh et al* [2002] to advertise the general non-stationarity of quasi-perpendicular shocks. We should, however, note that there is no principle reason for a shock to behave like we wish, i.e. to behave stationary. It might, if necessary, break and overturn or mike not; the only requirement being that it follows the laws of physics.

Nonlinear Whistler Mediated Non-stationarity

Krasnoselskikh et al [2002] rely on a method developed by *Whitham* [1974] to describe the nonlinear breaking of simple waves by adding to the simple wave evolution equation a nonlocal term that takes care of accumulating short wavelength waves. The Whitham equation reads

$$\frac{\partial v}{\partial t} + v\nabla_x v + \int_{-\infty}^{\infty} \mathrm{d}\xi\, K(x-\xi)\nabla_\xi v(t,\xi) = 0, \qquad K(x) = \frac{1}{2\pi}\int_{-\infty}^{\infty} \mathrm{d}k \frac{\omega(k)}{k} \mathrm{e}^{ikx} \quad (5.23)$$

If this additional term is purely dispersive, it reproduces the Korteweg-de Vries equation, if it is dissipative it reproduces Burgers' equation. In general, stationary solutions $\partial v/\partial t \to 0$ peak for $K(x) \sim |x|^{-\alpha}$ for $x \to 0$, and $\alpha > 0$. *Krasnoselskikh et al* [2002] use the whistler dispersion relation

$$\frac{\omega}{kV_A} = \left(\frac{m_i}{m_e}\right)^{\frac{1}{2}} \frac{|\cos\theta|k\lambda_e}{1+k^2\lambda_e^2}, \qquad \text{for} \quad k\lambda_i \gg 1,\ \cos^2\theta \gg \frac{m_e}{m_i} \quad (5.24)$$

describing low frequency whistlers at oblique propagation which, when inserted into the above integral for $K(x)$ asymptotically for $|x| \to 0$ yields $K(x) \sim \pi^{-1}\sqrt{m_i/m_e}|\cos\theta|[\mathsf{C} + \ln|x| + \ldots]$. Here $\mathsf{C} = 0.577\ldots$ is Euler's constant. Since $|x|^\alpha \ln|x| \to 0$ for all positive $\alpha > 0$ and $|x| \to 0$, nonlinear low-frequency whistler waves will necessarily break by the above condition. Thus, when whistlers are involved into shock steeping, and when $\alpha > 0$, they will necessarily break as their dispersion does not balance the nonlinear steeping. This happens when the Mach number exceeds the nonlinear whistler Mach number $\mathscr{M} > M_{\mathrm{wh,nl}}$. Both, whistler dispersion and dissipation by reflected ions cannot stop the whistlers from growing and steeping anymore, then.

In order to prevent breaking, another mechanism of dissipation is required. Still based on the whistler assumption, *Krasnoselskikh et al* [2002] argue that the shock ramp would radiate small wavelength whistler trains upstream as a new dissipation mechanism. This works, however, only as long as the Mach number remains to be smaller than another critical Mach number $\mathscr{M} < \mathscr{M}_{\mathrm{wh,g}}$ that is based on the whistler group velocity, $\partial\omega/\partial k$,

$$\mathscr{M}_{\mathrm{wh,g}} = \left(\frac{27\, m_i}{64\, m_e}\right)^{\frac{1}{2}} |\cos\Theta_{Bn}| \lesssim 19.8, \quad (5.25)$$

since for larger $\mathscr{M}$ the whistler-wave energy will be confined to the shock and cannot propagate upstream. The right-hand estimate holds for an electron-proton plasma and $\cos\Theta_{Bn} \sim 0.707$, i.e. at the largest shock-normal angle $\Theta_{Bn} = 45^\circ$ of quasi-perpendicular shocks.

In other words, since the nonlinear whistler Mach number is always larger than the whistler-group Mach number, whistler energy will leave the shock upstream only in a narrow Mach number range $\mathscr{M}_{\mathrm{wh}} < \mathscr{M} < \mathscr{M}_{\mathrm{wh,g}} < \mathscr{M}_{\mathrm{wh,nl}}$. This range corresponds to $15 < \mathscr{M}/|\cos\Theta_{Bn}| < 19.8 < 21.3$. One-dimensional full particle PIC simulations with realistic mass ratio $m_i/m_e = 1840$ have been performed by *Scholer & Matsukiyo* [2004] and *Scholer & Burgess* [2007] and confirm that whistlers affect the stationary or non-stationary behaviour of nearly perpendicular shocks.

At larger $\mathscr{M} > 19.8|\cos\Theta_{Bn}|$ the whistler energy is again confined to the shock and will be swept downstream towards the shock when transported by the passing though continuously retarded flow. In the region of the foot and ramp where the energy accumulates it will cause different instabilities some of which propagate downstream. Such processes can be wave-wave interactions driven by the high whistler energy, as had already been envisaged by *Sagdeev* [1966], or nonlinear wave-particle interactions. In addition to causing anomalous resistivity and anomalous dissipation, these processes should lead to emission of plasma waves from the shock, preferably into the direction downstream of the shock, as only there $\mathscr{M} \lesssim 1$, and the wave group and phase velocities can exceed the speed of the flow.

This whole discussion refers only to whistler waves and follows the traditional route. We have, however, seen in the previous sections that the foot of the shock is capable of generating waves of another kind, electromagnetic Buneman modes, modified-two-stream waves, and possibly even Weibel modes. These waves are highly productive in generation of electron heating; they cause magnetic disturbances that move towards the shock or also upstream. The role in dissipation and dispersion these waves play has not yet been clarified and is subject to further investigation. It is, however, clear that their excitation and presence in the shock foot produces electron heating, retarding of ions and ion heating as well and will thus provide an efficient dissipation mechanism. Whether this can prevent shock breaking and overturning at very large Mach numbers is not known yet.

Shock Variability Due to Two-Stream and Modified Two-Stream Waves

Variability of the quasi-perpendicular shock has been demonstrated from numerical full particle PIC simulations in one and two dimensions to come about quite naturally for a wide range of – sufficiently large – Mach numbers. While in the low Mach number range whistlers are involved in the variability, reformation and non-stationarity, the simulations have clearly demonstrated that at higher Mach numbers the responsible waves are the Buneman two-stream mode and the modified two-stream instability. This has been checked [cf., *Matsukiyo & Scholer*, 2006a, b] by shock-independent simulations where the typical electron and ion phase space distributions have been used which occur in the vicinity of supercritical shocks during particle reflection events. So far the importance of these waves over whistlers has been investigated only for the shock-foot region. The shock ramp and overshoot are more difficult to model because of the presence of density and field gradients, their electrical non-neutrality, and the fuzziness of the particle phase-space distribution functions.

Differences were also found between strictly perpendicular and quasi-perpendicular shocks. The former are much stronger subject to the Buneman two-stream instability that completely rules the reformation process in one and two dimensions in this case, causing phase-space holes to evolve and being responsible for quasi-periodic changes in the positions, heights and widths of the shock front and foot regions, respectively. We have already put forward arguments that an investigation of the long-term behaviour of this quasi-periodic variation should reveal that this process is irregular in a statistical sense. Even under apparently periodic reformation conditions the shock will presumably not behave stationary on the short time and spatial scales. This, however, can be checked only with the help of long-term simulations which so far are inhibited if done with sufficiently many macro-particles, realistic mass ratios and in more than one-dimension.

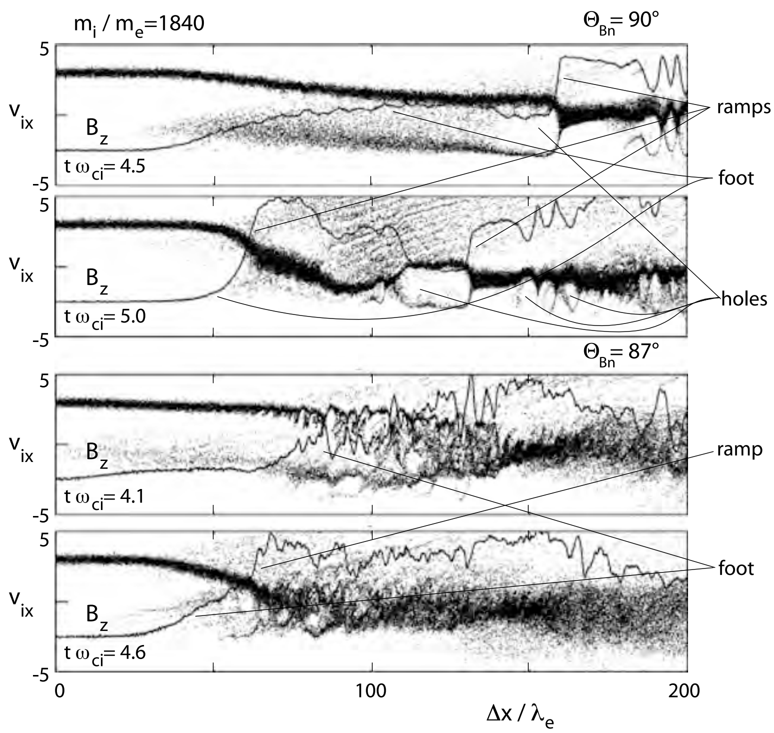

Figure 5.28: The completely different reformation behaviour of shocks in one-dimensional PIC simulations with realistic mass ratio of 1840 for strictly perpendicular and oblique quasi-perpendicular shocks at exactly same parameter settings and scales. Shown is the magnetic field B_z and the ion phase space at two subsequent simulation times for each of the respective simulations. Since the evolution is different in both cases the x-coordinate is given as a relative scale not in x but for the same interval lengths in Δx for the instance when reformation takes place in both cases [compiled from *Matsukiyo & Scholer*, 2006a, courtesy American Geophysical Union]. *Top*: Reformation at $\Theta_{Bn} = 90^\circ$ at two times showing the evolution of the foot in the magnetic field and the taking-over of the ramp by the foot while a new foot evolves. This process is governed by the Buneman two-stream instability. Large holes evolve on the ion distribution. Note the correlation of the ion holes with depressions in the magnetic field. In the *second panel* the old ramp is still visible as the boundary of the large ion hole. Farther downstream many holes are seen, each of them corresponding to a magnetic depression, and the regions between characterised by magnetic overshoots. *Bottom*: The corresponding evolution at $\Theta_{Bn} = 87^\circ$. High variability of the shock profile is observed which is identified as being due to the large amplitude MTS-waves travelling into the shock. The foot region is extended and very noisy both in the magnetic field and ion distributions, the latter being highly structured. The foot is extended much longer than in the perpendicular case. The *two bottom panels* might also show signatures of wave breaking in the ion velocities when groups of ions appear which overturn the main flow in forward downstream direction.

Figure 5.28 provides an impression of the variability of shock reformation in the two cases of a strictly perpendicular, highly supercritical shock, and the case of an oblique supercritical shock at $\Theta_{Bn} = 87^\circ$, when whistler excitation is absent. The settings of the simulations are otherwise identical, but the evolution of the two simulations is completely unrelated. This is because the perpendicular shock does not allow, in these one-dimensional simulations, for the modified two-stream instability to grow. So only the Buneman two-stream instability grows. It reforms the foot in the way we have already described, forming large holes and letting the shock ramp jump ahead in time-steps of the order of roughly an ion gyro-period. The shock foot acts decelerating on the flow, and already during reformation begins to reflect ions and to form a new foot. Most interestingly is that the holes survive quite a while downstream while being all the time related to magnetic depressions. At their boundaries large magnetic walls form which can be interpreted as magnetic compressions (or otherwise signatures of current vortices).

The oblique case looks different. It is highly variable both in time and in space. The magnetic profile is more irregular, and the ion-phase space exhibits much more structure than in the perpendicular case. This has been identified to be due to the combined action of the Buneman two-stream and the modified two-stream instabilities with the two-stream instability being important only during the initial state of the reformation process, while the modified two-stream instability dominates the later nonlinear evolution. Both, foot and ramp, are extended and vary strongly. It is quite obvious, that in this case one can speak of a stationary shock front only when referring to the long-term behaviour of the shock, much longer than the irregular reformation cycle lasts. At the scale of reformation and below there is no stationarity but variability and evolution, which can be attributed to the growth and interaction times of the MTSI and the various secondary processes caused by it.

To complete this section, we note in passing that the low-mass ratio two-dimensional full particle PIC simulations with small particle numbers performed by *Lembège & Savoini* [1992, 2002] and *Savoini & Lembège* [1994, 2001] also showed non-stationary behaviour of the quasi-perpendicular – or perpendicular – shock leading to so-called "rippling" of shocks, which we will briefly describe in the next paragraph.

5.5.2 Formation of Ripples

One-dimensional theory and one-dimensional simulations implicitly treat the shock as an infinitely extended plane surface. In addition they allow only for instabilities to evolve in the direction of the shock normal at an angle relatively close to 90° such that any waves along the shock surface are completely excluded and waves parallel to the magnetic field have very small wave numbers $k_\| = k_x \cos\Theta_{Bn} \ll k_x$ corresponding to very long parallel wavelengths. To be more realistic, two-dimensional PIC simulations have been performed to investigate the effect of the additional freedom given by the second spatial dimension which allows instabilities to evolve in other than the shock normal direction. The cost of these simulations is being restricted to low mass ratios only. In the simulation of *Lembège & Savoini* [1992, 2002] and *Savoini & Lembège* [1994, 2001] the mass ratio has been taken as $m_i/m_e = 42$ which implies from comparison to the high-mass ratios in one-dimensional simulations that the modified two-stream instability will presumably be excluded. The structure of the shock front in these simulations has been shown in Figure 5.8, the left-hand side of which shows the cyclic reformation of the shock – which at these low mass ratios is clearly expected to occur – at a period comparable to the ion-gyro period of the reflected

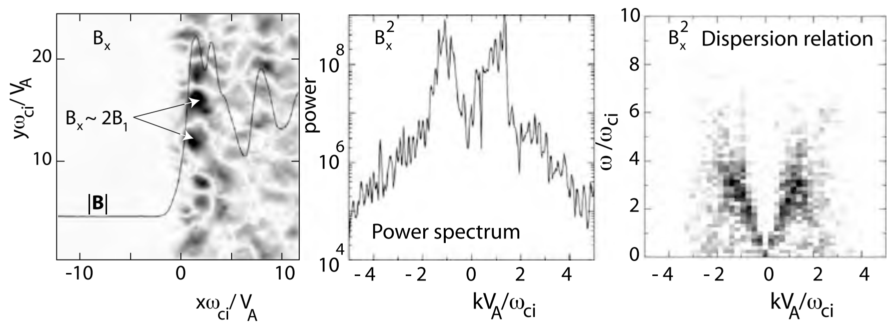

Figure 5.29: *Left*: Spatial distribution of the $B_n = B_x$-component of the magnetic field in the hybrid simulations of *Lowe & Burgess* [2003] with Mach number $\mathscr{M}_A = 5.7$, and for $\Theta_{Bn} = 88°$. The B_x-component is not zero; it reaches values twice the upstream magnetic field B_1 and shows quite structured behaviour along the shock surface which indicates that the surface is oscillating back and forth and that waves are running along the surface. These waves are interpreted as surface waves. *Centre*: The power in the presumable surface waves as determined from the simulations. Obviously the power concentrates around the ramp. *Right*: Apparent dispersion relation $\omega(k)$ of the fluctuations [after *Lowe & Burgess*, 2003].

ions in the foot of the shock. The right-hand side shows a pseudo-three-dimensional profile of the shock in the two spacial dimensions, in the top part at the time when the foot is fully developed, in the bottom part when the ramp has just reformed, i.e. when the foot has taken over to become the ramp. What interests us here is that the shock ramp surface is by no means a smooth plane in the direction tangential to the shock. It exhibits large variations both in space and time which are correlated but not directly in phase with the presence of reflected ions in the foot. The overshoot, steepness and width of the ramp and ramp position oscillate at a not strictly periodical time-scale. In addition, the structure of the ramp also exhibits shorter scale fluctuations.

Further hybrid simulations [*Lowe & Burgess*, 2003; *Burgess & Scholer*, 2007] in two dimensions at $\Theta_{Bn} = 88°$ for and $\mathscr{M}_A = 5.7$ satisfying Rankine-Hugoniot conditions with $\mathbf{n}\cdot\mathbf{B} = B_n$ constant, attribute fluctuations in B_n to these so-called ripples [*Lembège & Savoini*, 2002; *Lowe & Burgess*, 2003; *Burgess*, 2006a, b] as given in Figure 5.29 for the $B_n = B_x$ (left), power B_x^2 (centre), and the 'dispersion relation' $\omega(k)$ of the fluctuations in B_x. These fluctuations are of the same value as the main component of the magnetic field B_z reaching maximum values of twice the upstream magnetic field B_1. They are concentrated in the ramp, foot and overshoot. The dispersion relation is about linear and low frequency but exceeds the ion-cyclotron frequency for shorter wavelengths. There is no mode known which corresponds to these waves, so they are attributed to surface waves flowing in the shock transition. Maximum wavelengths are a few ion inertial lengths.

The lesson learned is, however, quite simple: the shock exhibits structure along its surface which can presumably be attributed to waves running along the shock front and modulating it temporarily and spatially. The caveat of these simulations is however, their hybrid character which does not account for the full dynamics of the particles and therefore it cannot be concluded about the nature of the waves. *Burgess & Scholer* [2007] have

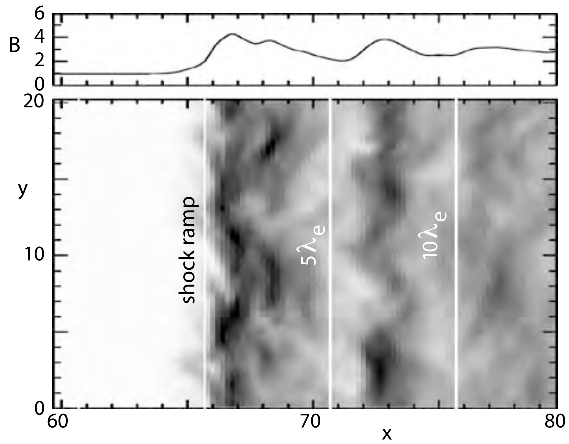

Figure 5.30: Two-dimensional structure of the surface waves [*Burgess & Scholer*, 2007]. *Top*: Magnetic field average across the shock. *Bottom*: *Grey scale plot* of the surface waves. The *three white lines* show the presumable location of the nominal shock and two distances from it downstream [after *Burgess*, 2006b, courtesy American Geophysical Union].

extended these investigations to infer about the driver of these waves. They find that it is the reflected ion component in the shock foot which flows along the shock surface and at large Mach numbers becomes unstable. Figure 5.30 shows a grey scale plot of the two-dimensional structure of the surface wave oscillation. Its growth is proportional to the Mach number, i.e. it must therefore be proportional to the number of reflected ions, their velocity and to the upstream convection electric field that accelerates the ions. Presumably it is some variant of Kelvin-Helmholtz instability along the shock surface, which is driven by the velocity shear introduced by the reflected ion flow along the shock surface. It causes undulations (or flow vortices) at the shock which, in the magnetic field, appear as ripples.

It should be clear, however, that long-term full particle simulations must be performed at real mass ratio before any reliable conclusion can be drawn about the existence of surface waves. We have seen that part of these waves is nothing but the exchange between the foot and the ramp during the reformation process. This applies to the long wave part. In addition it is indeed possible that the strong and fast flow of reflected ions along the shock surface could excite a Kelvin-Helmholtz-like instability. This depends on the fraction of ions which the shock is able to reflect, and this is a question of Mach number dependence. If the fraction of reflected ions is small the velocity shear will be too small to drive a Kelvin-Helmholtz instability. Giving a quantitative argument is, unfortunately, impossible. However, it is not clear whether these oscillations are the sole action of the modulation of the shock surface in two or three dimensions. The only conclusion we can safely draw is that the shock surface, even under ideal non-curved and quiet upstream conditions, will at high Mach numbers not remain to be a quiet smooth and stable shock surface but will exhibit fluctuations in position, structure, overshoot amplitude and width on the scales of the ion inertial length and the ion cyclotron period.

5.6 Summary and Conclusions

Among the collisionless shocks, quasi-perpendicular supercritical shocks are the best investigated. They are also the shocks which for other purposes like particle acceleration to very high energies have naturally been favoured and find wide application in astrophysics where one of the central problems consists in the explanation of the presence of energetic particles (Cosmic Rays). Theory has predicted that quasi-perpendicular shocks reflect ions by some basically unspecified mechanism that for simplicity is assumed to be specular, implying elastic scattering from the shock front. This might be provided for the low energy part of the upstream distribution by the transverse shock potential. These reflected ions form feet which are located upstream but adjacent to the shock ramps. Quasi-perpendicular shocks possess either whistler precursors are trails. Theory also predicts that whistlers could be phase-locked and stand in front of the shock ramp only for a limited range of Alfvénic Mach numbers.

We have reviewed here the theoretically expected shock structure, the relevant scales, the most relevant particle simulations for perpendicular and quasi-perpendicular supercritical shocks, the shock-reformation process and its physics as far as it could be elucidated from one-dimensional and to a certain part also from two-dimensional simulations. The most relevant instabilities generated in the shock foot have been identified as the whistler instability for nearly perpendicular supercritical but low-Mach number shocks, leading to foot formation but not being decisive for feet, as it has turned out that feet in this Mach number and shock-normal angle ranges are produced by accumulation of gyrating ions at the upward edge of the foot.

More important than whistlers have turned out the Buneman and modified two-stream modes, the former dominating shocks at perpendicular angles, the latter growing slowly but dominating at more oblique angles and at later simulation times with the effect of completely restructuring both the shock feet and ramps. Both instabilities generate phase space holes which during reformation survive and are added to the downstream plasma and, in addition, being responsible for low magnetic field values.

Most interestingly, the plasma state just downstream of the shock is, at least to large extent, nothing else but the collection of the old shock ramps which have been left over from former reformation cycles and move relative to the shock frame in the direction downstream of the shock. This is best seen in the simulations when analysing the ion phase space where each of the old ramps can still be identified as an ion clump, the remainder of the former ramp reflection position.

The modified-two-stream instability in addition generates waves which flow into the shock ramp where they contribute to the dynamics of the ramp. Wave-wave interaction and wave particle interaction lead to the generation of secondary waves and to particle heating. Finally, simulations show that the shock front in more than one dimension is not a plane surface but exhibits a strong variability in time and space. This can be explained as surface waves on the shock front which might be driven by the reflected ion current flow along the surface similar to a Kelvin-Helmholtz instability. This question is still open to investigation. So far the evolution of the shock ramp, its stability and time variation as well as the physics of the region just downstream of the ramp is not yet well explored. It is, however, clear from the available intelligence that any serious investigation must be based on full particle simulations and experimenting with appropriate sets of distribution functions suggested by the simulations in order to investigate the instabilities and interactions between the waves and particles as well as between waves and waves in order to understand the physics. This has to a certain degree already been achieved for the foot region. In the shock ramp and in the strongly disturbed region behind the ramp it is more difficult as the conditions there are less clean and the definition of the responsible distributions is more difficult. Moreover, plasma and field gradients must be taken into account in this region, and the electric charge separation field that is partially responsible for ion reflection cannot be neglected as well. With the further increase of computing capacity and the refinement of the models one expects that within the next decade also the physics of the shock ramp will become more transparent.

An interesting problem is the stability of shocks. Above the critical Mach number they reflect ions and generate ion viscosity that helps dissipating the excess energy. This dissipation goes via the above mentioned instabilities and less on the way of ion viscosity in the classical sense of fluid theory. For even larger Mach numbers these processes will not suffice to stabilise a quasi-perpendicular shock. What will then happen? It has been suggested that strongly nonlinear processes driven by whistlers will set on and lead to non-stationarity of the shock ramp. This might be the case. However, only simulations at high Mach numbers and full mass ratios in large enough systems can answer this question.

We state that the problem of stationarity or cyclic behaviour of the shock is not the problem of the shock; rather it is the problem of our understanding. For the shock nothing else counts than dissipating the excess inflow energy and momentum. If this turns out to be impossible by either anomalous dissipation, shock reflection, foot formation, precursors and early flow retarding, then the shock will not care but will break and turn over as this will be the only way for reducing the scale to microscopic dimensions producing violent heating and energy dissipation.

At the time of writing it remains unclear whether breaking takes place. Magnetic field lines cannot break-off; they kink but remain to be simply connected. Hence, any breaking that is going on takes place in the particle component requiring non-adiabaticity. It will be connected with vortex formation. The appearance of phase space vortices at high Mach numbers resembles a tendency towards shock breaking. In the light of this discussion the lower two panels in Figure 5.28 can also be interpreted as breaking and overturning of the quasi-perpendicular ($\Theta_{Bn} = 87^\circ$) realistic mass-ratio supercritical shock. In particular during the phase before reformation (third panel from top) the magnetic field behaves irregular, and both the incoming and reflected beams form many partial vortices prior to the reflection point (at $\Delta x \sim 140\,\lambda_e$). Behind the reflection point the ion velocity shows formation of bursts of ions which run away in forward direction, which is just what is expected in breaking. A sketch of the dynamical processes is given in Figure 5.31.

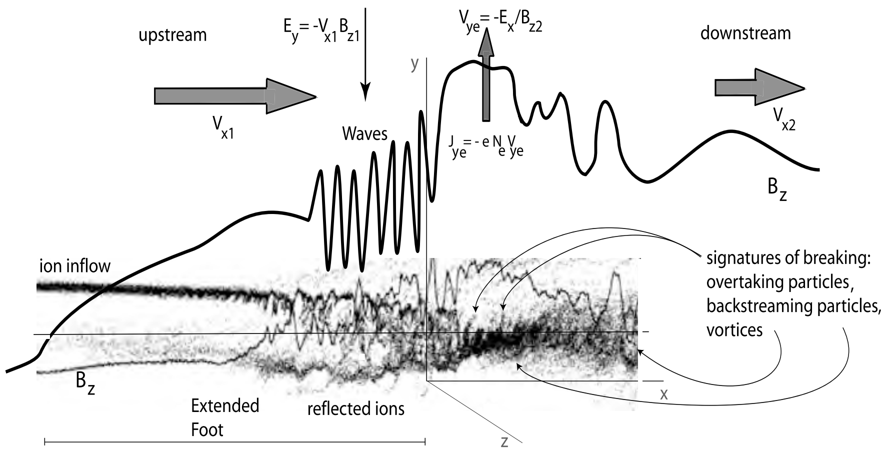

Figure 5.31: Schematic of the profile of a highly supercritical shock with waves just before shock reformation and signatures of beginning wave breaking. The sketch has been completed with a copy of the ion phase space from the simulations of *Matsukiyo & Scholer* [2006b] showing the structure of the ions in the ramp with the signatures of overtaking ions and backstreaming ions as well as ion vortices, all an indication of onset of breaking.

5.7 Update – 2012

Nonstationarity viz. shock reformation has been investigated at the example of Earth's bow shock wave with the help of CLUSTER spacecraft measurements by *Mazelle et al* [2010] showing that the ramp-gradient scale changes with time and can become as narrow as an electron inertial length, which is a most interesting observation as this is the shortest possible transverse length scale for a collisionless magnetised shock.

Related to this observation may be another observation by *Bale et al* [2008] who used CLUSTER measurement across the quasi-perpendicular super-critical bow shock wave at low plasma β to determine the cross-shock electric potential finding that the potential is typically in the range of $500 < \Phi < 2500$ V which amounts to large variations in the ion energy change in the range $20 < \Delta\mathscr{E}_{ion}/\mathscr{E}_{ion} < 240\%$. This would be indication of the high variability of the shock.

The cross-shock potential is also related to electron heating as described in this chapter. However, direct multi-spacecraft CLUSTER measurements analysed by *Schwartz et al* [2011] that this electron heating is a more complex and obviously multi-scale process which is related to the spatial and temporal structure of the shock layer electromagnetic field. These authors determined the electron temperature gradient across the quasi-perpendicular Earth's bow shock from the electron distribution measured *in situ*. According to these observations, roughly $\sim$50% of the electron heating must be attributed to the narrow few λ_e thick shock ramp layer. This heating comes from an inflation the electron phase space and indicates irreversibility which is attributed to wave particle interaction. In view of this the conclusion that wave turbulence in a narrow transition region practically independent on ion dynamics is responsible for the electron heating. This is, however, consistent with the assertion that violent instabilities work in this narrow region like the Buneman mode, the modified two-stream instability caused by the shock-electric potential. Possibly, as the authors suggest, oblique electron whistlers are also involved. *Sundkvist et al* [2009]; *Sundkvist et al* [2012], based on CLUSTER multi-spacecraft observations from crossings of Earth's bow shock, calculated the Poynting flux of such oblique whistler waves in two quasi-perpendicular ($\Theta_{Bn} \sim 85^\circ$) relatively high-Mach ($\mathscr{M}_A = 5.5$ and 11) number shocks finding – in the shock-normal frames – that the Poynting flux is directed obliquely upstream, away from the shock, as predicted by quasi-perpendicular supercritical shock theory. Their assumption is that the parallel electric field vanishes. Thus the whistlers generated at the shock are oblique and dispersive with k-vector approaching 90° with respect to the ambient magnetic field at the shock ramp. Downstream of the shock, the wave spectrum becomes incoherent, indicating that the waves in the whistler frequency range are turbulent. We note that recently [*Wilson et al*, 2012] electromagnetic whistler precursor waves have also been inferred from Wind data around some supercritical interplanetary shocks.

Shinohara & Fujimoto [2010] have preformed first three-dimensional PIC simulations of quasi-perpendicular shocks at a realistic mass ratio $\mu = 1840$ finding very strong wave activity in the shock foot region which is permitted by the inclusion of the third dimension. These waves cause a stronger then known upstream electron acceleration and the generation of non-thermal electrons. PIC simulations at smaller mass ratio and in two dimensions [*Savoini et al*, 2010] had already shown indications of reflected electrons before and attributed them to a magnetic mirror effect in the foot-shock ramp field.

Also of interest is the observation of a variability of electron counts at 500 eV electron energy observed downstream of the super-critical quasi-perpendicular bow shock by CLUSTER [*Matsui et al*, 2011]. It suggests a quasi-periodic modulation of electron flux at this energy with period ~3 s, suggested to be related to mirror mode waves excited by the presumably large downstream temperature anisotropy that is generated by the quasi-perpendicular shock transition.

Near the Saturnian bow shock, *Masters et al* [2011] found substantial solar wind electron heating from Cassini data during 2005 and 2007, attributing the heating to the action of the comparably strong bow shock at this outer strongly magnetised planet. The heating observed is correlated to the ram flow energy of the incident solar wind, e.g. to the upstream Mach number. It amounts to between 3% and 7% of the incident ram energy.

References

Auer PL, Hurwitz H, Kilb RW (1962) Large amplitude compression of a collision-free plasma II. Development of a thermalized plasma. Phys Fluids 5:298–316. doi:10.1063/1.1706615

Bale SD, Hull A, Larson DE, Lin RP, Muschietti L, Kellogg PJ, Goetz K, Monson SJ (2002) Electrostatic turbulence and Debye-scale structures associated with electron thermalization at collisionless shocks. Astrophys J 575:L25–L28. doi:10.1086/342609

Bale SD, Mozer FS (2007) Measurement of large parallel and perpendicular electric fields on electron spatial scales in the terrestrial bow shock. Phys Rev Lett 98:205001. doi:10.1103/PhysRevLett.98.205001

Bale SD, Mozer FS, Horbury TS (2003) Density-transition scale at quasiperpendicular collisionless shocks. Phys Rev Lett 91:265004. doi:10.1103/PhysRevLett.91.265004

Bale SD, Mozer FS, Krasnoselskikh VV (2008) Direct measurement of the cross-shock electric potential at low plasma β, quasi-perpendicular bow shocks. arXiv:0809.2435

Balikhin MA, Krasnosel'skikh V, Gedalin MA (1995) The scales in quasiperpendicular shocks. Adv Space Res 15:247–260. doi:10.1016/0273-1177(94)00105-A

Balikhin MA, Walker S, Treumann R, Alleyne H, Krasnoselskikh V, Gedalin M, Andre M, Dunlop M, Fazakerley A (2005) Ion sound wave packets at the quasiperpendicular shock front. Geophys Res Lett 32:L24106. doi:10.1029/2005GL024660

Biskamp D (1973) Collisionless shock waves. Nucl Fusion 13:719–740

Biskamp D, Welter H (1972) Structure of the Earth's bow shock. J Geophys Res 77:6052–6059. doi:10.1029/JA077i031p06052

Burgess D (2006a) Simulations of electron acceleration at collisionless shocks: the effects of surface fluctuations. Astrophys J 653:316–324. doi:10.1086/508805

Burgess D (2006b) Interpreting multipoint observations of substructure at the quasi-perpendicular bow shock: simulations. J Geophys Res 111:A10210. doi:10.1029/2006JA011691

Burgess D, Scholer M (2007) Shock front instability associated with reflected ions at the perpendicular shock. Phys Plasmas 14:012108. doi:10.1063/1.2435317

Czaykowska A, Bauer TM, Treumann RA, Baumjohann W (1998) Mirror waves downstream of the quasi-perpendicular bow shock. J Geophys Res 103:4747–4753. doi:10.1029/97JA03245

Edmiston JP, Kennel CF (1984) A parametric survey of the first critical Mach number for a fast MHD shock. J Plasma Phys 32:429–441. doi:10.1017/S002237780000218X

Eselevich VG (1982) Shock-wave structure in collisionless plasmas from results of laboratory experiments. Space Sci Rev 32:65–81. doi:10.1007/BF00225177

Feldman WC, Anderson RC, Bame SJ, Gary SP, Gosling JT, McComas DJ, Thomsen MF, Paschmann G, Hoppe MM (1983) Electron velocity distributions near the Earth's bow shock. J Geophys Res 87:96–110. doi:10.1029/JA088iA01p00096

Formisano V, Torbert R (1982) Ion acoustic wave forms generated by ion-ion streams at the Earth's bow shock. Geophys Res Lett 9:207–210. doi:10.1029/GL009i003p00207

Forslund DW, Morse RL, Nielson CW (1970) Electron cyclotron drift instability. Phys Rev Lett 25:1266–1269. doi:10.1103/PhysRevLett.25.1266

Forslund DW, Shonk CR (1970) Numerical simulation of electrostatic counterstreaming instabilities in ion beams. Phys Rev Lett 25:281–284. doi:10.1103/PhysRevLett.25.281

Galeev AA, Krasnosel'skikh VV, Lobzin VV (1988) Fine structure of the front of a quasi-perpendicular supercritical collisionless shock wave. Sov J Plasma Phys 14:697–702

Goodrich CC, Scudder JD (1984) The adiabatic energy change of plasma electrons and the frame dependence of the cross-shock potential at collisionless magnetosonic shock waves. J Geophys Res 89:6654–6662. doi:10.1029/JA089iA08p06654

Gurnett DA (1985) Plasma waves and instabilities. In: Tsurutani BT, Stone RG (eds) Collisionless shocks in the heliosphere: reviews of current research. AGU, Washington, pp 207–224

Gurnett DA, Neubauer FM, Schwenn R (1979) Plasma wave turbulence associated with an interplanetary shock. J Geophys Res 84:541–552. doi:10.1029/JA084iA02p00541

Hada T, Oonishi M, Lembège B, Savoini P (2003) Shock front nonstationarity of supercritical perpendicular shocks. J Geophys Res 108:1233. doi:10.1029/2002JA009339

Hellinger P, Trávníček P, Lembège B, Savoini P (2007) Emission of nonlinear whistler waves at the front of perpendicular supercritical shocks: hybrid versus full particle simulations. Geophys Res Lett 34:L14109. doi:10.1029/2007GL030239

Hellinger P, Trávníček P, Matsumoto H (2002) Reformation of perpendicular shocks: hybrid simulations. Geophys Res Lett 29:2234. doi:10.1029/2002GL015915

Hobara Y, Waker SN, Balikhin M, Pokhotelov OA, Gedalin M, Kransnoselskikh V, Hayakawa M, André M, Dunlop M, Rème H, Fazakerley A (2008) Cluster observations of electrostatic solitary waves near the Earth's bow shock. J Geophys Res 113:A05211. doi:10.1029/2007JA012789

Hull AJ, Larson DE, Wilber M, Scudder JD, Mozer FS, Russell CT, Bale SD (2006) Large-amplitude electrostatic waves associated with magnetic ramp substructure at Earth's bow shock. Geophys Res Lett 33:L15104. doi:10.1029/2005GL025564

Kazantsev AP (1961) Flow of a conducting gas past a current-carrying plate. Sov Phys Dokl 5:771–773

Kennel CF, Edmiston JP, Hada T (1985) A quarter century of collisionless shock research. In: Stone RG, Tsurutani BT (eds) Collisionless shocks in the heliosphere: a tutorial review. AGU, Washington, pp 1–36

Krasnoselskikh VV, Lembège B, Savoini P, Lobzin VV (2002) Nonstationarity of strong collisionless quasiperpendicular shocks: theory and full particle numerical simulations. Phys Plasmas 9:1192–1201. doi:10.1063/1.1457465

Kuncic Z, Cairns IH, Knock S (2002) Analytic model for the electrostatic potential jump across collisionless shocks, with application to Earth's bow shock. J Geophys Res 107:1218. doi:10.1029/2001JA000250

Lembège B, Dawson JM (1987a) Plasma heating through a supercritical oblique collisionless shock. Phys Fluids 30:1110–1114. doi:10.1063/1.866309

Lembège B, Dawson JM (1987b) Self-consistent study of a perpendicular collisionless and nonresistive shock. Phys Fluids 30:1767–1788. doi:10.1063/1.866191

Lembège B, Savoini P (1992) Nonstationarity of a two-dimensional quasiperpendicular supercritical collisionless shock by self-reformation. Phys Fluids 4:3533–3548. doi:10.1063/1.860361

Lembège B, Savoini P (2002) Formation of reflected electron bursts by the nonstationarity and nonuniformity of a collisionless shock front. J Geophys Res 107:1037. doi:10.1029/2001JA900128

Lembège B, Walker SN, Savoini P, Balikhin MA, Krasnoselskikh V (1999) The spatial sizes of electric and magnetic field gradients in a simulated shock. Adv Space Res 24:109–112. doi:10.1016/S0273-1177(99)00435-4

Leroy MM (1984) Computer simulations of collisionless shock waves. Adv Space Res 4:231–243. doi:10.1016/0273-1177(84)90317-X

Leroy MM, Goodrich CC, Winske D, Wu CS, Papadopoulos K (1981) Simulation of a perpendicular bow shock. Geophys Res Lett 8:1269–1272. doi:10.1029/GL008i012p01269

Leroy MM, Winske D, Goodrich CC, Wu CS, Papadopoulos K (1982) The structure of perpendicular bow shocks. J Geophys Res 87:5081–5094. doi:10.1029/JA087iA07p05081

Lowe RE, Burgess D (2003) The properties and causes of rippling in quasi-perpendicular collisionless shock fronts. Ann Geophys 21:671–679. doi:10.5194/angeo-21-671-2003

Masters A, Schwartz SJ, Henley EM, Thomsen MF, Zieger B, Coates AJ, Achilleos N, Mitchell J, Hansen KC, Dougherty MK (2011) Electron heating at Saturn's bow shock. J Geophys Res 116:A10107 doi:10.1029/2011JA016941

Matsui H, Torbert RB, Baumjohann W, Kucharek H, Schwartz SJ, Mouikis CG, Vaith H, Kistler LM, Lucek EA, Fazakerley AN, Miao B, Paschmann G (2011) Oscillation of electron counts at 500 eV downstream of the quasi-perpendicular bow shock, J Geophys Res 113:A08223. doi:10.1029/2007JA012939

Matsukiyo S, Scholer M (2003) Modified two-stream instability in the foot of high Mach number quasi-perpendicular shocks. J Geophys Res 108: ID 1459. doi:10.1029/2003JA010080

Matsukiyo S, Scholer M (2006a) On microinstabilities in the foot of high Mach number perpendicular shocks. J Geophys Res 111:A06104. doi:10.1029/2005JA011409

Matsukiyo S, Scholer M (2006b) On reformation of quasi-perpendicular collisionless shocks. Adv Space Res 38:57–63. doi:10.1016/j.asr.2004.08.012

Mazelle CX, Lembege B, Morgenthaler A, Meziane K (2010) Nonstationarity of quasi-perpendicular shocks: magnetic structure, ion properties and micro-turbulence. AGU Fall Meeting Abstracts, SM51B-1792

Meziane K, Hamza AM, Wilber M, Mazelle C, Lee MA (2011) Anomalous foreshock field-aligned beams observed by cluster. Ann Geophys 29:1967–1975. doi:10.5194/angeo-29-1967-2011

Morse DL, Destler WW, Auer PL (1972) Nonstationary behavior of collisionless shocks. Phys Rev Lett 28:13–16. doi:10.1103/PhysRevLett.28.13

Moullard O, Burgess D, Horbury TS, Lucek EA (2006) Ripples observed on the surface of the Earth's quasi-perpendicular bow shock. J Geophys Res 111:A09113. doi:10.1029/2005JA011594

Muschietti L, Lembège B (2006) Electron cyclotron microinstability in the foot of a perpendicular shock: a self-consistent PIC simulation. Adv Space Res 37:483–493. doi:10.1016/j.asr.2005.03.077

Papadopoulos K (1985) Microinstabilities and anomalous transport. In: Stone RG, Tsurutani BT (eds) Collisionless shocks in the heliosphere: a tutorial review. AGU Washington, pp 59–90

Papadopoulos K (1988) Electron heating in superhigh Mach number shocks. Astrophys Space Sci 144:535–547. doi:10.1007/BF00793203

Papadopoulos K, Davidson RC, Dawson JM, Haber I, Hammer D A, Krall NA, Shanny R (1971) Heating of counterstreaming ion beams in an external magnetic field. Phys Fluids 14:849–857. doi:10.1063/1.1693520

Papadopoulos K, Wagner CE, Haber I (1971a), High-Mach-number turbulent magnetosonic shocks. Phys Rev Lett 27:982–986. doi:10.1103/PhysRevLett.27.982

Paul PWM, Goldenbum GC, Iiyoshi A, Holmes LS, Hardcastle RA (1967) Measurement of electron temperatures produced by collisionless shock waves in a magnetized plasma. Nature 216:363–364. doi:10.1038/216363a0

Pickett JS, Kahler SW, Chen LJ, Huff RL, Santolik O, Khotyaintsev Y, Décréau PME, Winningham D, Frahm R, Goldstein ML, Lakhina GS, Tsurutani BT, Lavraud B, Gurnett DA, André M, Fazakerley A, Balogh A, Rème H (2004) Solitary waves observed in the auroral zone: the Cluster multi-spacecraft perspective. Nonlinear Process Geophys 12:183–196

Quests KB (1986) Simulations of high Mach number perpendicular shocks with resistive electrons. J Geophys Res 91:8805–8815. doi:10.1029/JA091iA08p08805

Rodriguez P, Gurnett DA (1975) Electrostatic and electromagnetic turbulence associated with the Earth's bow shock. J Geophys Res 80:19–31. doi:10.1029/JA080i001p00019

Sagdeev RZ (1966) Cooperative phenomena in collisionless plasmas. In: Leontovich MA (ed) Rev plasma phys, vol 4. Consultants Bureau, New York, pp 32–91

Savoini P, Lembège B (1994) Electron dynamics in two- and one-dimensional oblique supercritical collisionless magnetosonic shocks. J Geophys Res 99:6609–6635. doi:10.1029/93JA03330

Savoini P, Lembège B (2001) Two-dimensional simulations of a curved shock: self-consistent formation of the electron foreshock. J Geophys Res 106:12975–12992. doi:10.1029/2001JA900007

Savoini P, Lembège B (2010) Non-adiabatic electron behavior through a supercritical perpendicular collisionless shock: impact of the shock front turbulence. J Geophys Res 115:A11103. doi:10.1029/2010JA015381

Savoini P, Lembége B, Stienlet J (2010) Origin of backstreaming electrons within the quasi-perpendicular foreshock region: two-dimensional self-consistent PIC simulation. J Geophys Res 115:A09104. doi:10.1029/2010JA015263

Schmitz H, Chapman SC, Dendy RO (2002) Electron preacceleration mechanisms in the foot region of high Alfvénic Mach number shocks. Astrophys J 579:327–336. doi:10.1086/341733

Scholer M, Burgess D (2006) Transition scale at quasiperpendicular collisionless shocks: full particle electromagnetic simulations. Phys Plasmas 13:062101. doi:10.1063/1.2207126

Scholer M, Burgess D (2007) Whistler waves, core ion heating, and nonstationarity in oblique collisionless shocks. Phys Plasmas 14:072103. doi:10.1063/1.2748391

Scholer M, Matsukiyo S (2004) Nonstationarity of quasi-perpendicular shocks: a comparison of full particle simulations with different ion to electron mass ratio. Ann Geophys 22:2345–2353. doi:10.5194/angeo-22-2345-2004

Scholer M, Shinohara I, Matsukiyo S (2003) Quasi-perpendicular shocks: length scale of the cross-shock potential, shock reformation, and implication for shock surfing. J Geophys Res 108: ID 1014. doi:10.1029/2002JA009515

Schwartz SJ, Henley E, Mitchell J, Krasnoselskikh V (2011) Electron temperature gradient scale at collisionless shocks. Phys Rev Lett 107:215002. doi:10.1103/PhysRevLett.107.215002

Schwartz SJ, Thomsen MF, Gosling JT (1983) Ions upstream of the Earth's bow shock – a theoretical comparison of alternative source populations. J Geophys Res 88:2039–2047. doi:10.1029/JA088iA03p02039

Sckopke N, Paschmann G, Bame SJ, Gosling JT, Russell CT (1983) Evolution of ion distributions across the nearly perpendicular bow shock – specularly and non-specularly reflected-gyrating ions. J Geophys Res 88:6121–6136. doi:10.1029/JA088iA08p06121

Scudder JD (1995) A review of the physics of electron heating at collisionless shocks. Adv Space Res 15:181–223. doi:10.1016/0273-1177(94)00101-6

Scudder JD, Aggson TL, Mangeney A, Lacombe C, Harvey CC (1986) The resolved layer of a collisionless, high beta, supercritical, quasi-perpendicular shock wave. I – Rankine-Hugoniot geometry, currents, and stationarity, II – Dissipative fluid electrodynamics, III – Vlasov electrodynamics. J Geophys Res 91:11019–11097. doi:10.1029/JA091iA10p11019

Shimada N, Hoshino M (2000) Strong electron acceleration at high Mach number shock waves: simulation study of electron dynamics. Astrophys J 543:L67–L71. doi:10.1086/318161

Shimada N, Hoshino M (2005) Effect of strong thermalization on shock dynamical behavior. J Geophys Res 110:A02105. doi:10.1029/2004JA010596

Shinohara I, Fujimoto M (2010) Results of a 3-D full particle simulation of quasi-perpendicular shock. AGU Fall Meeting Abstracts, SH51D-1724

Shinohara I, Fujimoto M (2011) Electron acceleration in the foot region of a quasi-perpendicular shock. AGU Fall Meeting Abstracts, SH41D-1904

Sundkvist DJ, Krasnoselskikh V, Bale S (2009) AGU Fall Meeting Abstracts, A1453

Sundkvist DJ, Krasnoselskikh V, Bale SD, Schwartz SJ, Soucek J, Mozer F (2012) Dispersive nature of high Mach number collisionless plasma shocks: Poynting flux of oblique whistler waves. Phys Rev Lett 108:025002. doi:10.1103/PhysRevLett.108.025002

Umeda T, Yamazaki R (2006) Full particle simulation of a perpendicular collisionless shock: a shock-rest-frame model. Earth Planets Space 58:e41–e44

Walker SN, Alleyne H, Balikhin M, André M, Horbury T (2004) Electric field scales at quasi-perpendicular shocks. Ann Geophys 22:2291–2300. doi:10.5194/angeo-22-2291-2004

Weibel ES (1959) Spontaneously growing transverse waves in a plasma due to an anisotropic velocity distribution. Phys Rev Lett 2:83–84. doi:10.1103/PhysRevLett.2.83

Whitham GB (1974) Linear and nonlinear waves. Wiley-Interscience, New York

Wilson LB III, Koval A, Szabo A, Breneman A, dattell CA, Goetz K, Kellogg PJ, Kersten K, Kasper JC, Maruca BA, Pulupa M (2012) Observations of electromagnetic whistler precursors at supercritical interplanetary shocks. Geophys Res Lett 39:L08109. doi:10.1029/2012GL051581

Winske D, Quest KB (1988) Magnetic field and density fluctuations at perpendicular supercritical collisionless shocks. J Geophys Res 93:9681–9693. doi:10.1029/JA093iA09p09681

Wu CS, Winske D, Papadopoulos K, Zhou YM, Tsai ST, Guo SC (1983) A kinetic cross-field streaming instability. Phys Fluids 26:1259–1267. doi:10.1063/1.864285

Wu CS, Winske D, Tanaka M, Papadopoulos K, Akimoto K, Goodrich CC, Zhou YM, Tsai ST, Rodriguez P, Lin CS (1984) Microinstabilities associated with a high Mach number, perpendicular bow shock. Space Sci Rev 36:64–109. doi:10.1007/BF00213958